TSUNAMI LOADS ON STRAIGHT AND SKEWED BRIDGES – PART 2: NUMERICAL INVESTIGATION AND DESIGN RECOMMENDATIONS

Final Report

PROJECT TPF 5-307

RESEARCH

TSUNAMI LOADS ON STRAIGHT AND SKEWED BRIDGES – PART 2: NUMERICAL INVESTIGATION AND DESIGN RECOMMENDATIONS

Final Report

PROJECT TPF 5-307

By

Denis Istrati, Assistant Research Professor, Ph.D.
Ian G Buckle, Foundation Professor, Ph.D.

Department of Civil and Environmental Engineering
University of Nevada, Reno

for

March 2021

Technical Report Documentation Page

1. Report No. FHWA-OR-RD-21-13	2. Government Accession No.	3. Recipient's Catalog No.
4. Title and Subtitle Tsunami Loads on Straight and Skewed Bridges – Part 2: Numerical Investigation and Design Recommendations		5. Report Date March 2021
		6. Performing Organization Code
7. Author(s) Denis Istrati, https://orcid.org/0000-0002-1210-0338 Ian G Buckle, https://orcid.org/0000-0002-7858-7054		8. Performing Organization Report No.
9. Performing Organization Name and Address Department of Civil and Environmental Engineering University of Nevada, MS 0258 Reno, Nevada 89557		10. Work Unit No. (TRAIS)
		11. Contract or Grant No.
12. Sponsoring Agency Name and Address Oregon Dept. of Transportation Research Section Federal Highway Admin. 555 13th Street NE, Suite 1 1200 New Jersey Avenue SE Salem, OR 97301 Washington, DC 20590		13. Type of Report and Period Covered Final Report
		14. Sponsoring Agency Code

15. Supplementary Notes

Abstract: Despite the documented vulnerability of coastal bridges in recent tsunami events, no formal guidance exists to date for the tsunami design of such structures. To contribute to the development of such guidelines, this report presents the results of a numerical investigation into tsunami-induced loads on bridges. Following extensive validation of an incompressible hydrodynamic solver, three existing bridges owned by the Oregon Department of Transportation, are investigated, including open-girder and box-girder superstructures. These analyses revealed that when a bore impacts a straight bridge, large impulsive horizontal (F_x) and uplift (F_y) loads together with an overturning moment about the longitudinal axis of the bridge (M_z) are simultaneously applied to the bridge, increasing the likelihood for severe damage. As the angle of skew increases the magnitude of the impulsive component of these loads decreases, leading to a decreasing trend in F_x, F_y and M_z. On the other hand these structures are also subject to (i) a force normal to the direction of wave propagation, and (ii) moments about the y- and z-axes. The F_z force and the yaw moment M_y can have a detrimental effect on bridge performance because they generate out-of-plane horizontal loads that can result in unseating of the deck, while the roll moment M_x can overload the structural components (bearings and shear keys) at one end of a skewed deck. Another important finding is that while a tsunami wave that strikes a straight bridge at an oblique angle generates significant three-dimensional effects similar to skewed bridges, such a wave can lead to more severe deck loads due to the interaction of the wave with the bridge abutments and a subsequent channeling effect. Finally, to assist bridge designers, the report presents a simplified methodology for the tsunami design of skewed bridges, and performance criteria for bridges in tsunami-prone areas, based on (i) two tsunami levels, (ii) three bridge operation categories, and (iii) three performance levels to quantify the criteria.

17. Key Words: Tsunami, Loads, Bridges, Numerical, CFD, Waves Skew, Oblique incidence, Design recommendations	18. Distribution Statement Copies available from NTIS, and online at www.oregon.gov/ODOT/TD/TP_RES/

19. Security Classification (of this report) Unclassified	20. Security Classification (of this page) Unclassified	21. No. of Pages 104	22. Price

SI* (MODERN METRIC) CONVERSION FACTORS

APPROXIMATE CONVERSIONS TO SI UNITS					APPROXIMATE CONVERSIONS FROM SI UNITS				
Symbol	When You Know	Multiply By	To Find	Symbol	Symbol	When You Know	Multiply By	To Find	Symbol
LENGTH					**LENGTH**				
in	inches	25.4	millimeters	mm	mm	millimeters	0.039	inches	in
ft	feet	0.305	meters	m	m	meters	3.28	feet	ft
yd	yards	0.914	meters	m	m	meters	1.09	yards	yd
mi	miles	1.61	kilometers	km	km	kilometers	0.621	miles	mi
AREA					**AREA**				
in^2	square inches	645.2	millimeters squared	mm^2	mm^2	millimeters squared	0.0016	square inches	in^2
ft^2	square feet	0.093	meters squared	m^2	m^2	meters squared	10.764	square feet	ft^2
yd^2	square yards	0.836	meters squared	m^2	m^2	meters squared	1.196	square yards	yd^2
ac	acres	0.405	hectares	ha	ha	hectares	2.47	acres	ac
mi^2	square miles	2.59	kilometers squared	km^2	km^2	kilometers squared	0.386	square miles	mi^2
VOLUME					**VOLUME**				
fl oz	fluid ounces	29.57	milliliters	ml	ml	milliliters	0.034	fluid ounces	fl oz
gal	gallons	3.785	liters	L	L	liters	0.264	gallons	gal
ft^3	cubic feet	0.028	meters cubed	m^3	m^3	meters cubed	35.315	cubic feet	ft^3
yd^3	cubic yards	0.765	meters cubed	m^3	m^3	meters cubed	1.308	cubic yards	yd^3
~NOTE: Volumes greater than 1000 L shall be shown in m^3.									
MASS					**MASS**				
oz	ounces	28.35	grams	g	g	grams	0.035	ounces	oz
lb	pounds	0.454	kilograms	kg	kg	kilograms	2.205	pounds	lb
T	short tons (2000 lb)	0.907	megagrams	Mg	Mg	megagrams	1.102	short tons (2000 lb)	T
TEMPERATURE (exact)					**TEMPERATURE (exact)**				
°F	Fahrenheit	(F-32)/1.8	Celsius	°C	°C	Celsius	1.8C+32	Fahrenheit	°F

*SI is the symbol for the International System of Measurement

iii

ACKNOWLEDGEMENTS

DISCLAIMER

TABLE OF CONTENTS

LIST OF TABLES

LIST OF FIGURES

1.0 COMPUTATIONAL FLUID DYNAMIC ANALYSES

1.1 INTRODUCTION

Tsunamis are one of the most devastating natural disasters with the potential to cause significant casualties and damage to infrastructure. In the last two decades several major tsunami events have occurred in different locations around the world, such as, the Indian Ocean (2004), Chile (2010), Japan (2011) and Sulawesi (2018), which were generated by underwater earthquakes, landslides or volcanic eruption. These events caused severe damage to ports, buildings and infrastructure. Bridges were washed away, cutting lifelines and hindering the efforts of rescue teams to provide help to the people in need. In view of the widespread damage to coastal bridges and the lack of tsunami design guidelines, a Pooled-Fund Study (TPF-5(307)) with contributions from Oregon DOT, Caltrans, Washington DOT, Alaska DOT and Hawaii DOT, was formed with the objective to develop "Guide Specifications for Tsunami Design of Highway Bridges". The research part of the study is led by the Pacific Earthquake Engineering Research Center (PEER), and the University of Southern California.

This report contributes to the TPF-5(307) by advancing the fundamental knowledge of tsunami-induced effects on coastal bridges and developing a simplified design methodology, as described below. In fact, the present report complements the experimental investigation and simplified methods developed in (Istrati and Buckle, 2020), and focuses on the numerical investigation of the tsunami-induced loading on bridges. Funding for this effort was provided principally by the Oregon DOT. The content of this report is as follows:

- Given the complex physics involved in the interaction of tsunami waves with coastal bridges, and the significant uncertainty associated with computational fluid dynamic analyses, Chapter 1 focuses on the extensive validation of a Finite Element Method (FEM)-based hydrodynamic solver using small-scale simplified experiments and more realistic large-scale experiments of wave impact on bridges. Validation of this code is necessary to give confidence in the simulations described in subsequent chapters.

- Chapter 2 investigates the tsunami-induced loads on three existing bridges located in Oregon, including straight bridges with two different superstructure types (open-girder and box-girder), as well as, a skewed bridge. Moreover, this chapter presents an insight into the limitations of 2D analyses relative to 3D ones utilizing the numerical results of the three real bridges.

- Chapters 3 and 4, focus on the investigation of the applied loads on skewed bridges and straight bridges subjected to an oblique tsunami attack via sophisticated three-dimensional analytical simulations. These chapters shed light on the complex three-dimensional effects generated in the two aforementioned tsunami scenarios, and develop a simplified methodology for the tsunami design of skewed bridges.

- In Chapter 5 the authors develop performance criteria for bridges in tsunami-prone areas, based on (i) two tsunami levels, (ii) three bridge operation categories, and (iii) three performance levels to help quantify the criteria.

- The last chapter summarizes the findings of the analytical study and discusses remaining knowledge gaps that need to be addressed by future studies.

1.2 NUMERICAL METHODOLOGY

In this study the finite element based code LS-DYNA ICFD (LSTC, 2014) was used in all the analytical investigations. This code can simulate the incompressible flow of single and multi-phase fluids, and their impact on rigid and flexible structures. The code solves the Navier-Stokes (NS) equations and the continuity equation, which for incompressible fluids can be represented by the following set of equations:

$$\rho \left(\frac{\partial u_i}{\partial t} + u_j \frac{\partial u_i}{\partial x_j} \right) = -\frac{\partial p}{\partial x_i} + \mu \frac{\partial^2 u_i}{\partial x_j \partial x_j} + \rho f_i \quad \text{in} \quad \Omega$$

$$\frac{\partial u_i}{\partial x_i} = 0 \quad \text{in} \quad \Omega$$

(1-1)

Where:

u_i=velocity in i-direction, p=pressure in i-direction, ρ=density of fluid and μ=fluid dynamic viscosity, Ω=computational domain

In order to solve the above set of differential equations, boundary conditions and initial conditions have to be specified. In the current study, prescribed velocities were used at the inflow boundary, hydrostatic pressures at the outflow, non-slip conditions at the bottom of the computational domain and around the bridge deck, and atmospheric pressure at the top side of the flume. For the time integration of the above equations, the code uses the fractional step method, a projection method in which the pressure and velocity are uncoupled. This means that three linear systems of equations are generated for the momentum equation and one for the incompressibility constraint. The fractional step method at each time-step consists of three sub-steps, with the first step predicting a value for the velocity, the second step projecting the velocity into a divergence free vector field, and the third step moving the fluid particles to their new time step position. These steps are applied iteratively until convergence is reached and the particles move to the same final location. For more information about the fractional step method the reader is referred to the theory manual of the solver (LSTC, 2014).

In free-surface and multi-phase problems the moving interface is simulated via a level-set method based on (Osher and Fedkiw, 2003). In this method an implicit function φ is defined for the whole domain, with φ being positive inside the fluid, negative outside the fluid and zero at the interface. In the case of two-phase fluids, the formulation is similar, however the NS equations are solved in the two domains with a smoothing of the density and viscosity at the

interface. In order to calculate the evolution of the interface, the simple convection equation is used:

$$\frac{\partial \phi}{\partial t} + \vec{V}.\vec{\nabla}\phi = 0,$$

(1-2)

The ICFD solver has different turbulence formulations, including the Reynolds-averaged Navier-Stokes (RANS). The RANS model is the most classic turbulence model and uses a time-averaged version of the governing equations. In this approach the flow is decomposed into a mean and fluctuating component using the Reynolds decomposition method, which leads to a modified set of NS equations for the mean quantities (velocities and pressures). These equations are similar to the ones shown in equation (1-1) but have a new viscous term, which represents the Reynolds stresses generated by the fluctuating velocity field. To solve for the additional unknowns various turbulence models can be used, such as, the standard k-ε, k-omega and Spalart Allmaras approach. These models provide different levels of closure by introducing additional variables, with the most widely used model (k-ε) being dependent on the turbulent kinetic energy k and the turbulent dissipation ε.

Although, such models can be quite accurate for steady-state flows, their accuracy can be significantly reduced when transient effects are significant. For such cases, the solver includes a Large Eddy Simulation (LES) turbulence model. In this model each flow variable is divided into a large-scale component and a sub-grid component. It then makes the assumption that that the large eddies contain most of the kinetic energy of the flow and therefore they are resolved in time (time-dependent variables), while the sub-grid component is estimated via simplified models (Smagorinsky model). The LES model is generally more accurate for transient phenomena than RANS, but computationally expensive and usually more sensitive to the mesh size.

1.3   VALIDATION WITH SMALL-SCALE EXPERIMENTS

1.3.1 Dam-break bore impact on structure

One popular experiment available in the literature, which has been widely used for the validation of the transient fluid impact on structures is the dam-break experiment (Kleefsman et al., 2005) at the Maritime Research Institute Netherlands (MARIN). The popularity of these experiments emanates from the fact that (a) it is a very simple experiment with no special boundary conditions, and (b) the availability of the digital data together with the recorded videos as test case-2 of the SPH European Research Interest Community (Issa and Violeau, 2006). According to Figure 1-1, which shows a schematic of the experiments, the tank has dimensions equal to 3.22×1×1m and an initially closed door with a 0.55m water level. The initial standing water flows into the tank when the door opens and impacts a rectangular structure.

This experiment was modeled with the ICFD solver using three different mesh-sizes, in all of which, the surface mesh of the walls of the computational domain was 1.5cm, while the mesh of the structure was between 0.5cm and 0.8cm. The differences in the two models was the size of

3

the volume mesh generated between the surface mesh of the structure and the computational domain. In the first model this mesh-size inside the domain was up to 2.2cm, while in models 2 and 3 the maximum mesh-size inside the domain was 1.6cm. The last model (model 3) had overall the largest number of elements because it had a localized small mesh (equal to 0.8cm) in a selected volume around the structure, which extended in the vertical direction for a distance of 40cm from the bottom of the flume and 60cm in the horizontal direction. The total number of tetrahedral elements in model 1, 2, and 3 were about 2million, 5million and 6.2million respectively.

Figure 1.2 shows a qualitative comparison of the experiments and the numerical simulations, by illustrating selected snapshots of the fluid flow slightly before and after the impact on the structure (at t=0.4sec and t=0.56sec). It can be observed that the hydrodynamic solver provides reasonable predictions of the hydrodynamic flow. Moreover, Figure 1.3 shows a comparison of the recorded pressures at three different locations of the front face of the structure. Interestingly, although all three models with the different mesh-sizes give very good agreement with the experimentally recorded pressures at locations P2 and P3, this is not the case with P1, which is the point closest to the ground and the one that comes first in contact with the dam-break bore. For this location, while models 2 and 3 give very good estimates, the model with the coarser mesh can over-predict the magnitude by a factor of 2. Overall this example demonstrates the sensitivity of the numerical results to the mesh and the importance of the proper selection of the size for capturing localized pressures applied by bores.
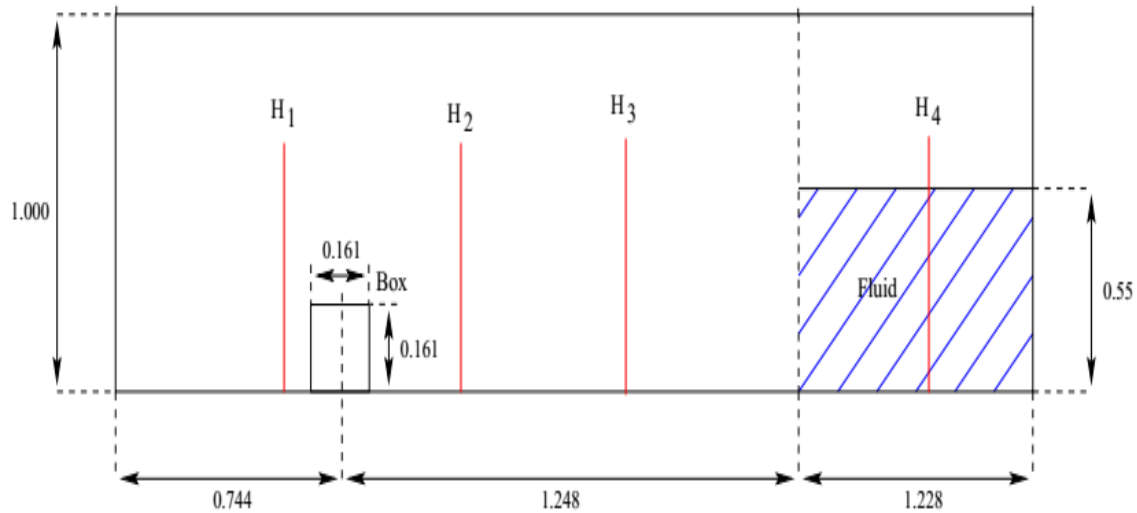
Figure 1.1: Side view of the dam-break experiments conducted by Kleefsman et al (2005) (adopted from Issa and Violeau (2006))
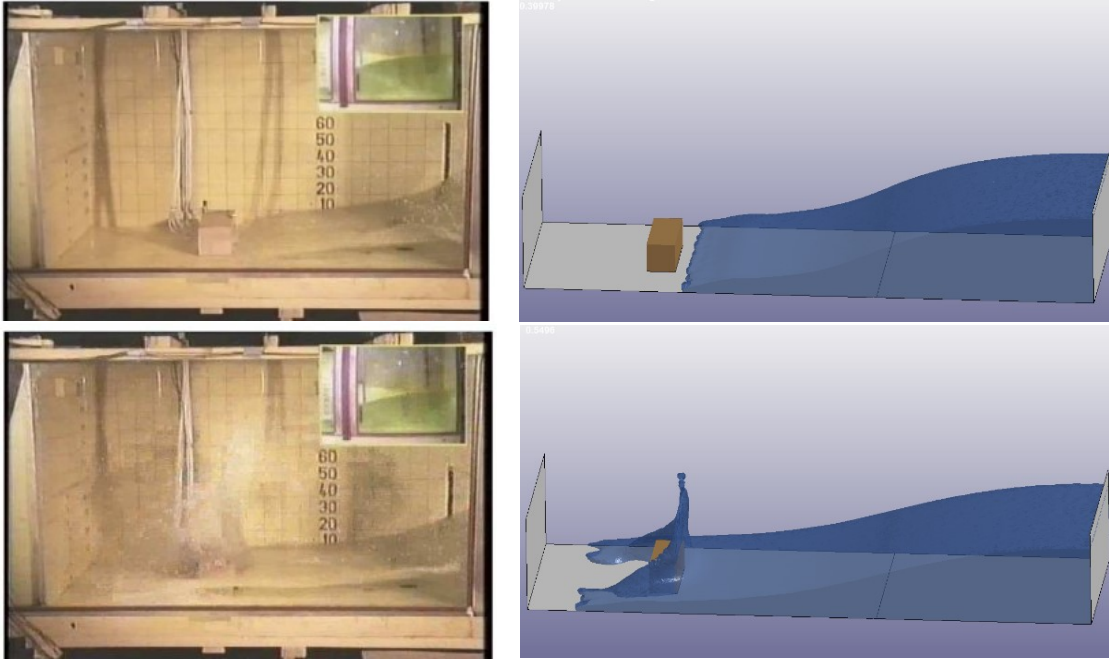
Figure 1.2: Snapshots of dam-break impact on a structure from experiments (left: adopted from Issa and Violeau (2006)) and CFD analyses conducted herein (right)
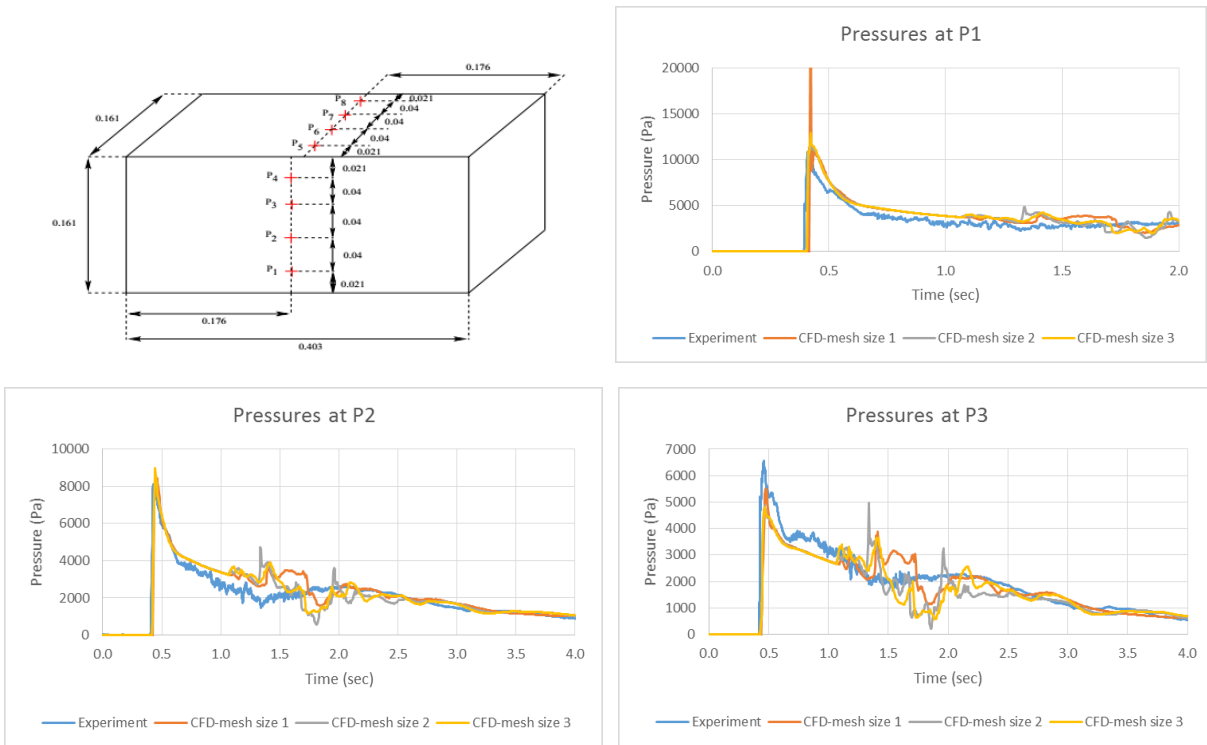
Figure 1.3: Pressure gage location (top-left: adopted from Issa and Violeau (2006)) and recorded pressures in Kleefsman's experiments and by the ICFD solver

1.3.2 Solitary wave impact on slab-type bridge

Another interesting experimental study available in the literature is presented in (Seiffert et al., 2014). These experiments focused on elevated decks (slab-type) and can be conveniently used for the calibration and validation of numerical codes because the authors used simplified and easily reproducible solitary waves, which propagated over a horizontal slab (see Fig. 1.4). Moreover, the authors provide in the aforementioned paper the time-histories of the free-surface together with the corresponding recorded forces for a specific wave height, enabling the comparison of numerical solutions of both of these parameters. Given the fact that the authors removed the higher frequency peaks of the forces (which were caused by structural dynamic effects), their results could directly be used for the validation of CFD analyses (which treat the structure as a boundary with no dynamic properties).

These experiments were conducted in a wave flume with a piston-type wavemaker and dimensions equal to 9.14m x 0.152m x 0.39m. The structure had a length of 0.149m, width 0.305m, and thickness 1.27cm and was located a distance of 2.62m from the wavemaker. The free-surface was recorded at three locations, with WG1 being located on the offshore side of the slab at 0.610m horizontal distance. This experimental setup was modeled numerically as a two-dimensional problem using LS-DYNA's ICFD solver. Prescribed velocities were applied at the inlet, hydrostatic pressures at the outlet, free-slip conditions at the bottom of the flume and nonslip conditions on the structure. The mesh-size was 5mm in the horizontal direction and 2mm in the vertical one, while the time-step of the analyses was determined using a value of about 0.5 for the Courant-Friedrichs-Lewy (CFL) condition. Both RANS and LES turbulence models were utilized with the best agreement being achieved by LES. Figure 1.5 shows a comparison of the free-surface recorded by WG1 together with the horizontal and vertical forces. It becomes apparent from the graph that the hydrodynamic solver predicts both the free-surface and the wave-induced structural forces very well.
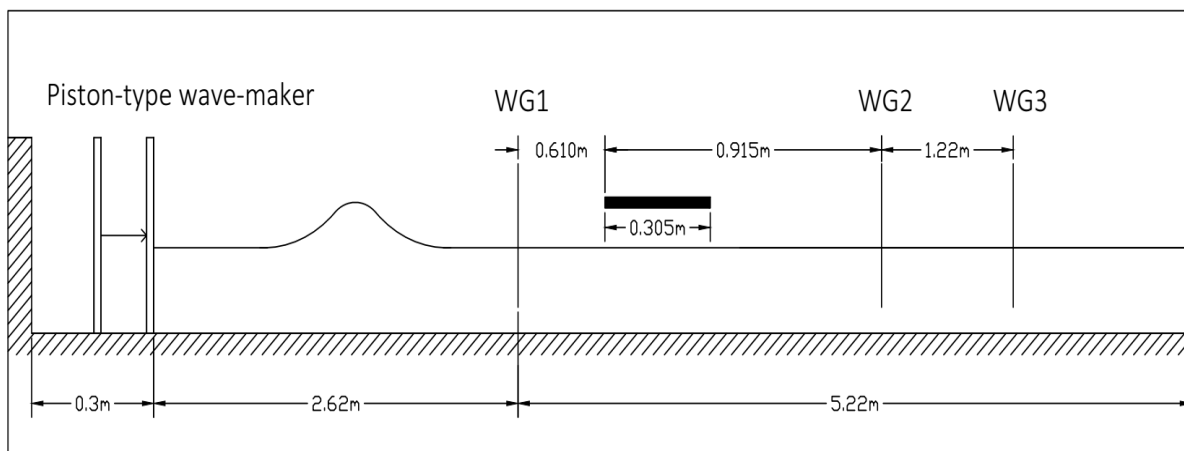
Figure 1.4: Schematic of wave impact experiments on a slab (source: Seiffert et al., 2014)
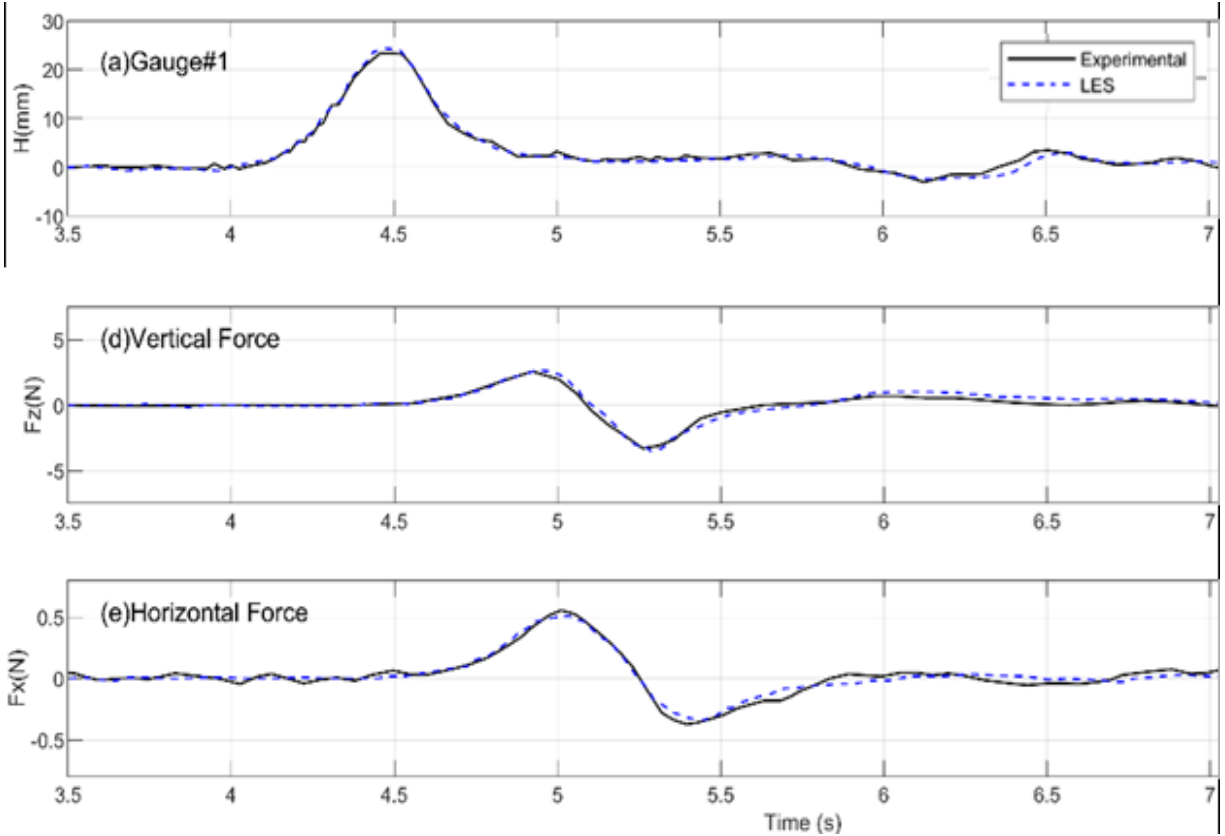
Figure 1.5: Comparison of free-surface histories recorded in the experiments of Seiffert et al (2014) and predicted by the ICFD solver (courtesy: Hasanpour and Istrati)

1.4   VALIDATION WITH LARGE-SCALE EXPERIMENTS

1.4.1 Straight box-girder bridge

Given the good performance of the hydrodynamic solver in predicting the bore and solitary wave-induced pressures and forces on small-scale structures (see section 1.3), it was of interest to investigate the capabilities and limitations of the code in more realistic large-scale experiments. For this purpose, the 1:5 scale experiments of tsunami impact on a box-girder bridge conducted by the authors in a prior project (Istrati D., 2017; Istrati and Buckle, 2020), were used as a benchmark. These experiments were conducted in the Large Wave Flume at OSU, which is 104.24 m long, 3.66 m wide, and 4.57 m deep, with the testing section having a length of 87.43m. Figure 1.6 shows an overview of the bridge specimen, the testing setup and the wave flume (note that although the bottom graph of Fig. 1.6 shows an open-girder superstructure, the same setup was utilized for the box-girder as well.). The experimental setup consists of a superstructure with in-plane dimensions 3.45m length and 1.94m width, supported on elastomeric bearings, bent caps, and black beams that transfer the loads to the walls of the flume. The bridge has also shear keys that restrict the lateral movement (in the direction of the wave propagation) but allow the bridge to move vertically and rotate, meaning that the dynamic bridge response and wave-structure interaction might play a major role on the actual structural

demand. Modal analyses and hammer tests determined that the fundamental frequency of the bridge structure was 32-34Hz.

Uniaxial load cells were installed below the bearings and at the level of the bent cap in the horizontal and vertical direction. This means that the measurements of the horizontal force will be generated by the applied pressures on the superstructure, the bent cap and all the connecting elements in between them (bearings, shear keys, steel plates). As shown in Figure 1.7, an important characteristic of these experiments is that due to the change of the bathymetry at a distance of about 21.49m from the wavemaker, the solitary waves are starting to undergo transformations with noticeable increases in the maximum wave height and changes in the wave shape by the time it reaches the bridge.

With the above complex characteristics of the test setup in mind and the need to develop numerical models that could achieve reasonable accuracy at the minimum possible computational cost, it was decided to simulate only part of the flume, as was done in other studies (Yang et al., 2014). In fact, instead of simulating a length of 87.43m, the numerical model simulated only the area between wg9 and wg13 with a length of 26m (shown with an enclosed rectangular box in the center graph of Figure 1.6). At the inlet of the truncated domain the modified transient wave was simulated as a solitary wave with an adjusted height in order to account for the height increase during the wave propagation. Several mesh-sizes were investigated with the size of the elements on the surfaces of the computational domain ranging between 10cm (coarse mesh) to 2.5cm (fine mesh), and the mesh on the bridge ranging between 5cm and 0.65cm. The initial (coarse) bridge mesh was selected so that we can have 12 elements along the height of the deck and 40 elements across its width, and then this size was reduced to half and a quarter of the initial one in order to investigate the sensitivity of the numerical results to the discretization. The model with the fine mesh had a total of about 550k triangular elements, requiring the use of a high-processing computing system. Nonslip conditions were applied on the bridge surface and bottom of the flume, prescribed velocities at the inlet, and prescribed hydrostatic pressures at the outlet and the top of the computational domain, while the turbulent flow was simulated via the Large Eddy Simulation (LES) mathematical model.

Figures 1.8 and 1.9 show a comparison of the free-surface and force histories between the experiments and numerical calculations for a wave with H=0.42m and demonstrate that:

- Truncated domains with equivalent simplified prescribed waves at the inlet can capture the magnitude and shape of the wave that impacts the structure quite reasonably. In fact, unbroken (symmetric) solitary waves were able to match surprisingly well the magnitude (within 10%) and the shape of the leading part of the transient/transformed waves of the experiments (at wg10 and wg11 which were close to the bridge), however, they could not capture the trailing part of the wave (e.g. between 4.5-7sec of the free-surface histories at wg11 shown in Fig. 1.8).

- More importantly, despite the fact that the solitary waves of the truncated domain did not represent exactly the waves of the experiments (as explained above), the hydrodynamic solver predicts quite accurately the magnitude of both the maximum horizontal and uplift force (within 10% of the experimental values). While the numerical force histories seem to exhibit similar trends with the experimental ones,

they do not capture accurately the force fluctuations after the occurrence of the maximum values (after the wave has slammed the offshore face and has started inundating the deck). Possible reasons for the differences are:

a) the inability of the solitary waves in the CFD solver to capture the shape of the trailing part of the transient waves of the experiments, meaning that a smaller volume of water impacted the bridge in the numerical simulations, leading to modifications in the inundation process and the force-histories,

b) the potentially important role of structural dynamics and wave-structure interaction in the experiments, which were not simulated in the CFD analyses,

c) the fact that in the experiments part of the vertical load was transferred to the bent caps via the friction generated between the steel girders and shear-keys, and therefore was not measured by the load cells below the girders. This in turn means that the experimental measurements of the vertical forces below the deck might differ from the total induced vertical load, which is the one predicted by the CFD solver. And

d) the fact that the numerical model did not simulate all the other structural components (bearing, shear keys, connecting plates, bent caps and support beams) that might have affected the hydrodynamic flow around the structure and the associated fluid pressures.

Overall this benchmark case demonstrates that the use of two-dimensional models with truncated numerical domains can not only reduce the computational time significantly (e.g. by 80% or more) but also give reasonable estimates of the forces applied on a box-girder bridge impacted by a tsunami wave at a normal angle.
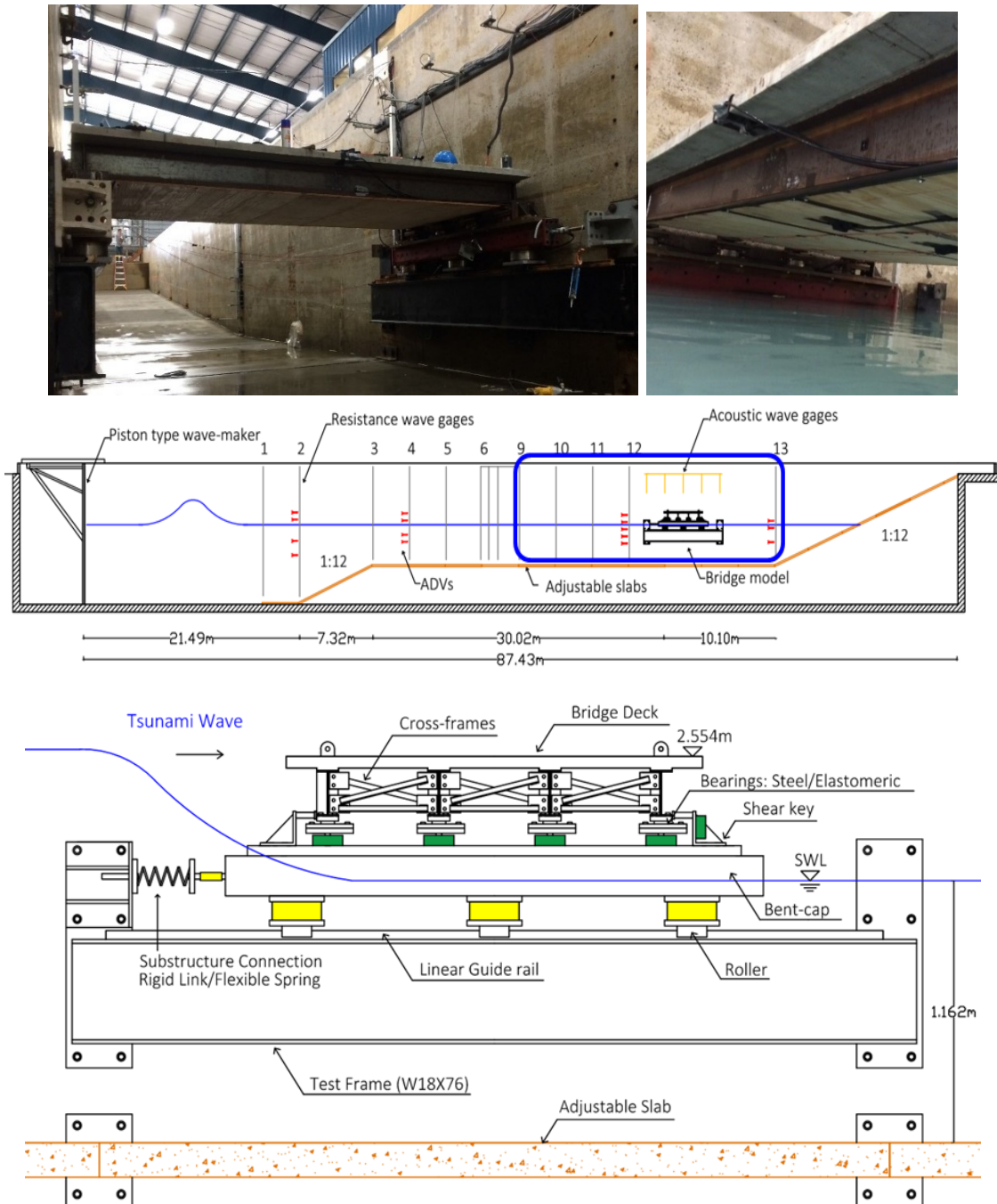
Figure 1.6: Overview of the box-girder bridge specimen (top), the wave flume with the instrumentation (center), and the experimental setup at the bridge location (bottom), which was used as benchmark problem for the validation study
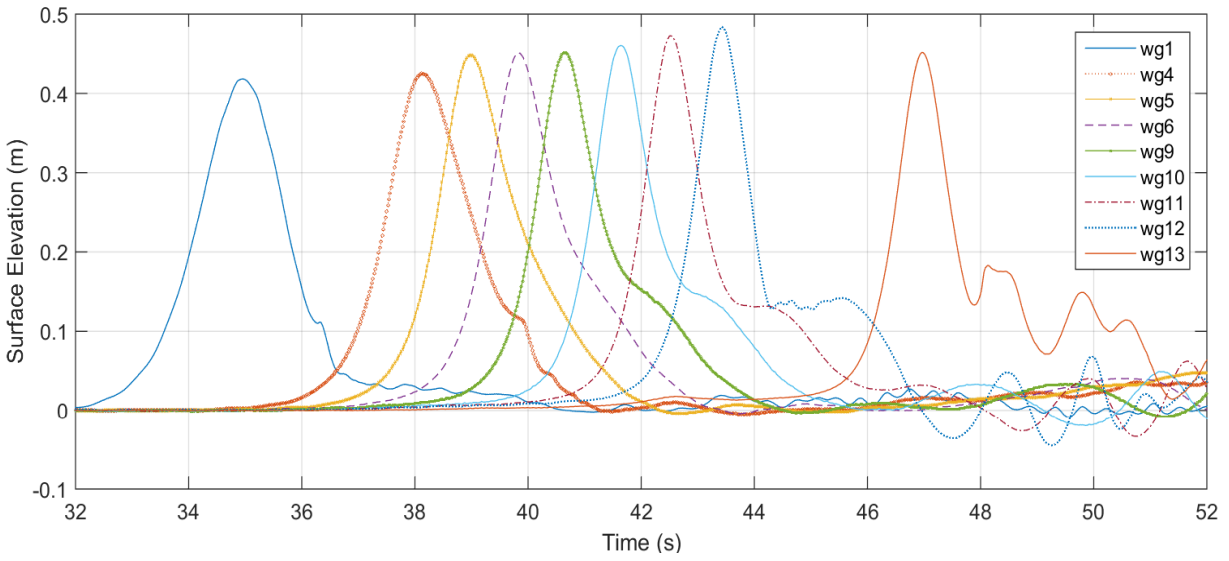
Figure 1.7: Experimentally recorded free-surface histories along the flume for H=0.42m
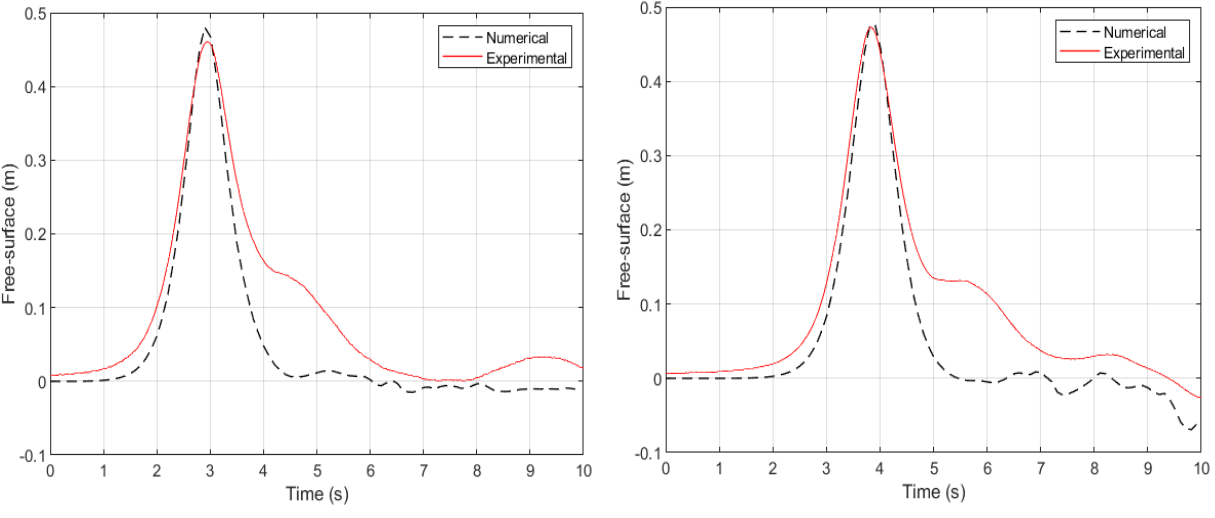
Figure 1.8: Free-surface histories at wg10 and wg11 for the wave with H=0.42m

11
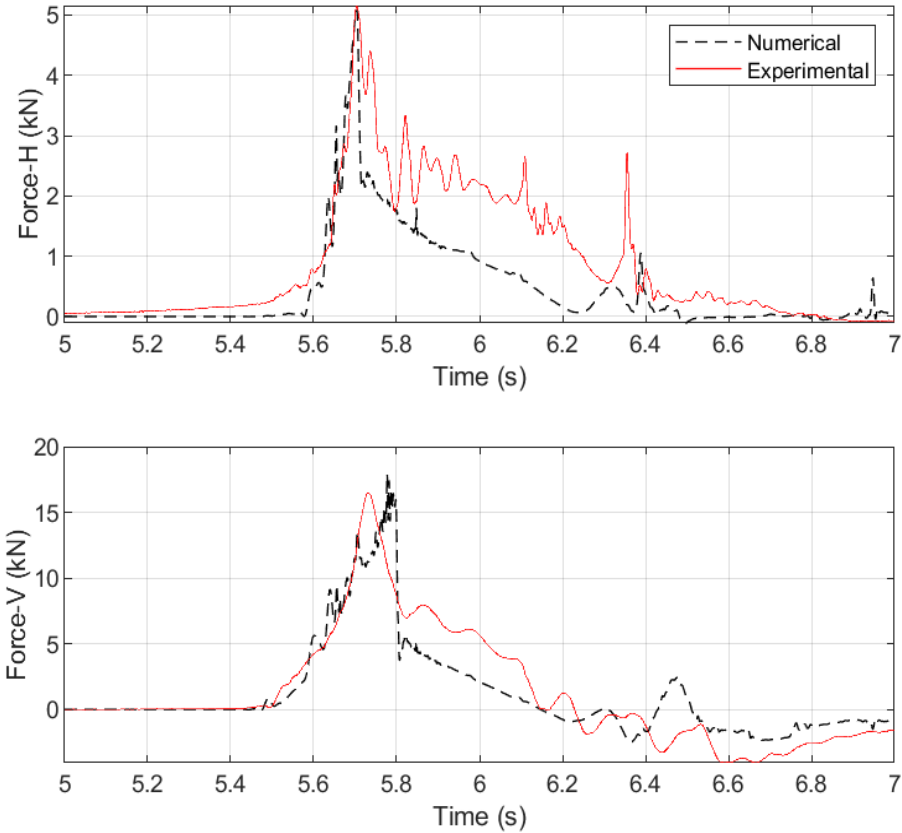
Figure 1.9: Force histories for the box-girder impacted by a wave with H=0.42m

1.4.2 Skewed open-girder bridge

Perhaps one of the most challenging benchmark problems presented herein was the simulation of solitary wave impact on a skewed bridge specimen. The benchmark structure had a 46.6º skew angle and three I-girders with cross-frames. It was tested experimentally in the same flume as the straight box-girder bridge described in the previous section. As shown in Fig. 1.10, the skewed bridge also had the same/similar structural components as the straight box-girder bridge with the main difference being that it was supported on steel bearings. These bearings restrained all the degrees of freedom minimizing consequently the structural deformations and potential fluid-structure interaction effects. More details about the experimental investigation can be found in (Istrati and Buckle, 2020).

Given the efficiency and promising -in terms of accuracy- performance of reduced computational domains seen in the previous section, the same approach was used in this section too. However, the computational domain was three-dimensional with a width of 3.66m, which is 20cm more than the normal (to the direction of the wave propagation) length of the skewed bridges. This means that there is a 10cm gap between the side of the bridge and the flume walls. The two main assumptions/simplifications made in the numerical model are the:

- Reduction of the length of the numerical wave flume from 87.43m to 26m and the representation of the transient waves with symmetric solitary waves (see Fig. 1.8 of previous section)

- Modeling of only the superstructure, without consideration of the bearing, shear keys, connecting plates, cross-frames, welded (plate-type) stiffeners of the girders, bent caps and support beams that might have affected the hydrodynamic flow around the structure and the associated fluid pressures.

In the numerical model nonslip conditions were applied on the bridge surface, freeslip at the bottom of the flume, prescribed velocities at the inlet, and prescribed hydrostatic pressures at the outlet. Three different mesh sizes were investigated, with the size of the elements on the surfaces on the bridge ranging between 1.25cm and 7.4cm. In fact the model with the coarse mesh Mesh 1), had a 2.5cm mesh-size in the vertical direction (y-axis) and the direction of the wave propagation (x-axis), but had about three times larger elements (7.5cm) in the z-direction (normal to the wave propagation). In the model with the finest mesh (Mesh 3), the aspect ratio of the bridge elements were approximately the same, but their size was half of the coarse mesh, ranging between 1.35cm and 3.7cm (as shown in Figure 1.11). The total number of the elements in the three mesh-sizes were 14.7million, 15million and 21.3million. As noticed, although the model with the fine mesh had elements around the bridge at half the size of the coarse mesh, the total number of elements increased only by 45% and this is because the surface mesh of the sides of the computational domain were kept equal to 5cm in all the models. Nonetheless, the model with the fine mesh was computationally more expensive than the model with the coarse mesh because it required twice the time for each analysis.

Figure 1.12 shows a qualitative comparison of the inundation process witnessed in the large-scale experiments and the three-dimensional CFD analyses. Although, the snapshots of the experiments and numerical simulations were not perfectly synchronized, they do show similar patterns, complex shapes of the wave as it impacts the bridge, and similar hydrodynamic flow on top of the deck, increasing the confidence in the hydrodynamic solver. Moreover, Figure 1.14 and 1.15, show the time histories of the applied forces (in x and y) and moments (about x and z) for the numerical models with the coarse and fine mesh respectively, revealing that:

- Both numerical models underpredict the maximum Fx and this underprediction becomes smaller for the fine mesh. The reason behind this behavior is the fact that in the experiments the tsunami wave impacts the bent cap below the offshore acute corner before it reaches the deck. Since the uniaxial loads record the horizontal force at the level of the bent cap, they consider also the fluid pressures applied on the bent cap and all the other components between the bent cap and the girders. This is why the experimentally recorded Fx histories exhibit a small gradual increase at the beginning and a more abrupt increase later on as it touches the girders. On the other hand, the Fx histories of the numerical model, which did not include the applied load on the bent caps, start a few fractions of a second later. Taking the above observations into account it can be concluded that the approximately 0.5kN load seen at the beginning of the experimentally recorded Fx histories is generated by the pressures on the bent cap and other components below the girders. If the numerical results are adjusted to include this 0.5kN load from the bent caps then a match better agreement

of the Fx forces is achieved, with the smallest mesh size giving an accurate prediction of the maximum force. The only difference is at the end of the force histories, which can be justified though by the differences in the trailing part of the simulated solitary waves and the transformed waves of the experiments (see discussion related to Fig. 1.8)

- The hydrodynamic solver can give very good predictions of the vertical forces, as well as, the moments Mx and Mz with surprisingly accurate prediction of the maximum values (within 10% for the coarse mesh and 5% for the fine mesh). There still exist some differences in the time-histories (e.g. in the negative peaks of Mx and Mz), but those can easily be justified by the simplifications of the numerical model of the bridge, which involved only the deck with the girders, and the differences in the shape of the waves, as discussed previously.

Figure 1.10: Skewed bridge specimen used as a benchmark problem for the validation of the three-dimensional formulation of the CFD solver
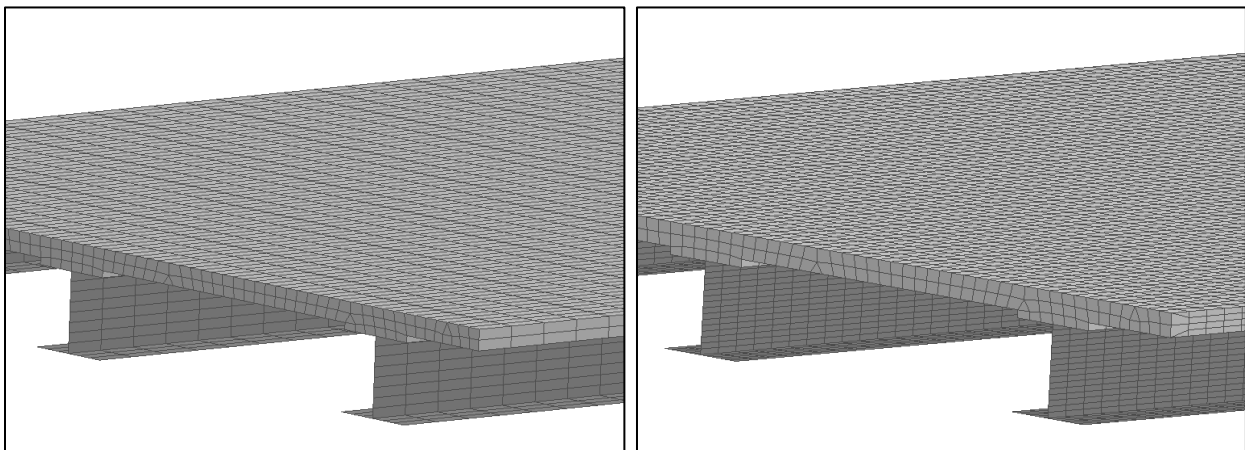
Figure 1.11: Three-dimensional models of the skewed bridge specimen used as a benchmark, with Mesh 1 (left) and Mesh 3 (right)

Figure 1.12: Snapshots of the skewed bridge inundation process recorded in the experiments for H=0.55m
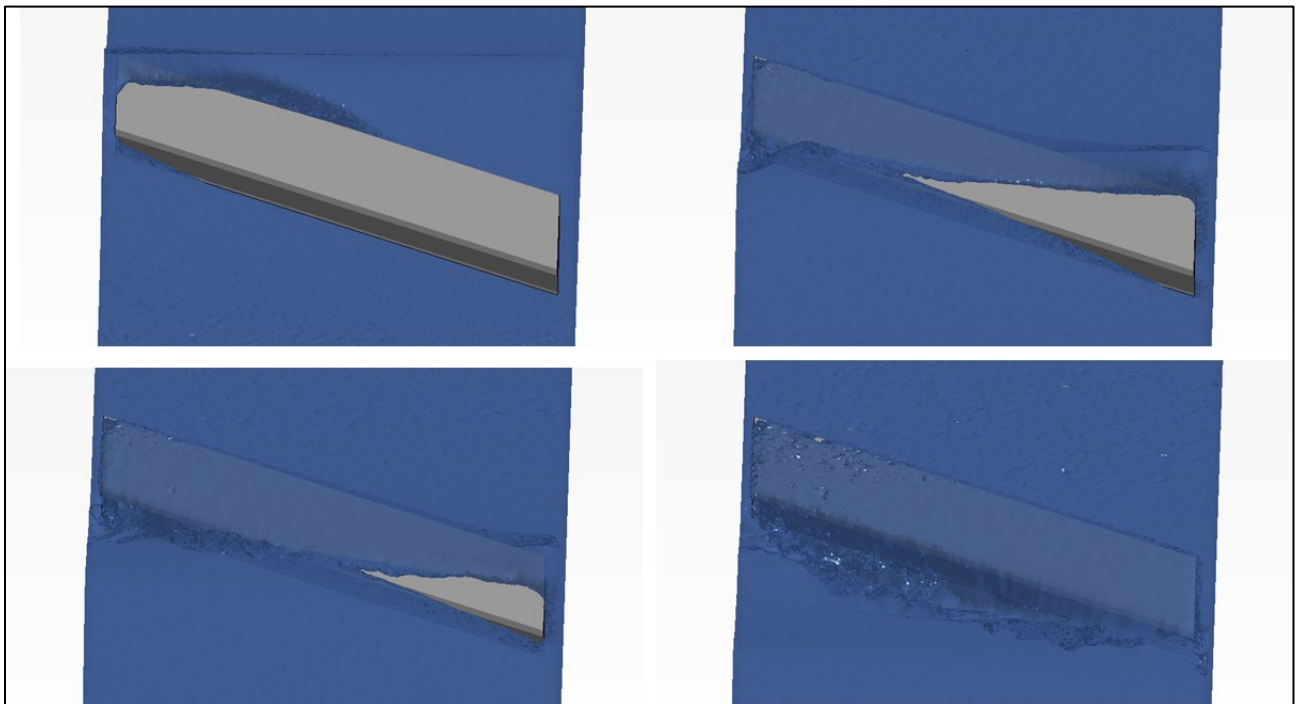
Figure 1.13: Snapshots of the skewed bridge inundation process recorded in the numerical simulations for H=0.55m
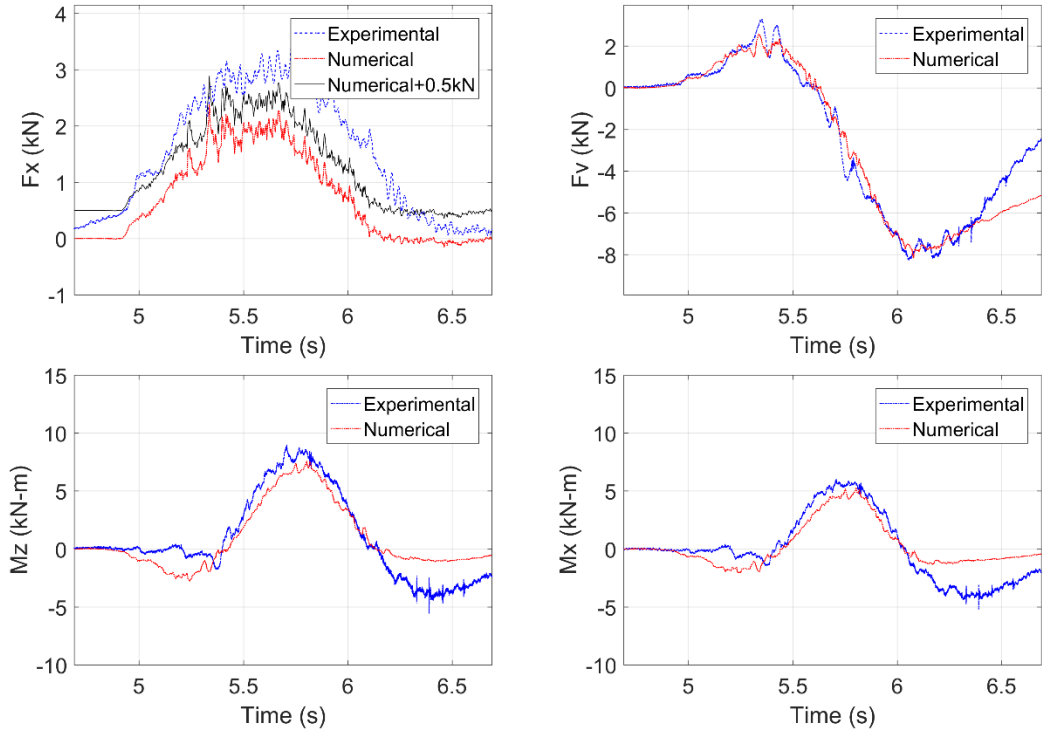
Figure 1.14: Load histories applied on the skewed bridge model with Mesh 1
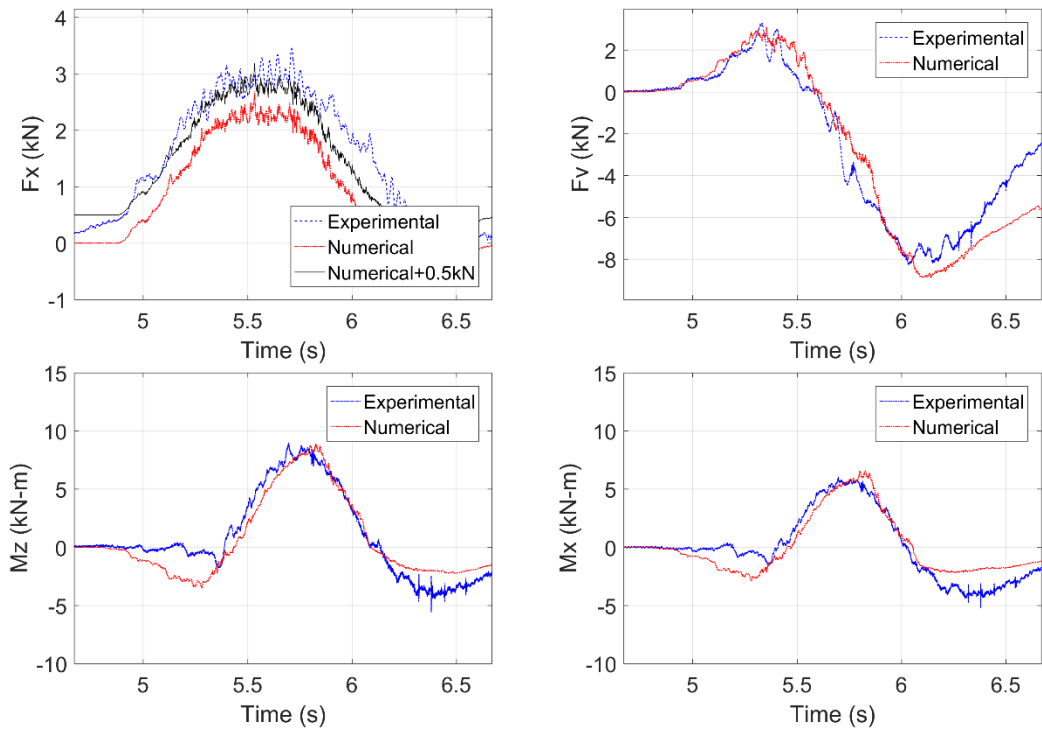
Figure 1.15: Load histories applied on the skewed bridge model with Mesh 3

In summary all the numerical models presented herein demonstrated the ability to achieve surprisingly good accuracy (given the involved uncertainties and simplifications) in predicting both the forces and the moments applied on a skewed specimen. Clearly the smaller mesh improves the accuracy of the numerical results, however this improvement is in the range of 15%, while the increase in the computational expense is 100%. Therefore, it can be concluded from this benchmark that models with medium mesh-sizes (in the range of 2.5cm vertically and up to 7.4cm in the z direction) can give reasonable results for the minimum time, making them an ideal candidate for parametric investigations that require large numbers of analyses.

2.0 NUMERICAL MODELING OF EXISTING BRIDGES IN OREGON

2.1 INTRODUCTION

This chapter presents a numerical investigation of tsunami-induced loads on three existing bridges in Oregon, owned by the Oregon Department of Transportation. The first bridge is the Winchuck River Bridge, the second one is the Schooner Creek Bridge and the third is the Little Nestucca River Bridge. These bridges were selected with the aim of covering typical superstructure types that have been constructed on the U.S. west coast, including open-girder and box-girder bridges, as well as those on straight and skewed alignments. In order to facilitate the reproducibility of the numerical simulations, the authors give the main dimensions and parameters for the numerical models in Table 2.1 and Figure 2.1.

Table 2.1: Description of Model Parameters

Parameter	Description
Hdm	Height of computational domain
Ldm	Length of computational domain
df	Distance of the offshore bridge face from the inlet
Hbc	Elevation of the top-surface of the deck at its mid-width
h	Initial water depth
H	Wave or bore height (measured from the still water level)
v	Particle velocity
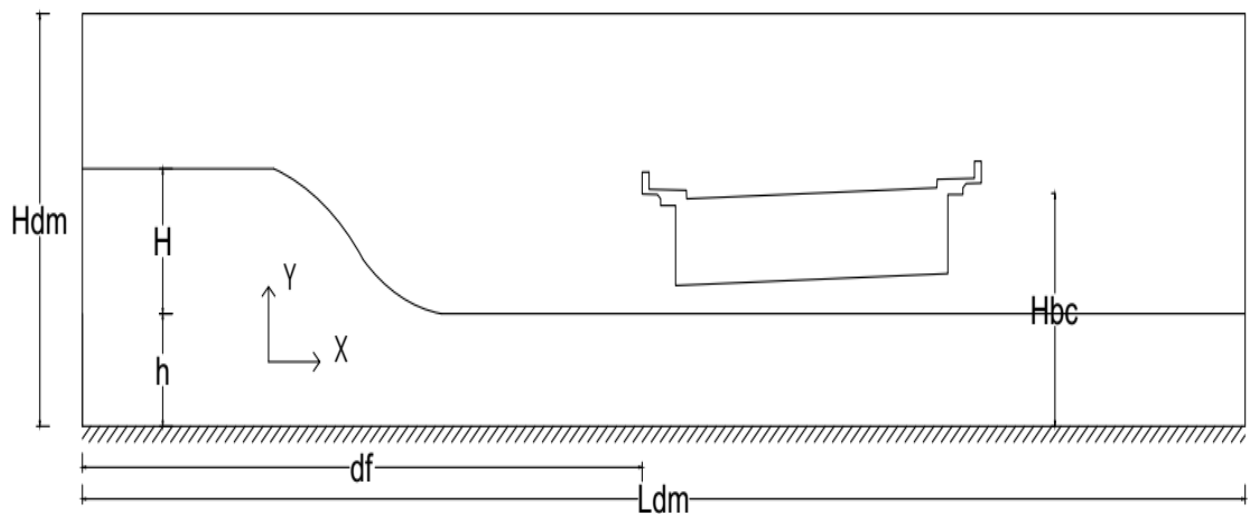
Figure 2.1: Sketch depicting the main parameters describing the numerical models

2.2 WINCHUCK RIVER BRIDGE

2.2.1 Description of structure, models and hydrodynamic conditions

The first bridge to be modelled is the Winchuck River Bridge, shown in Figure 2.2. This is a straight box-girder bridge with three spans and four cells. The elevation of the center span ranges between 19.32ft and 21.43ft and has a super-elevation of about 1.72 degrees. Prior probabilistic tsunami inundation analyses (PTHA), conducted by H. K. Thio using the methodology described by Grezio et.al. (2017), suggested a water depth of 3m and tsunami heights in the range of 2 to 3m at this particular bridge location.

Following the commonly used approach of simulating the wave impact on straight bridges via two-dimensional analyses of a slice of the bridge, the slice at the mid-length of the center span was simulated for this study, as shown in Figure 2.2. The computational domain was 90m long and 11m tall, with the distance of the bridge from the inlet boundary being about 40m. The latter distance was selected in order to properly simulate the smallest solitary wave of interest, which is associated with the largest wavelength. Two different wave types were simulated including unbroken solitary waves and broken waves/bores. The former ones had a height between 1.05m and 2.25m, with H/d ratios between 0.35 and 0.74m, while the two bores had heights of between 2.2m and 2.8m. It is noteworthy that slightly before the impact on the offshore face of the bridge the simulated bores had velocities in the range of 3.5m/s-9m/s, which also varied with the elevation due to the transient nature of the tip of the bore. All these parameters are summarized in Table 2.2.

Table 2.2: Description of the Winchuck River Numerical Models

Parameter	Description
Comp. domain	Ldm=90m, Hdm=11m
Bridge model	df=40m, Hbc=6.21m
Wave/flow	h=3m, H=1.05m÷2.8m, v=2.2m/s÷9 m/s

2.2.2 Sensitivity of numerical analyses

In order to investigate the sensitivity of the numerical method to the mesh, three different bridge models were developed (see Figure 2.2) with mesh-sizes around the bridge being 10cm (Mesh 1), 5cm (Mesh 2) and 2.5cm (Mesh 3). For all these models the size of the surface mesh of the computational domain was kept equal to 10cm, and the total number of nodes was approximately 170k for Mesh 3.The analyses were conducted with a variable time-step that was automatically calculated based on the CFL condition and turbulence effects were represented via the Large Eddy Simulation (LES) mathematical model.

Figures 2.4 and 2.5 show respectively the original and filtered load histories (with a cutout freq. of 100Hz) for the three mesh-sizes and an unbroken solitary wave height with H=1.65m. Note that this results correspond to a 1m wide slice, which means that they shall be multiplied by the length of the span in order to obtain the total loads on the span. Interestingly, all three mesh-sizes show similar trends, with Mesh 2 and 3 demonstrating some differences relative to Mesh 1,

indicating that the latter one might be too coarse. However, the differences in the magnitudes are relatively low. Given the small-observed sensitivity of the results to the mesh-size and the tolerable increase of computational time due to the smaller mesh-size, it was decided to conduct the parametric analysis using the model with Mesh 3.

Figure 2.2: Plan view (top), elevation (center) and cross-section (bottom) of the Winchuck River Bridge (source: Oregon Department of Transportation)
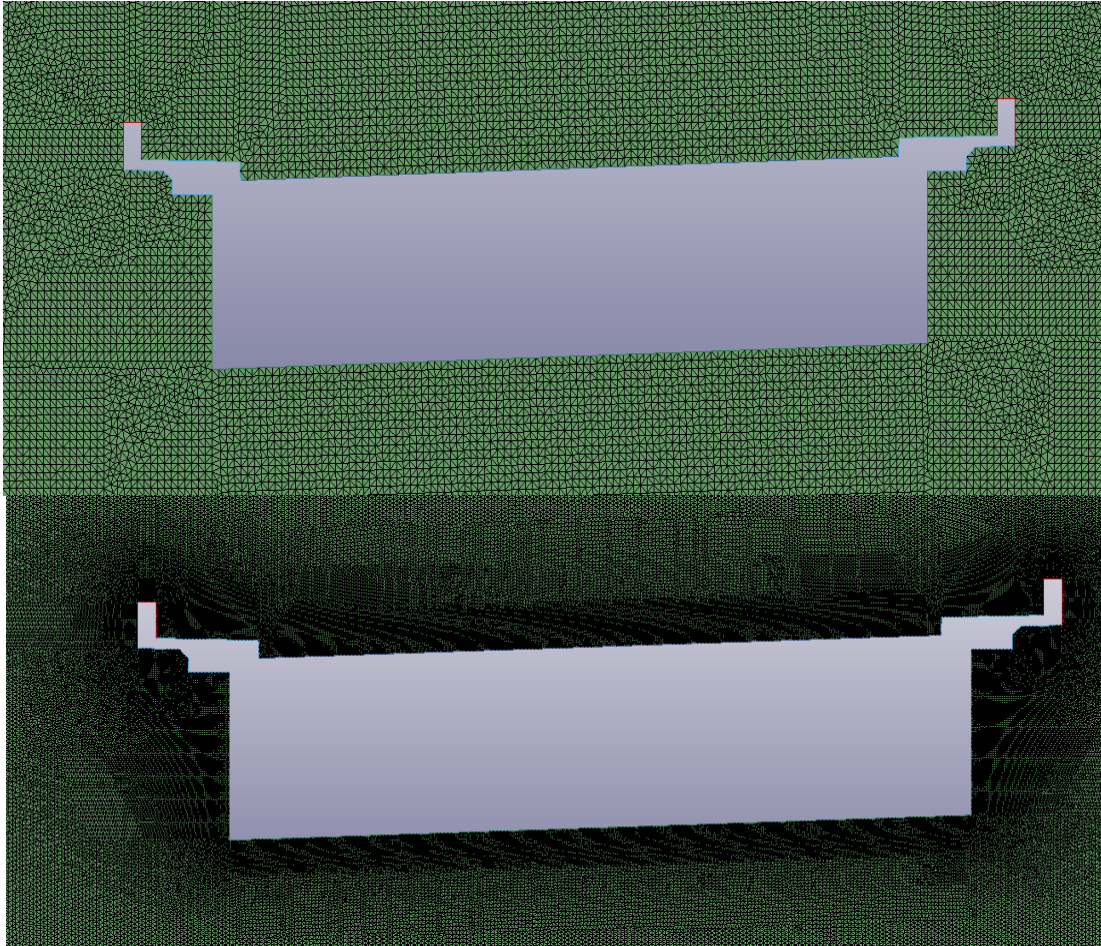
Figure 2.3: Overview of the mesh around the bridge in the numerical models with a coarse and fine mesh size
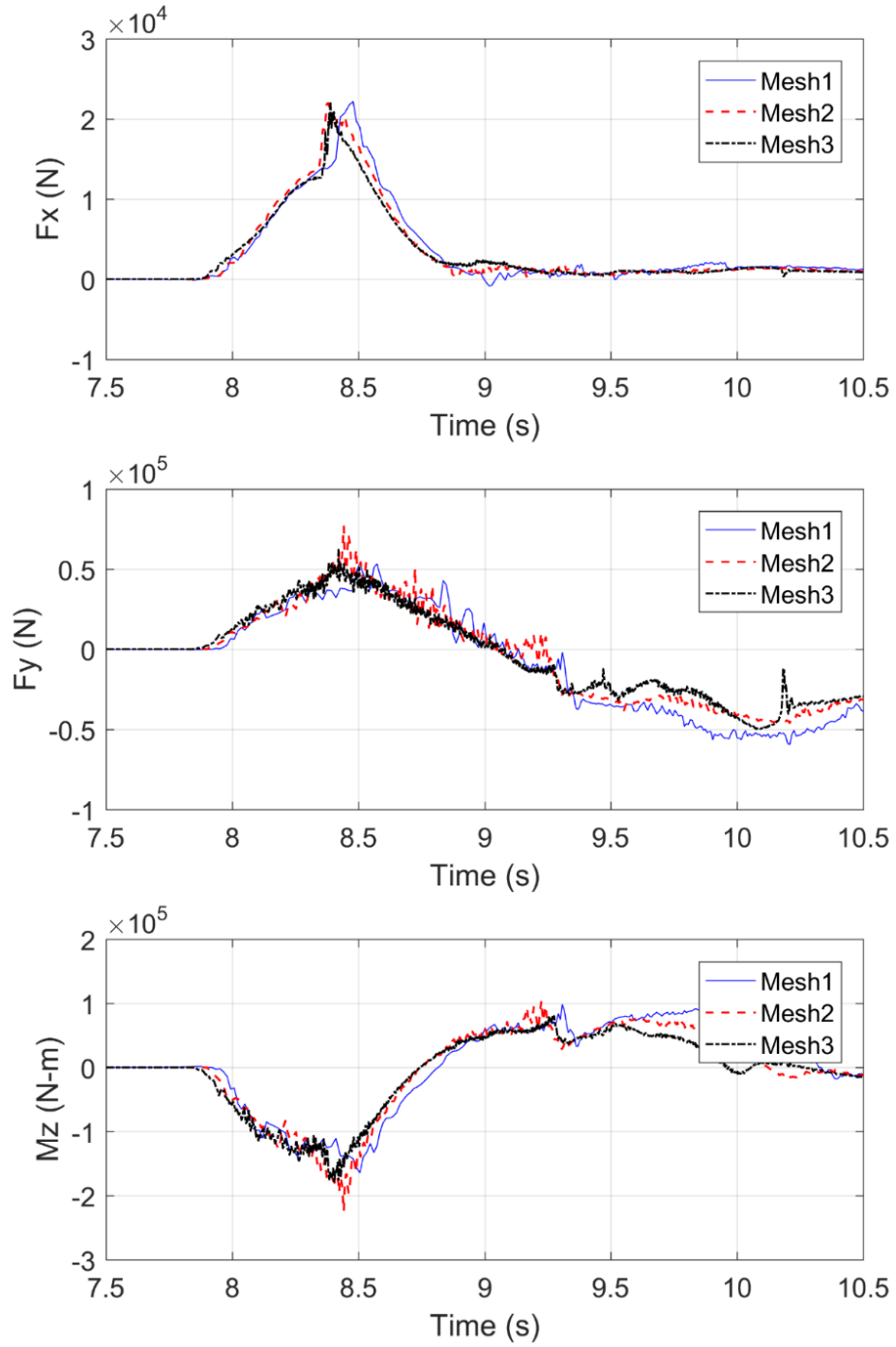
Figure 2.4: Applied forces and overturning moments (OTM) on the Winchuck River Bridge for η=1.65m and three different mesh-sizes

23
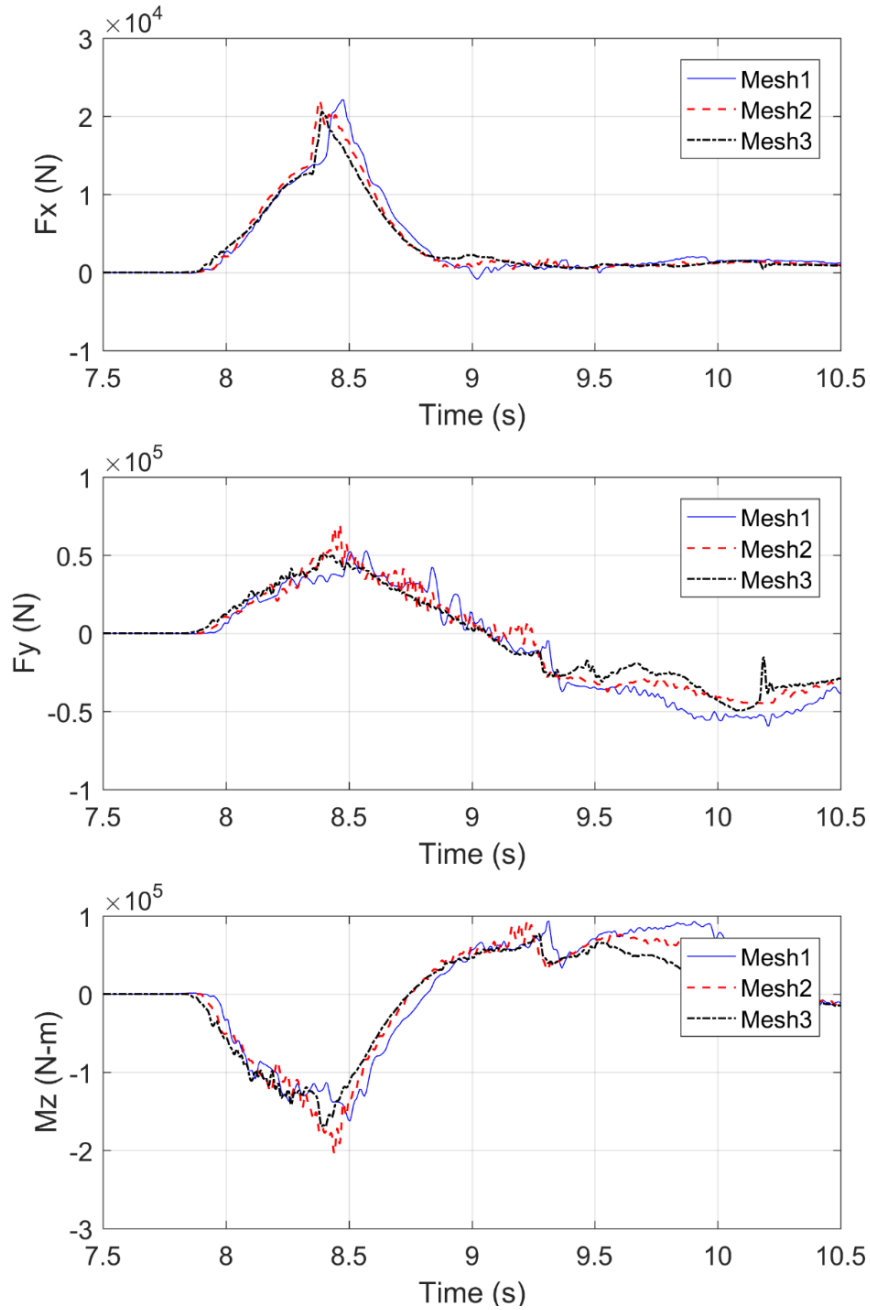
Figure 2.5: Filtered forces and overturning moments on the Winchuck River Bridge for H=1.65m and three different mesh-sizes

2.2.3 Results and discussion

Figures 2.6 and 2.7 plot the time histories of the forces (Fx and Fy) and overturning moments (Mz) for a smaller and a large solitary wave. Note that in all the graphs the forces and moments are positive when they point in the positive direction of the axes shown in Figure 2.1. In the numerical model the positive direction of the x is in the direction of the wave propagation, y is positive upwards and z is normal to the plane of Figure 2.1 pointing outwards. As observed in

the previous studies (Hoshikuma et al., 2011; Istrati et al., 2018; Xiang et al., 2020) the bridge is simultaneously subjected to lateral force, uplift force and moment at the beginning of the inundation. As the wave propagates through the structure the horizontal force decreases, while the vertical force and overturning moment change in severity and direction. Interestingly, the new results reveal that while for small wave heights the loads are governed by a long-duration quasi-static component, as the wave increases in height more transient (short-duration) peaks appear in the load histories, which increase the overall magnitude. This could be attributed to the fact that larger wave heights are associated with larger particle velocities, which govern the slamming loads.

Another major finding of the new analyses, demonstrated by the normalized load histories, is that although for small wave heights the maximum uplift force occurs after the occurrence of the maximum horizontal force and overturning moment, for large waves this is not the case. In fact, in the latter case the horizontal and uplift force, as well as the moment, are maximized at the same instant, meaning that the large wave heights can have a much worse effect on critical infrastructure not only due to the larger magnitudes but also due to the simultaneous applications of all the maximum loads. Moreover, the different trends between the small and large heights imply that the simplified design methodology consisting of three load cases developed in (Istrati et al., 2018) could potentially be further modified and expanded to box-girder bridges in the future, so that the critical load case can be defined as a function of the wave height.
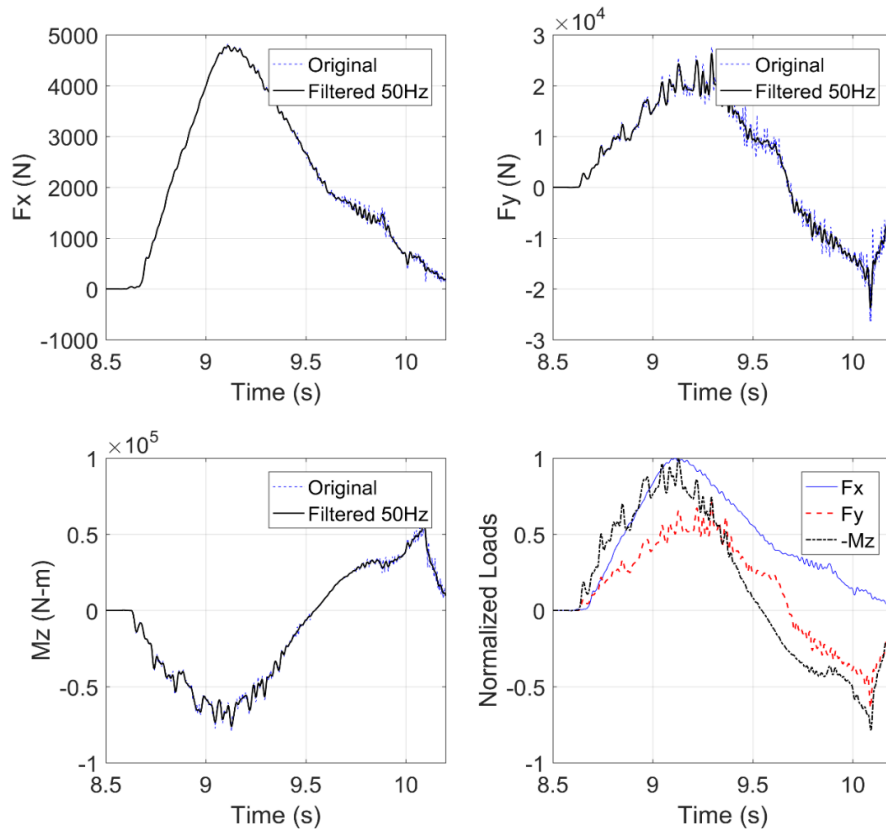
Figure 2.6: Time histories of horizontal (Fx) and vertical force (Fy) and overturning moments (Mz) applied on the Winchuck River Bridge by an unbroken solitary wave with H=1.25m

25

Figure 2.7: Time histories of forces and overturning moments applied on the Winchuck River Bridge by an unbroken solitary wave with H=2.25m

Figure 2.8 presents the maximum horizontal and uplift force, together with the maximum clockwise moment (when the wave comes from the left side of Figure 2.3). Interestingly, although the horizontal force and moment exhibit a nonlinear trend (a 2nd order fitting polynomial achieves an $R^2=0.995$), the uplift force has a smaller nonlinearity and can be approximated by a linear function with reasonable accuracy ($R^2=0.964$). Generally speaking, previous research studies (Douglass et al., 2006; Yim and Azadbakht, 2014; Istrati, 2017; Xiang et al., 2020) have shown that the total wave-induced loads on bridges have a hydrostatic component (a function of h) and a hydrodynamic component (a function of the momentum flux hv^2). However, the results of this study seem to indicate that for box-girder bridges particularly, the Fh and OTM tend to be governed by the hydrodynamic component, while for Fup (uplift) the hydrostatic component seems to be playing a major role.

Figures 2.9 and 2.10 show the load histories for the two aforementioned waves. Similarly to the case of large solitary wave heights, bores introduce significant forces and moments, which are maximized simultaneously. However, in the case of bore impact on box-girder bridges the demand is clearly governed by the transient hydrodynamic component both in terms of forces and moments. Moreover, although the investigated bores (e.g. Fig. 2.9) have similar wave

heights with the largest solitary wave shown in Fig. 2.6, the bore-induced forces and moments are significantly larger. In fact, Fh and Fup are larger by a factor of 3.9 and 2.3 respectively, while the OTM is larger by a factor of 3.2. This can be justified by the larger bore velocity, which can reach 8m/s at certain elevations, and the different distribution of fluid velocities before the impact on the offshore face, which subsequently cause a different pattern of applied pressures on the bridge. For the largest bore with a 2.50m height and a velocity up to 9m/s the forces were even larger reaching 517kN/m and 433kN/m in the horizontal and upwards direction respectively. In this case the horizontal and vertical loads were larger than the respective loads of the largest unbroken solitary wave by a factor of about 6 and 3.8.

Note that all the load histories presented in this chapter have been filtered using a 6[th]order Butterworth filter with a cutout frequency of 50Hz, unless stated otherwise. This frequency has been used in previous wave-related experimental and numerical studies (Bradner et al., 2010) and it was demonstrated that it did not remove the actual content of the recorded signal. Nonetheless, it must be stated that more work is required in order to quantify the frequency content of waves and especially tsunami-like bores that tend to introduce high-frequency peaks.
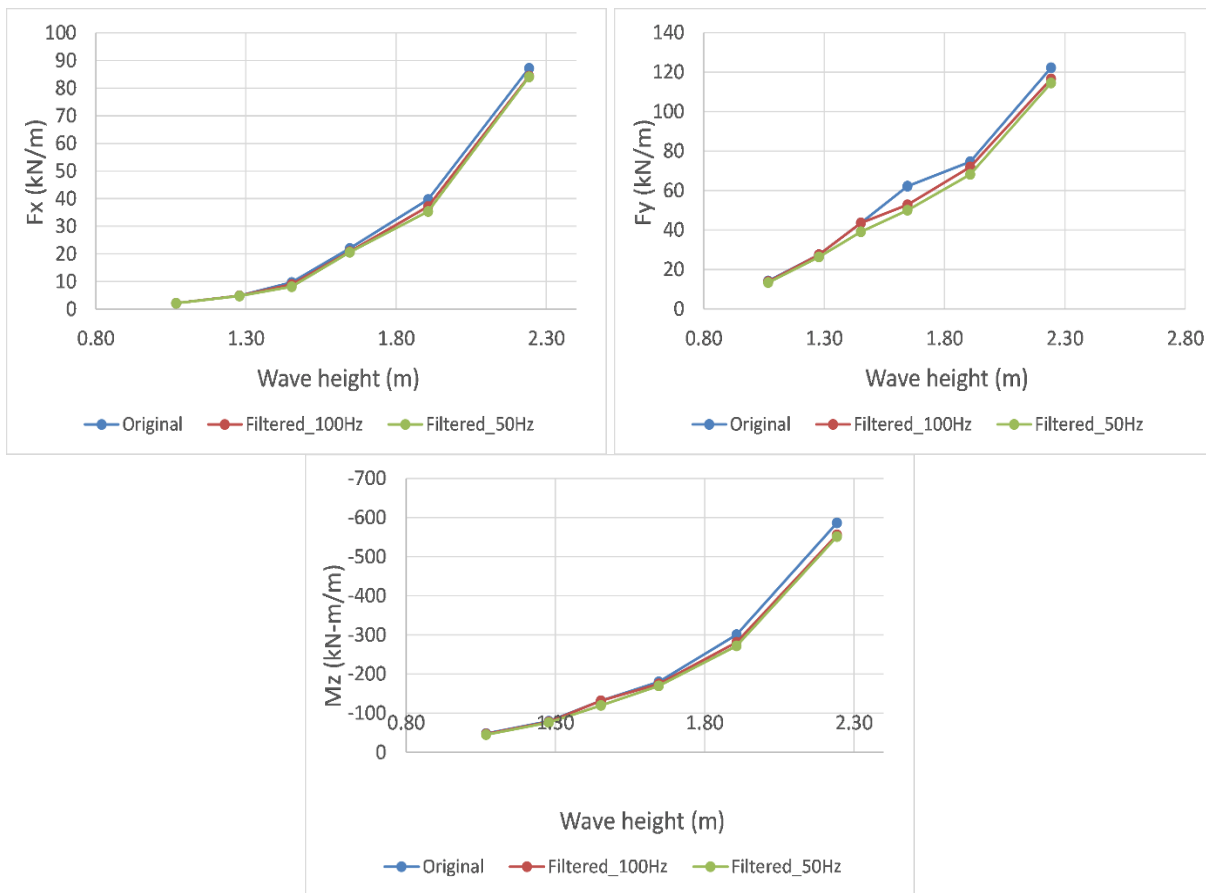
Figure 2.8: Maximum forces and overturning moments applied on the Winchuck River Bridge by unbroken solitary waves
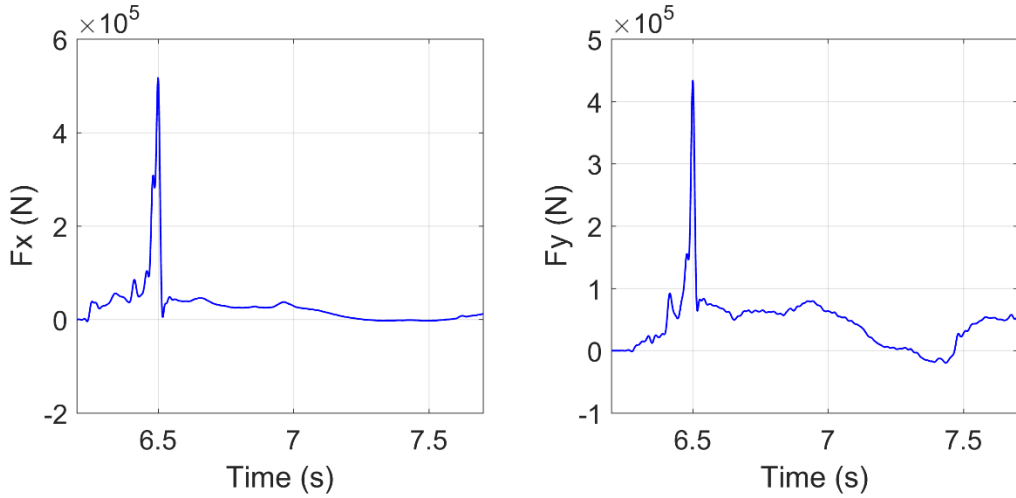
Figure 2.9: Time histories of forces applied on the Winchuck River Bridge by a 2.50m high bore
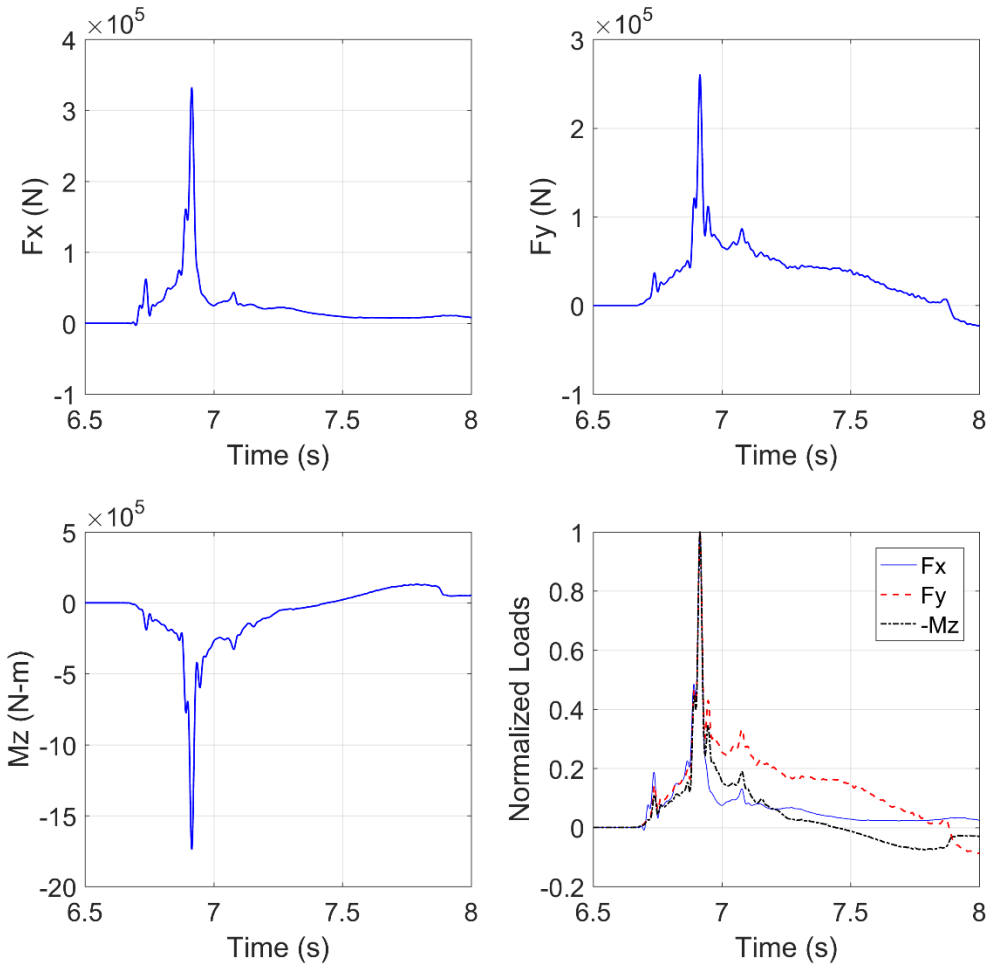
Figure 2.10: Time histories of forces and overturning moments applied on the Winchuck River Bridge by a 2.20m high bore

28

2.3   SCHOONER CREEK BRIDGE

2.3.1 Description of structure, models and hydrodynamic conditions

The second bridge that was investigated is the Schooner Creek Bridge, which is a straight open-girder bridge with concrete girders and diaphragms, which do not extend along the whole height of the girders. The elevation of the bridge ranges between 23.47ft and 29.15ft with the south end being elevated higher than the north end, as shown in Figure 2.11. The deck has a super-elevation that ranges between 0.286° and 1.43°. Following the same approach as in the previous section, the tsunami impact was simulated via two-dimensional analyses of a slice of the bridge. The slice was assumed to be located at the mid-length of the third (from the left) span. Given the variable super-elevation along the bridge length (down to 0.286) in the numerical analyses the super-elevation was not considered.

The computational domain was 100m long and 14m tall, with the distance of the bridge from the inlet boundary being about 45m. The mesh-size was 10cm at the boundary of the computation domain and 5cm around the bridge (see Fig. 2.12), which is the same as the medium mesh (Mesh 2) of the previous section. A series of solitary wave heights were investigated for a water depth of 5m, which ranged between 2.15m and 3.15m, with H/d ratios between 0.43 and 0.63. All the parameters that describe the numerical models are summarized in Table 2.3.
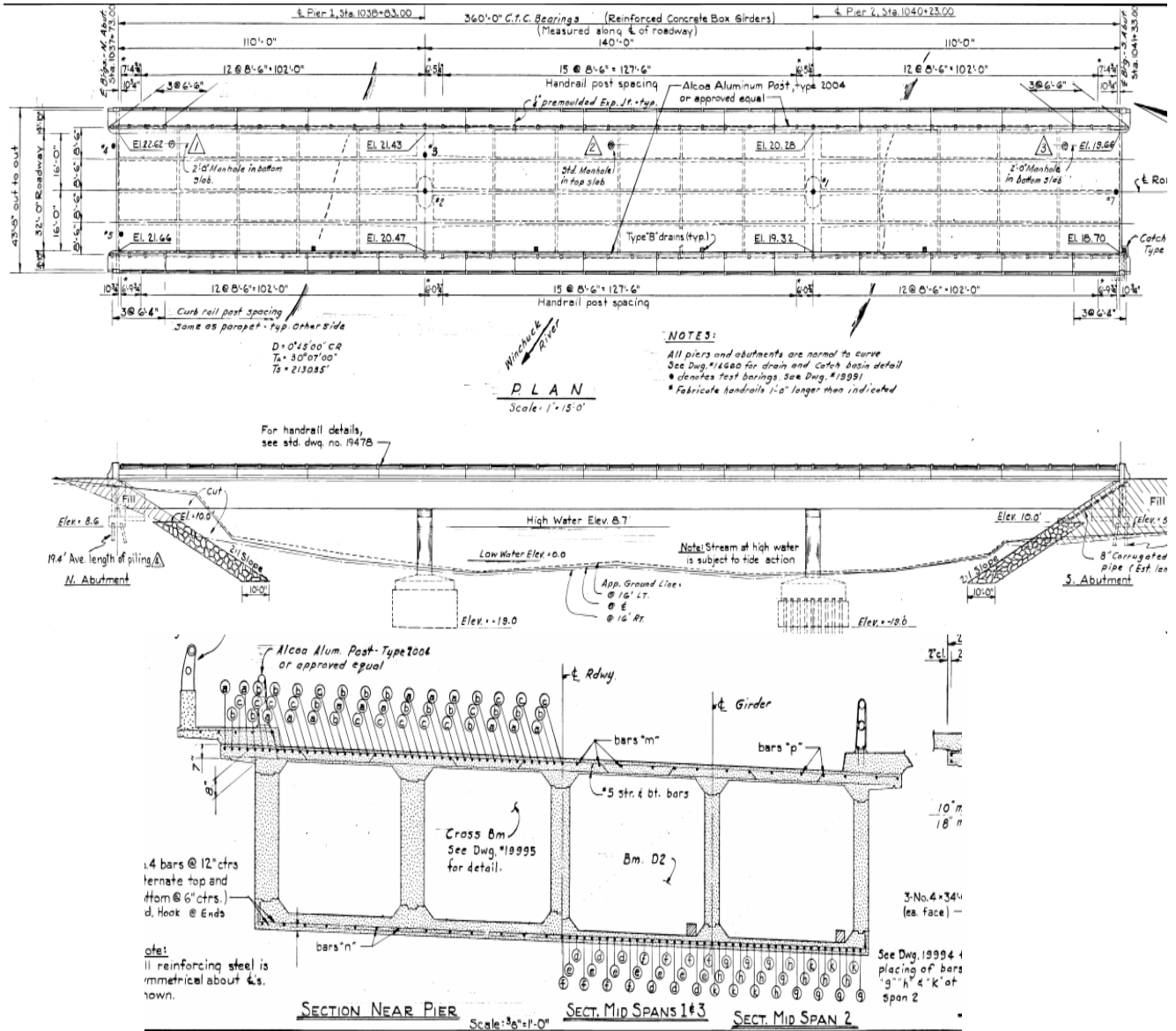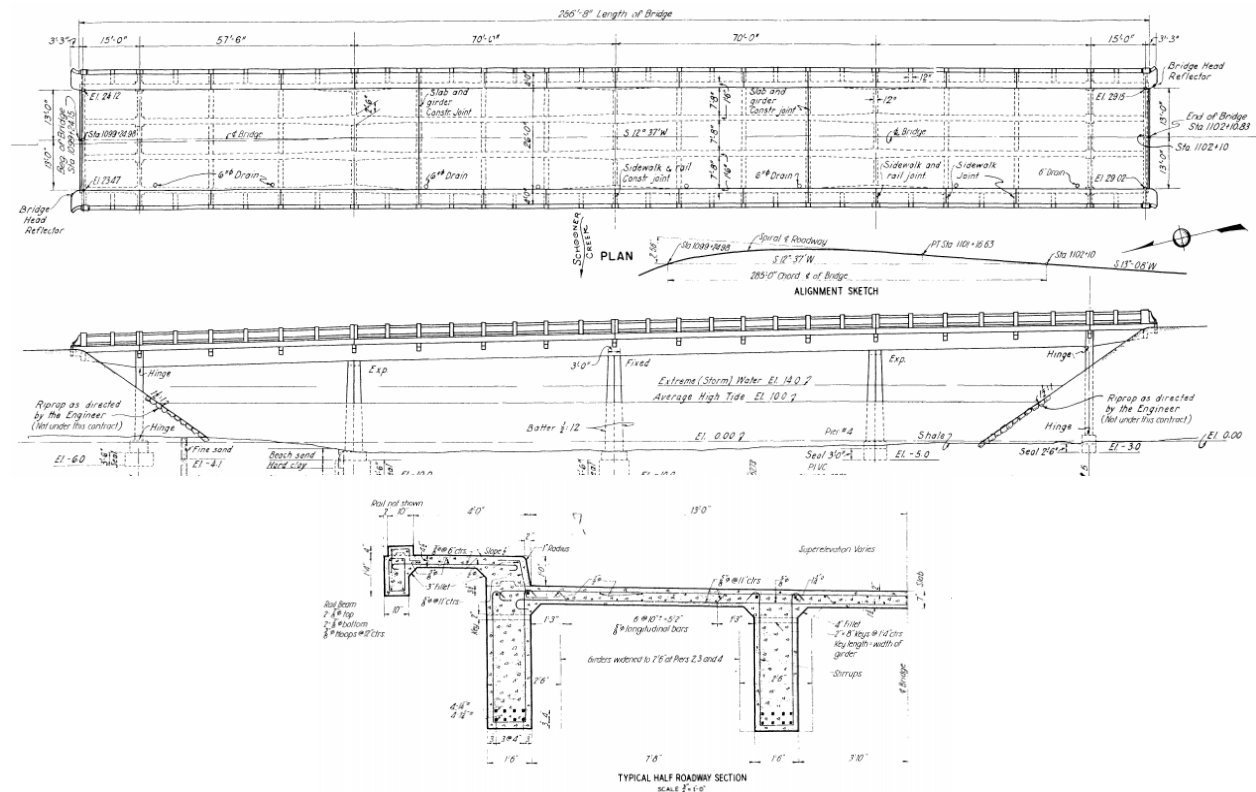

Figure 2.11: Plan view (top), elevation (center) and cross-section (bottom) of the Schooner Creek Bridge (source: Oregon Department of Transportation)
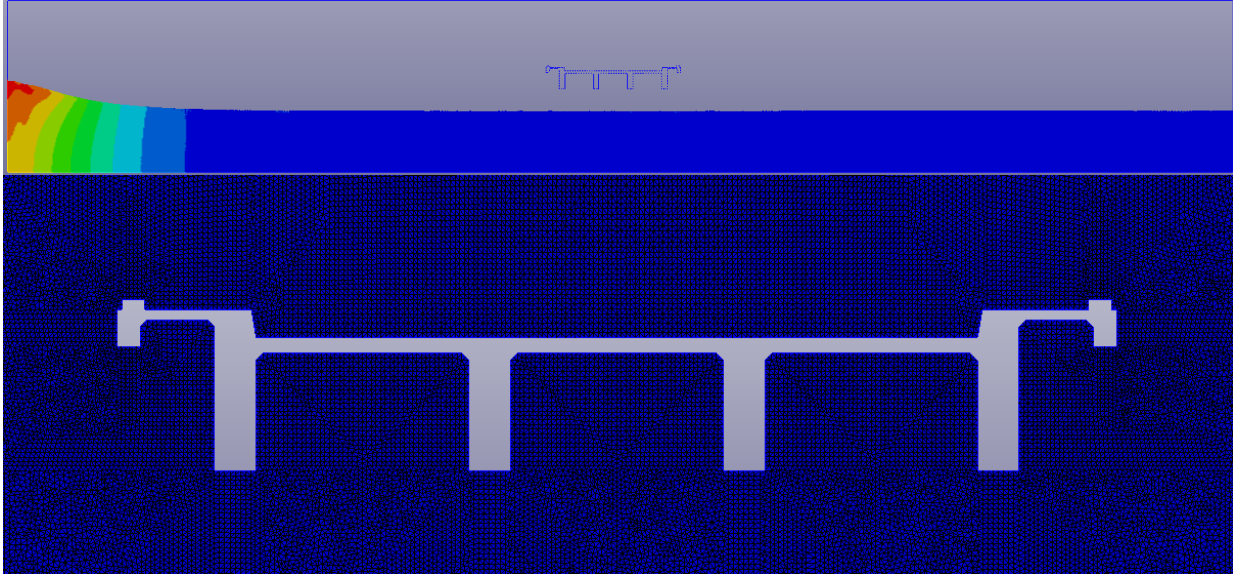
Figure 2.12: Overview of the computational domain (top) and mesh-size around the model (bottom) of the Schooner Creek Bridge

Table 2.3: Description of the Schooner Creek Bridge Numerical Models

Parameter	Description
Comp. domain	Ldm=100m, Hdm=14m
Bridge model	df=45m, Hbc=8.258m
Wave/flow	h=5m, H=2.15m÷3.15m, v=3.60m/s÷5.63m/s

2.3.2 Results and discussion

Figure 2.13 shows the loads applied on the Schooner Creek Bridge by one of the large solitary waves. Similarly to the box-girder bridge, this open-girder bridge witnesses large lateral and uplift forces simultaneously with a large (clockwise) overturning moment, which could potentially overstress the offshore bearings and connections. Contrary to the box-girder bridge though, the force histories present additional peaks both in the horizontal and vertical direction, following the initial major peak generated when the wave slams on the offshore face of the bridge. These peaks could be related to the instants that the wave impacts a different girder or chamber.

To investigate this further, Figure 2.14 presents snapshots of the fluid velocities at two instants (t=4.4s and t=4.8s), which are close to the instants that the two major uplift peaks occur in the time-histories. This figure proves that the first uplift peak occurs when the wave hits the offshore overhang, while the 2nd one occurs when the wave impacts the bottom slab of the 1st chamber, which are exactly the two first load cases described in (Istrati et al., 2018). Although at the first instant the uplift pressures are applied only on the offshore overhang, which is smaller than the area on which the pressures are applied at the 2nd instant, the former one still seems to govern the uplift demand for the particular bridge and wave height. This is because the vertical velocities are large when the wave hits the offshore overhang generating a significant slamming

component, after which the wave loses energy leading to smaller vertical velocities when the wave reaches the 1st chamber. This reveals the major role that the overhang plays when a bridge is subjected to extreme hydrodynamic loading, and implies that removing (or modifying) the overhang could potentially reduce the uplift demand both on box-girder and open-girder bridges.

Last but not least, Figure 2.15 shows the maximum applied loads on the Schooner Creek Bridge for the selected wave conditions. The nonlinear trends of Fx and OTM are consistent with the ones observed in the case of a box-girder bridge. In contrast though to the box-girder bridge, the uplift forces applied on the Schooner Creek bridge exhibit also a highly nonlinear behavior, which leads to larger uplift forces than horizontal ones for the large waves. Another fundamental difference between the Winchuck and Schooner Bridge is the shape of the overhang, with the Schooner Bridge tending to constrain the water more when the wave hits the offshore overhang. It must be clarified that in the current 2D simulations the trapped air was not considered, since it is expected that the air can (partially) escape in reality due to the fact that the diaphragms had a shorter height than the girders. However, future studies could investigate the actual percentage of the air that escapes through the sides where the shorter diaphragms are located, by utilizing three-dimensional two-phase analyses.

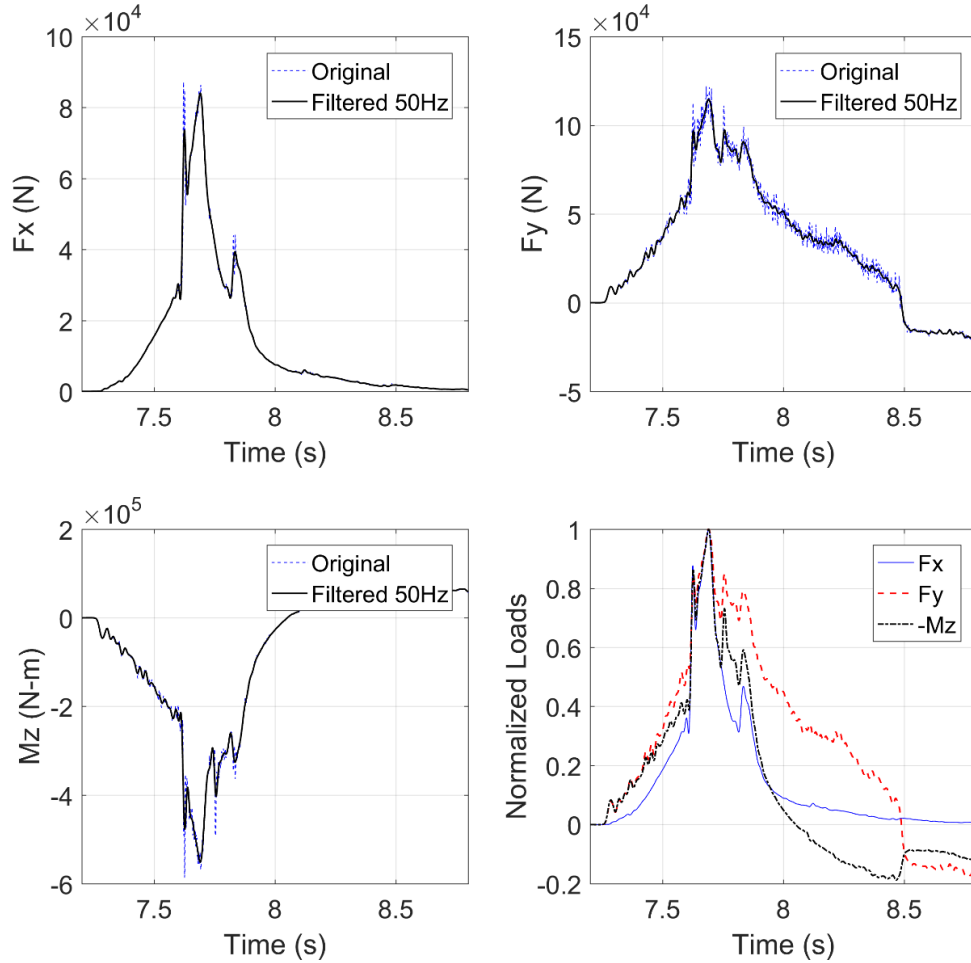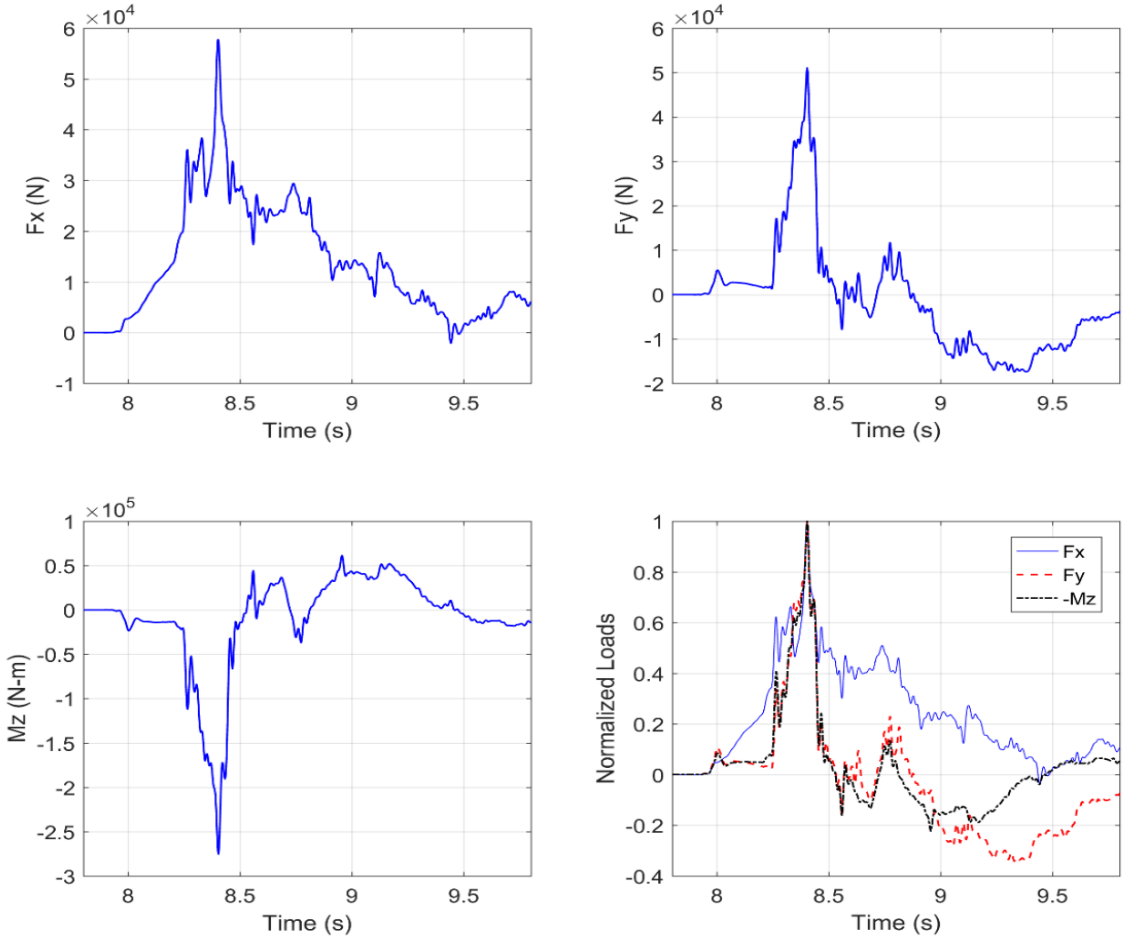**Figure 2.13: Time histories of forces and overturning moments applied on the Schooner Creek Bridge by an unbroken solitary wave with H=2.85m**

31
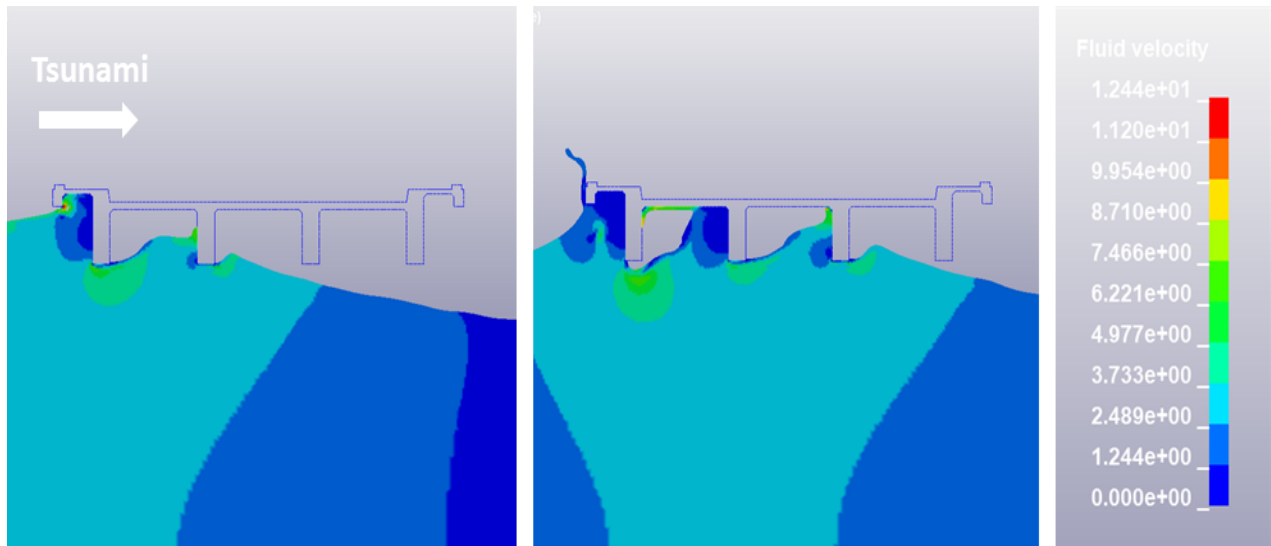
Figure 2.14: Snapshots of the fluid velocities at t=4.4s (left) and t=4.8s (right) during the inundation of the Schooner Creek Bridge by an unbroken solitary wave with H=2.85m
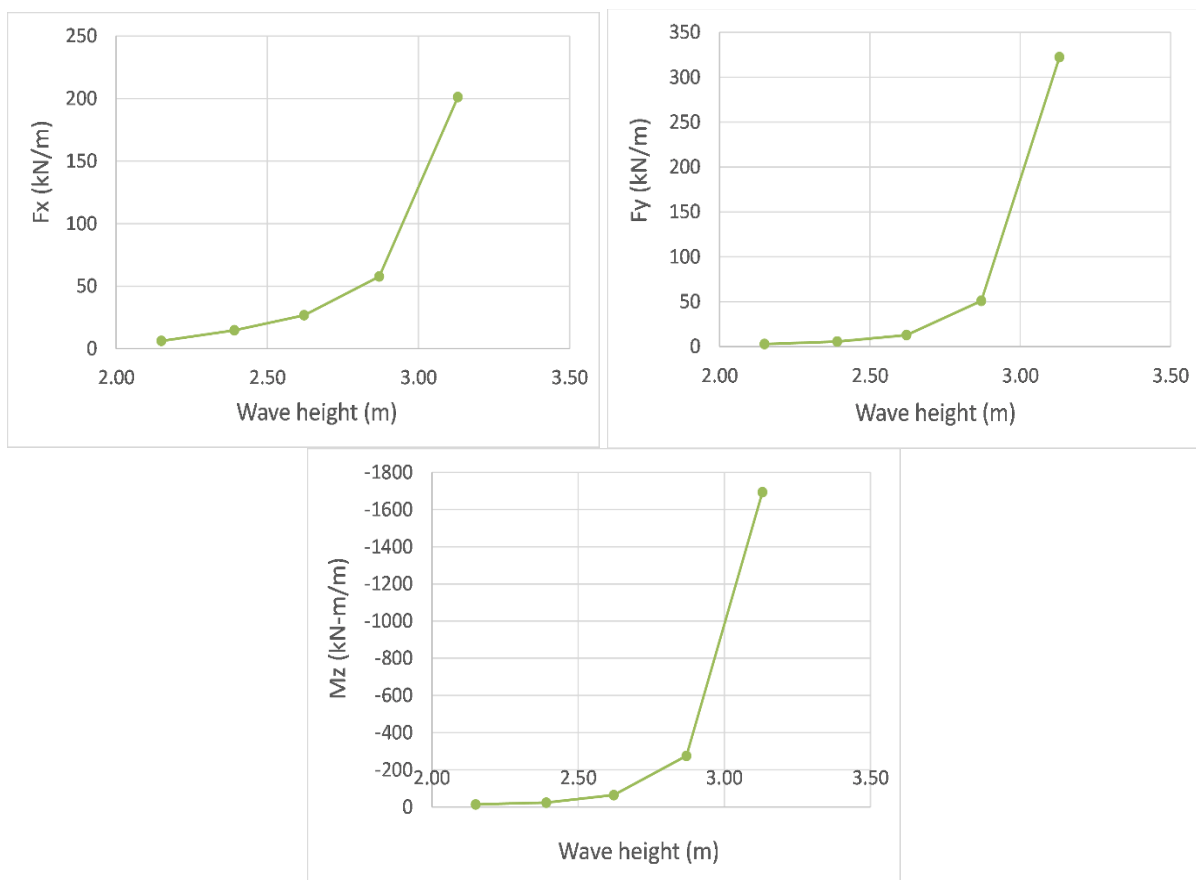
Figure 2.15: Maximum forces and overturning moments applied on the Schooner Creek Bridge by a series of unbroken solitary waves

32

2.4   LITTLE NESTUCCA RIVER BRIDGE

2.4.1 Description of structure, models and hydrodynamic conditions

The last bridge that was investigated in this study is the Little Nestucca River Bridge. This is a skewed open-girder bridge with concrete girders and diaphragms. Figure 2.16 shows that the bridge has 5 spans, 8 girders and a 34° skew angle. Therefore, in order to investigate the loads, a three-dimensional model was built (see Figure 2.17). The 3D computational domain was 100m long, 35m wide x 10m tall, which means that only one span was simulated. The mesh-size was 20cm at the edges of the computational domain and 5cm on and around the bridge, leading to about 15million nodes in total. A gap of 10cm was simulated between the side walls and the deck, assuming that those were the expansion joints that had popped-out during the preceding earthquake shaking. The investigated hydrodynamic conditions involved an unbroken solitary wave with a height of 3m and a long-duration bore with a 3.5m height and 7m/s velocity, while the water depth was 4m for both conditions. All the parameters that describe the numerical models are summarized in Table 2.4.
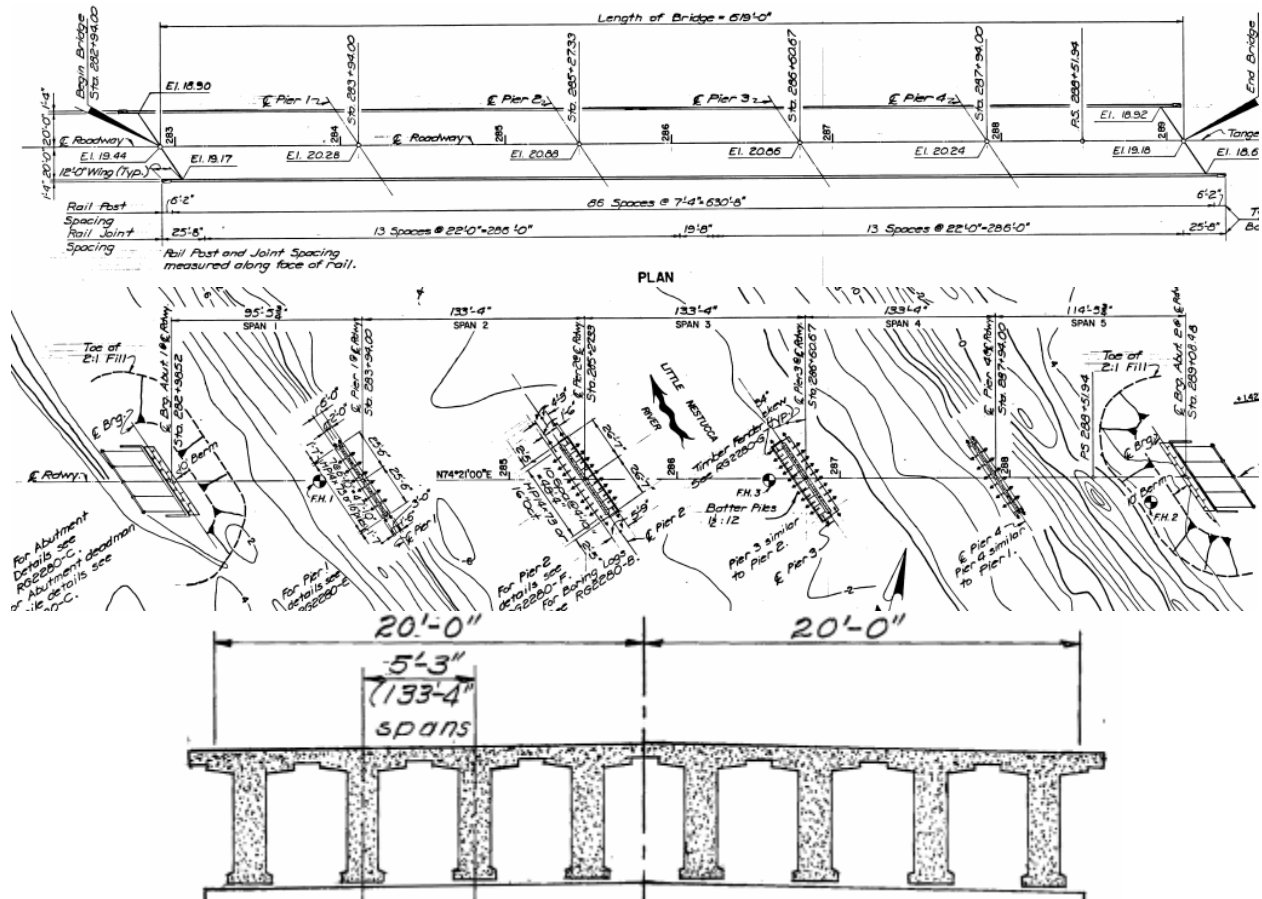
Figure 2.16: Plan view of deck (top) and foundations (center), and cross-section (bottom) of the Little Nestucca River Bridge (source: Oregon Department of Transportation)

Table 2.4: Description of the Little Nestucca River Bridge Numerical Models

Parameter	Description
Comp. domain	Ldm=100m, Hdm=10m
Bridge model	df=35m, Hbc=6.36m
Wave/flow	h=4m, H=3m÷3.5m, v=6.22m/s÷7m/s
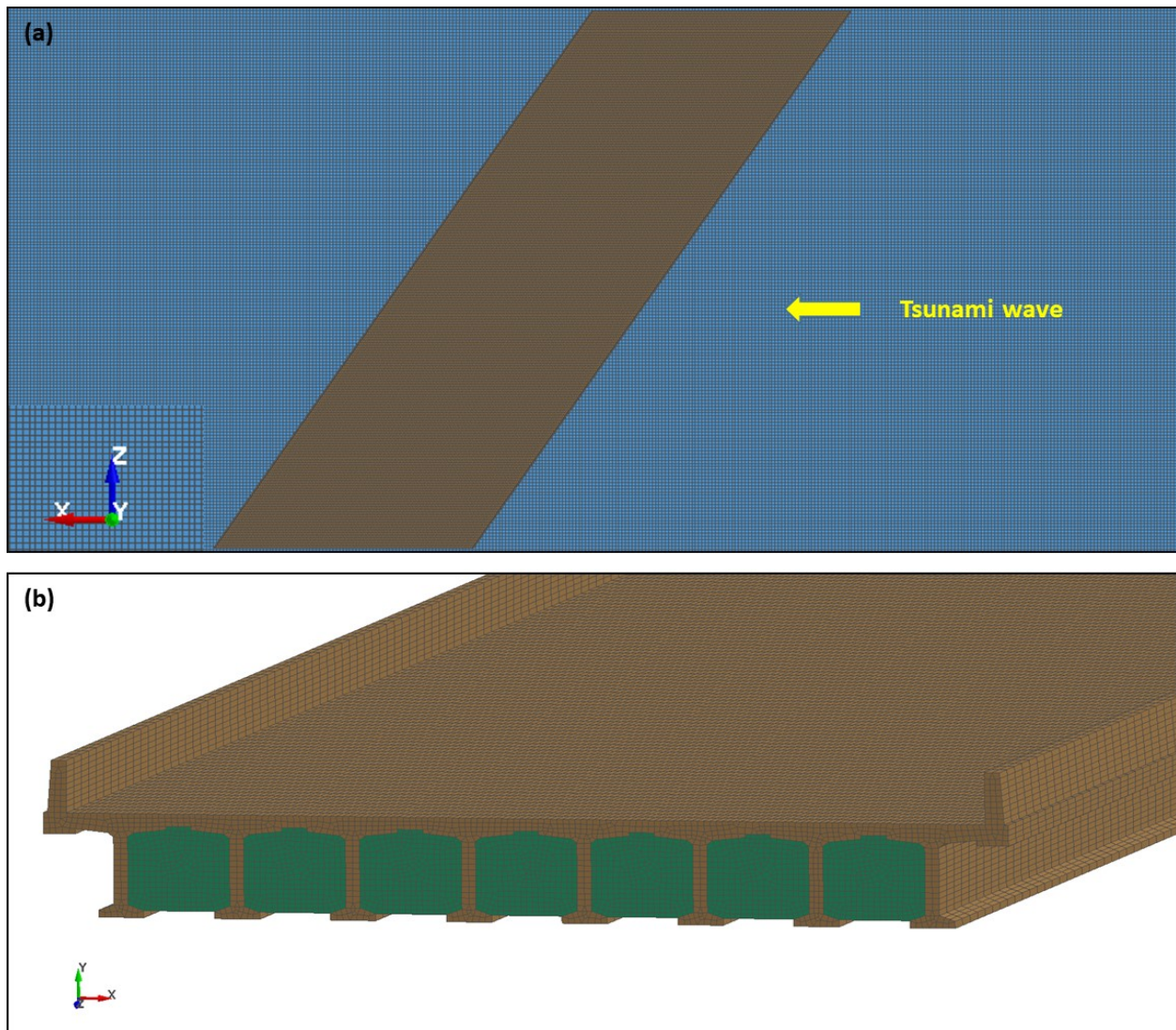
Figure 2.17: Computational model of the Little Nestucca Bridge: (a) Plan view of the model close to the bridge, and (b) 3D view of the superstructure mesh

2.4.2 Results and discussion

Figure 2.18 and 2.19 show the time-histories of the loads on the Little Nestucca River bridge, applied respectively by an unbroken solitary wave with H=3m and a bore with H=3.5m. To decipher the underlying physics and relate the estimated loads to the inundation process, Figures

34

2.20 and 2.21 show snapshots of the bridge inundation process and the distribution of fluid velocities, at selected instants. Observation of these figures can lead to the following findings:

- In contrast to straight bridges, skewed ones seems to be subjected to longer duration uplift (Fy) and lateral (Fx) forces, as well as, overturning (pitch) moment (Mz), which lack large impulsive peaks, meaning that the slamming effects are not very significant. This seems to be consistent with the experimental results presented in (Istrati and Buckle, 2020). Moreover, in the case of the bore impact the steady-state component Fx is more significant than in the case of straight bridges, since it's magnitude is about 40% of maxFx.

- On the other hand, the force histories also exhibit characteristics that are in agreement with the straight bridge, including the fact that (a) the maximum Fx and Fuplift do not occur at the same time, and that (b) the bridge is subjected initially to a negative pitch moment, which tends to uplift the offshore side of the bridge, followed by an opposite moment as the tsunami wave inundates the top of the slab.

In addition to the loads applied on straight bridges (Fx, Fy and Mz), the particular skew bridge is also subjected to a force normal to the direction of the tsunami propagation (Fz), as well as, roll (Mx) and yaw (My) moments. These latter load effects (Fz, Mx and My) do not exist in the case of straight bridges subjected to tsunami waves that propagate in the direction normal to the bridge length (90º incident angle) due to symmetry, while in the skew bridge case they exhibit the following trends

- **Fz:** The time-histories of this force seems to be exhibiting trends similar to Fx, with a long duration pulse in the direction of +z occurring at the beginning of the inundation followed by a significant steady-state component in the same direction. The direction of Fz indicates that the force is governed by the fluid pressures applied normal to the bridge span, and not by the shear stresses (since they would yield an Fz in the opposite direction). This force can have a major effect in the tsunami design of skew bridges because it is about 50% of maxFx and will increase the lateral demand on bearings, shear keys, bent caps, foundations and abutments, since their design loads will be a function of Fx and Fz.

- **My:** The time-histories of the yaw moment exhibits a positive pulse starting at the instant that the wave slams the offshore acute corner followed by an opposite moment generated as the wave propagates though the bridge and pressures are applied along the whole length of the girders. Once the bridge is permanently inundated then a steady-state positive moment (smaller than the transient moment) is generated. The yaw moment is expected to have a significant role for the horizontal demand (x and z directions) in structural components (e.g. abutment, shear key, columns etc), due to its large magnitude relative to the total tsunami induced horizontal load and the fact that it will affect the distribution of the applied loading to the two supports of each span. Considering that the normal distance between the two bent caps is 33.69m and the magnitude of My for the bore of Fig. 2.18 is about 25000kN-m, the additional Fx introduced in one of the bent caps would be 25000kN-m/33.69m=742kN, which is about 46% of the Fx introduced in the abutment by the applied total x-force (of about

3250kN equally shared by the two bent caps). This is a clear demonstration of the importance of My for skewed bridges.

- **Mx:** The time-histories of the roll moment (Mx) present similar trends with the pitch moment (Mz). It is characterized by three major long duration pulses, a negative one at the beginning of the inundation, a positive one when the wave slams the top surface, and a second negative moment at the end of the inundation process when the whole deck is submerged in water. The reason for the generation of this moment is the gradual application of the vertical tsunami pressures starting from the offshore acute corner and propagating to the rest of the bridge as it becomes inundated by the tsunami. The roll moment has a similar effect with the yaw moment by affecting the distribution of the forces in the structural components at the two ends of the span but this time in the vertical direction. This unequal distribution will in turn overstress the components of one end relative to the other one. In fact, if we repeat the same calculation as we did for My, then this moment would increase the uplift demand of one abutment by about 37%.

Figure 2.22 presents the time-histories of the loads normalized with their maximum absolute value, for the two aforementioned hydrodynamic conditions. The left and right graphs present the loads that affect the demand in the horizontal direction (Fx, Fz and My) and vertical direction (Fy, Mz, Mx) respectively. These graphs demonstrate the similarities of the trends introduced by the two wave types (solitary waves and bores) mainly during the transient inundation phase, as well as, the significant differences generated after the first pulse in the load histories. More importantly though, this figure reveals that the maximum forces and moments do not necessarily occur simultaneously, meaning that the above simplified calculations that estimated an increase of 46% and 37% respectively of the lateral and uplift demand in the two bent caps due to the application of the My and Mx, might not be exactly accurate but just an upper bound. This in turn reveals the need for further investigation that will determine the appropriate combination of forces and moments that will yield realistic demand in structural components and identify the most critical ones for the tsunami design.
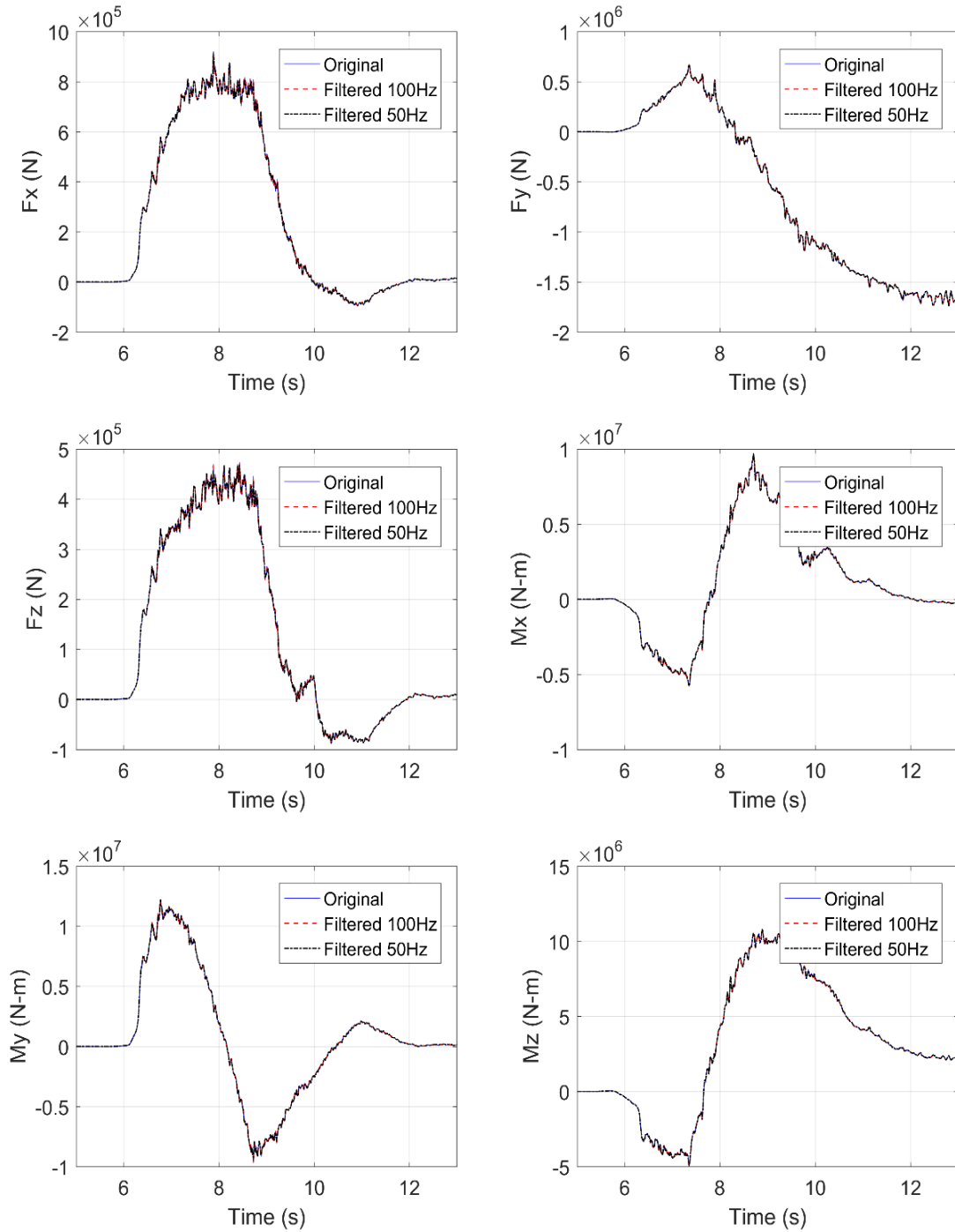
Figure 2.18: Time histories of forces and moments applied on the Little Nestucca River by an unbroken solitary wave with H=3m
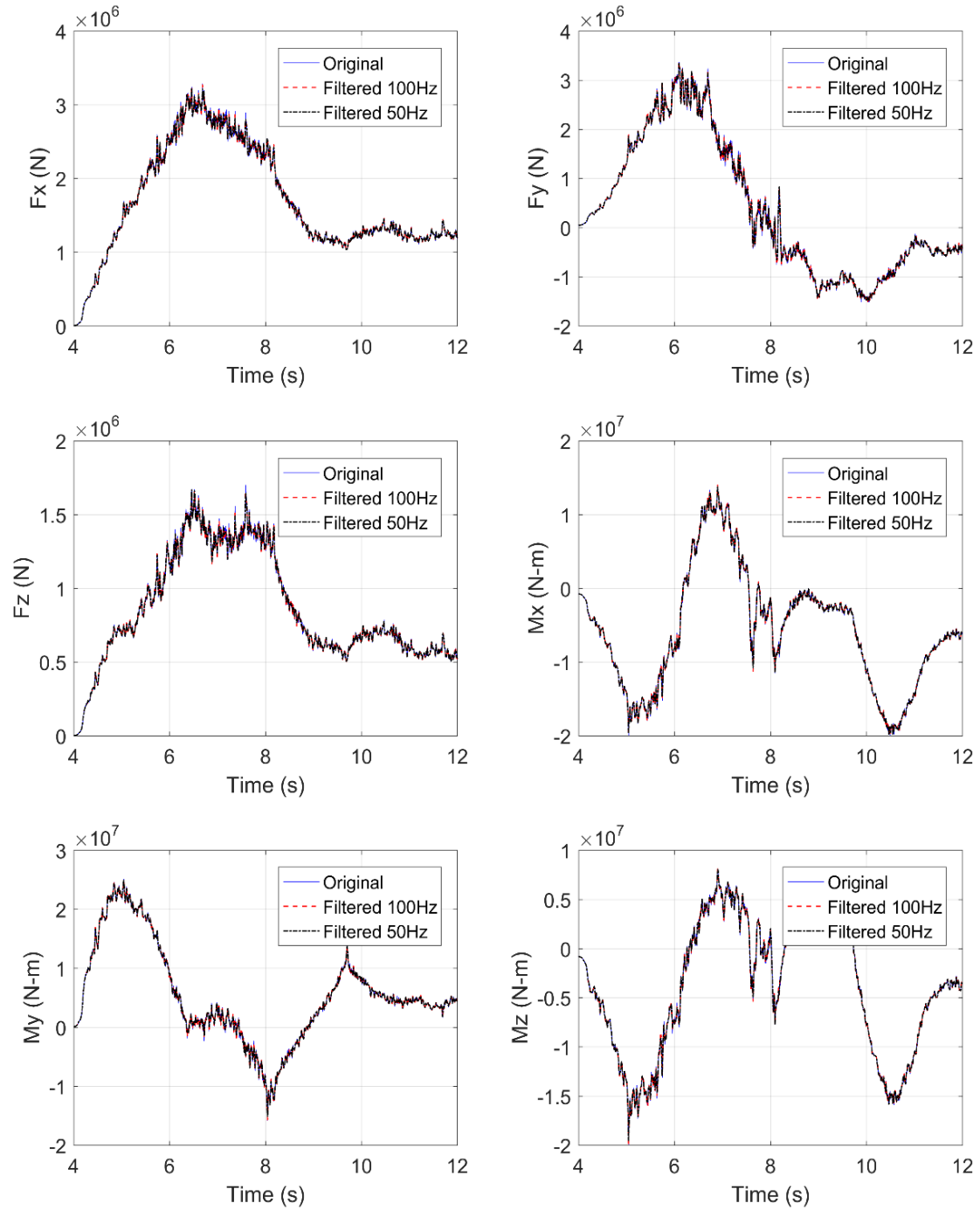
Figure 2.19: Time histories of forces and moments applied on the Little Nestucca River by a bore with H=3.5m
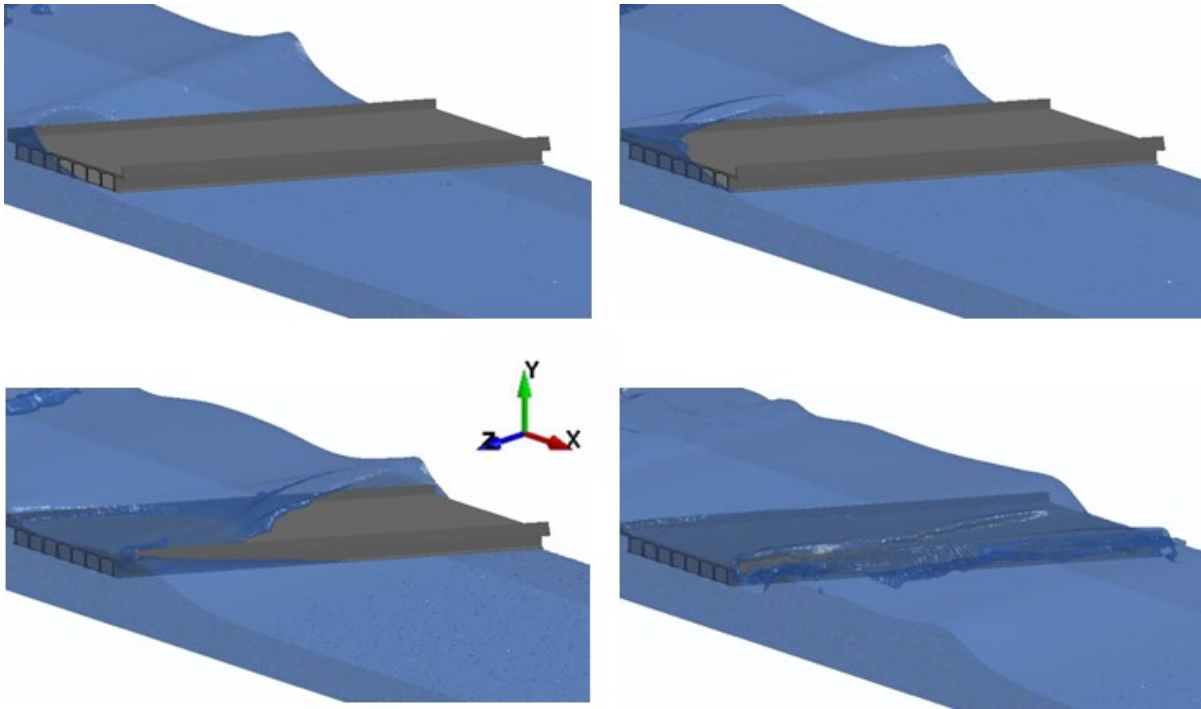
Figure 2.20: Inundation of the Little Nestucca River Bridge by a bore
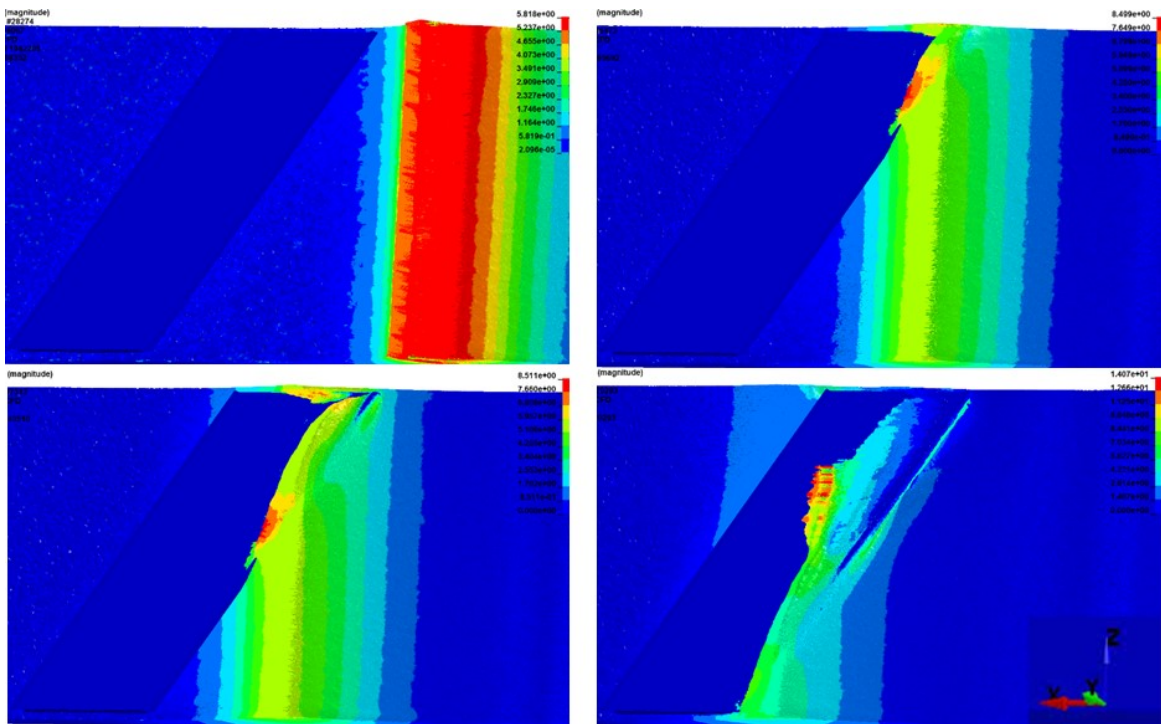
Figure 2.21: Plan view of the fluid velocities at 5.2sec (top-left), 6.8sec (top-right), 7.4 (bottom-left), and 8.7sec (bottom right) during the inundation of the Little Nestucca River Bridge by an unbroken solitary wave with H=3m
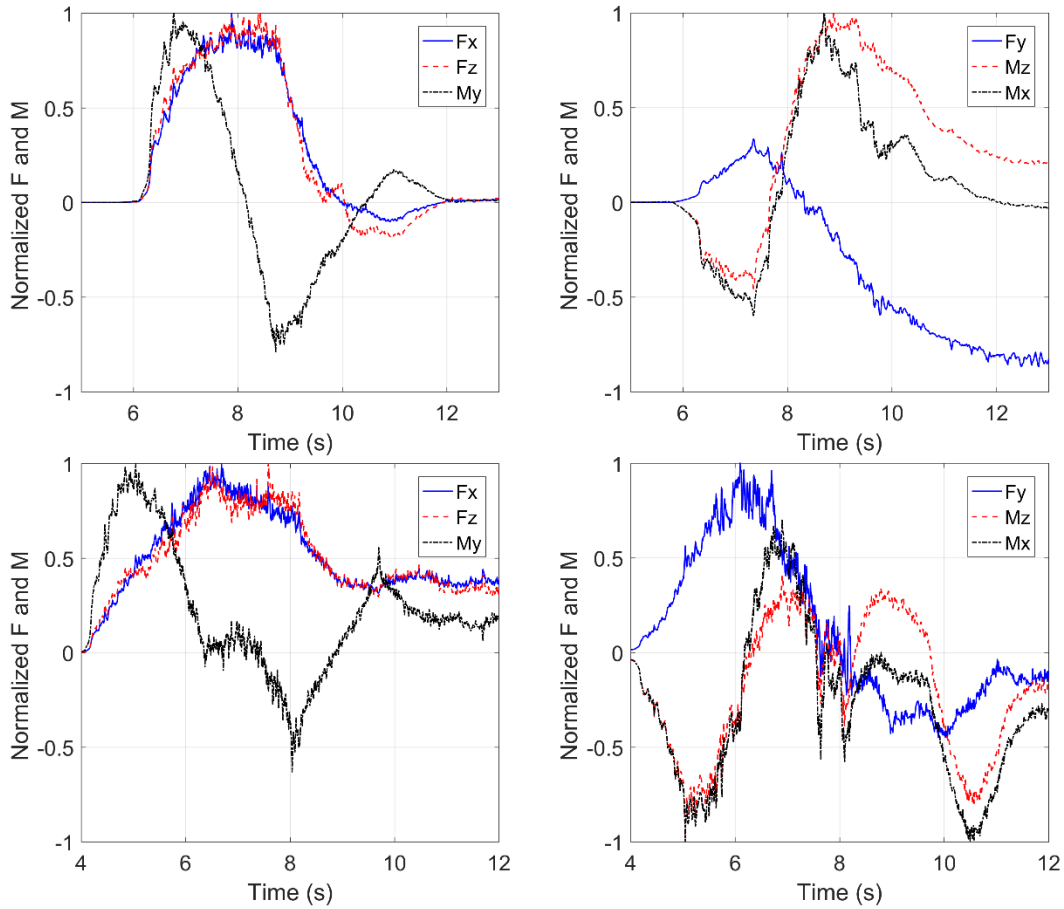
Figure 2.22: Normalized time histories of forces and moments applied on the Little Nestucca River by an unbroken solitary wave (top) and a bore (bottom)

2.4.3 2D vs 3D numerical analyses

Although as discussed earlier the Little Nestucca River Bridge is a skewed bridge for which three-dimensional (3D) analyses were deemed necessary, the authors also conducted two-dimensional (2D) analyses in order to determine the limitations of the latter approach. The main benefit of using 2D analyses is the computational cost (including the modeling effort and the actual run-time, and in some cases even eliminating the need for an HPC system), with the overall time being reduced down to 2-5% relative to the 3D ones. In these analyses the 2D slice was assumed to be located at the bent cap that supports the offshore acute corner, and the forces from the 2D analyses were multiplied by the normal length of the bridge (projection of the bridge length on the plane normal to the tsunami propagation) in order to obtain the total forces for the whole span.

Figure 2.23 plots the time-histories of the horizontal and vertical loads and demonstrates that while the 2D analyses predict large impulsive peaks at the time of the initial slamming of the wave on the offshore face of the bridge, this is not happening in the 3D analyses. This is expected since in the calculation of the 2D forces it is assumed that the slamming forces occur

40

simultaneously for all the slices along the length of the bridge, while the 3D analyses demonstrated in the previous section that this is not happening. Interestingly, despite the major differences observed in the transient inundation phase of the bridge, the 2D and 3D analyses seem to be resulting to similar steady-state loading conditions. Overall, the conclusion is that 2D analyses cannot present the hydrodynamic flow and transient tsunami-induced loads on a skewed bridge with a large skew angle (34°)
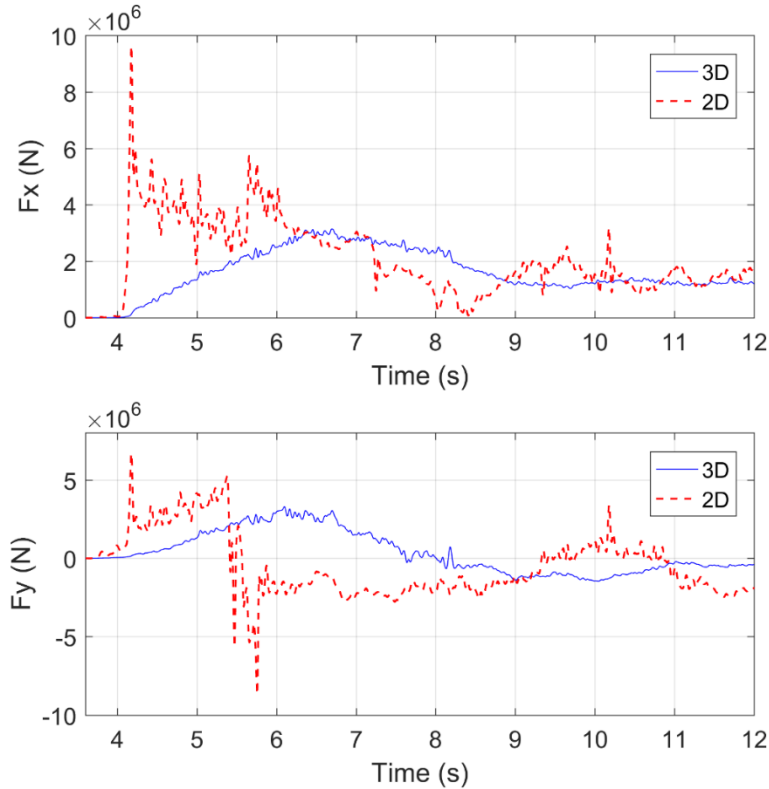
Figure 2.23: Time histories of applied loads predicted by 2D and 3D numerical models of the Little Nestucca River impacted by a bore with H=3.5m

2.5   COMPARISON OF NUMERICAL METHODS: FEM VS PFEM

Since the numerical work presented herein (based on the Finite Element Method) has been conducted as part of a larger Pooled-Fund Study TPF-5(307) led by the Pacific Earthquake Engineering Research Center, which utilized the newly developed Particle Finite Element Method (PFEM) in OpenSees (Zhu et al., 2018), it was deemed necessary to conduct a comparison of the two methods. In order to do that, the Winchuck River Bridge was selected as a baseline model and the analyses were run for H=1.20m using both the FEM method in LS-DYNA and the PFEM method in OpenSees. Due to differences in the modeling assumptions, the numerical model of section 2.1 was adjusted (moved downwards 0.21m in order to have a 6m elevation at the center of the top surface of the deck, and also used an opposite super-elevation) in order to match the numerical model in OpenSees. The results shown in Figure 2.24 reveal the overall good agreement of the two methods and solvers. The predicted trends were similar for both the horizontal and vertical forces. In fact for the horizontal force a surprising agreement was

observed both in the maximum peak and the first positive pulse, with some differences occurring in the negative horizontal part. On the other hand, for the vertical force the trends are also similar with a major uplift pulse followed by a significantly lower downward one. However, the FEM method seems to predict a larger magnitude of the uplift force by up to 40%, with this percentage being significantly reduced if the high-frequency peaks are filtered.
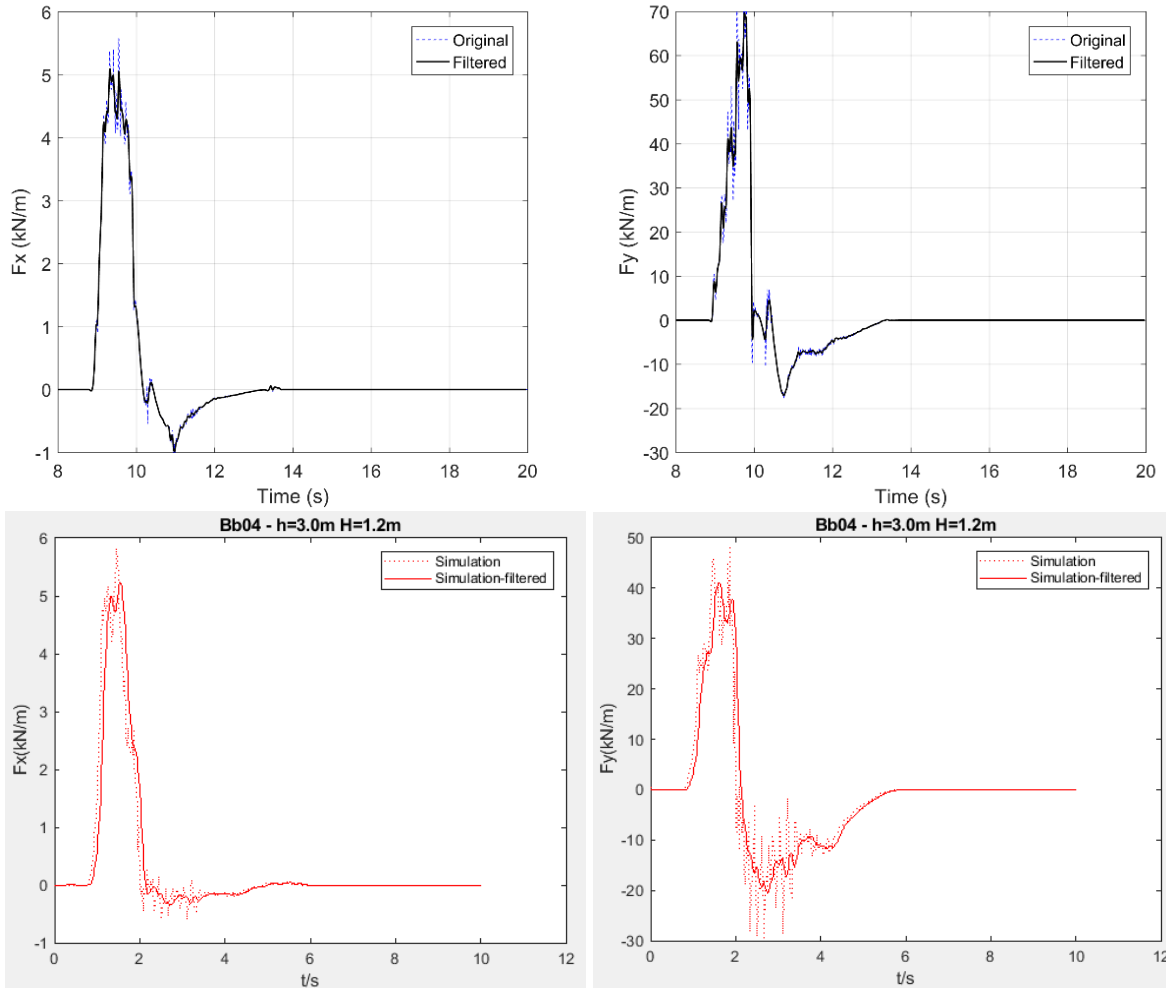
Figure 2.24: Horizontal and vertical forces predicted by the FEM in LS-DYNA (top) and the PFEM in OpenSees (bottom: courtesy of M. Scott & Z. Xie)

Note that the FEM analyses were conducted using a 5cm mesh-size around the bridge deck and 10cm at the boundaries of the computational domain, meaning that additional mesh-sizes (e.g. a smaller one) could be investigated in the future. The objective of this comparison was not to match perfectly the results of the two methods by identifying the optimal numerical settings, but instead to conduct a first comparison by utilizing reasonable modeling assumptions for both solvers.

3.0   TSUNAMI LOADS ON SKEW BRIDGES

3.1   DESCRIPTION OF NUMERICAL MODELS AND PARAMETRIC INVESTIGATION

Given the complex transient loads observed in the numerical simulations of the Little Nestucca River Bridge, which was a skewed open-girder bridge, it was decided to conduct a parametric investigation of the role of skew angle in order to shed light on the role of this parameter. Utilizing the validated 3D computational model (see Chapter 1) of an open-girder skewed bridge with three steel I-girders and a 46.6º skew angle tested in prior hydrodynamic experiments, new models with different skew angles were developed. In fact, this chapter will present the results from seven different bridge models with skew angles equal to 0º, 5º, 10º, 15º, 20º, 30º and 46.6º. As shown in Figure 3.1, all the models had the same cross-section at the left abutment (top side of the plane view) but different lengths, which were calculated based on the constant width of the wave flume and the skew angle of the bridge. Therefore, the lengths of the seven specimens were 3.46m, 3.473m, 3.513m, 3.582m, 3.682m, 3.995m and 5.036m. In all the cases the initial water depth was 1.15m and the models had an elevation of 1.72m at the top of deck, apart from one case where the deck was moved 10cm higher in order to investigate the effect on the observed trends.
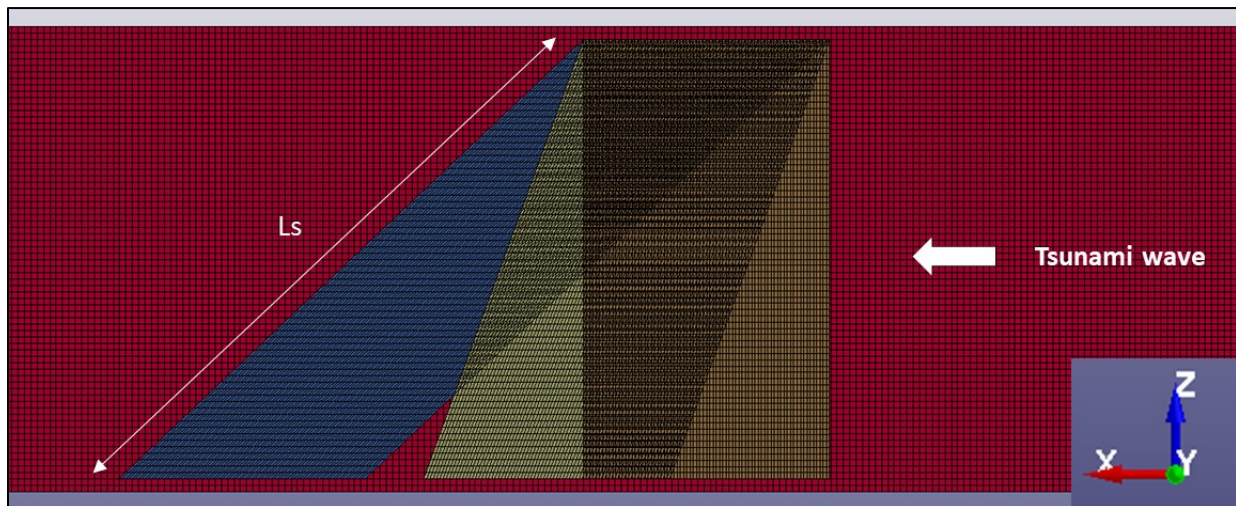
Figure 3.1: Overview of numerical models used for the parametric study of skewed bridges

All the skewed models of the baseline bridge were subjected to unbroken solitary waves with heights between 0.65m and 0.75m, broken solitary waves/short-bores, and more realistic long duration tsunami-like bores. In fact two different long-duration bores with heights in the range of 0.67-0.70m and particle velocities up to 2.5m/s. In addition to the baseline open-girder bridge model with three girders and a total width of 1.94m, it was decided to investigate the tsunami-induced loads on a wider bridge in order to check if the observed trends with the change of the skew angle were affected by the width of the superstructure. Therefore, as shown in Figure 3.2,

the baseline model was modified by adding two more girders (and chambers) with the same spacing as the existing ones, increasing the width by about 75% and reaching a value of 3.39m. In addition to the effect of the superstructure width and inspired by the fundamental differences of the tsunami-induced loads observed in the case of straight box-girder bridges relative to open-girder ones, it was deemed critical to investigate the effect of the skew angle on the former type of bridges. To that end, the baseline model was modified and a box-girder specimen with the same overhang, cross-section width and bridge height was constructed as shown in Figure 3.2.
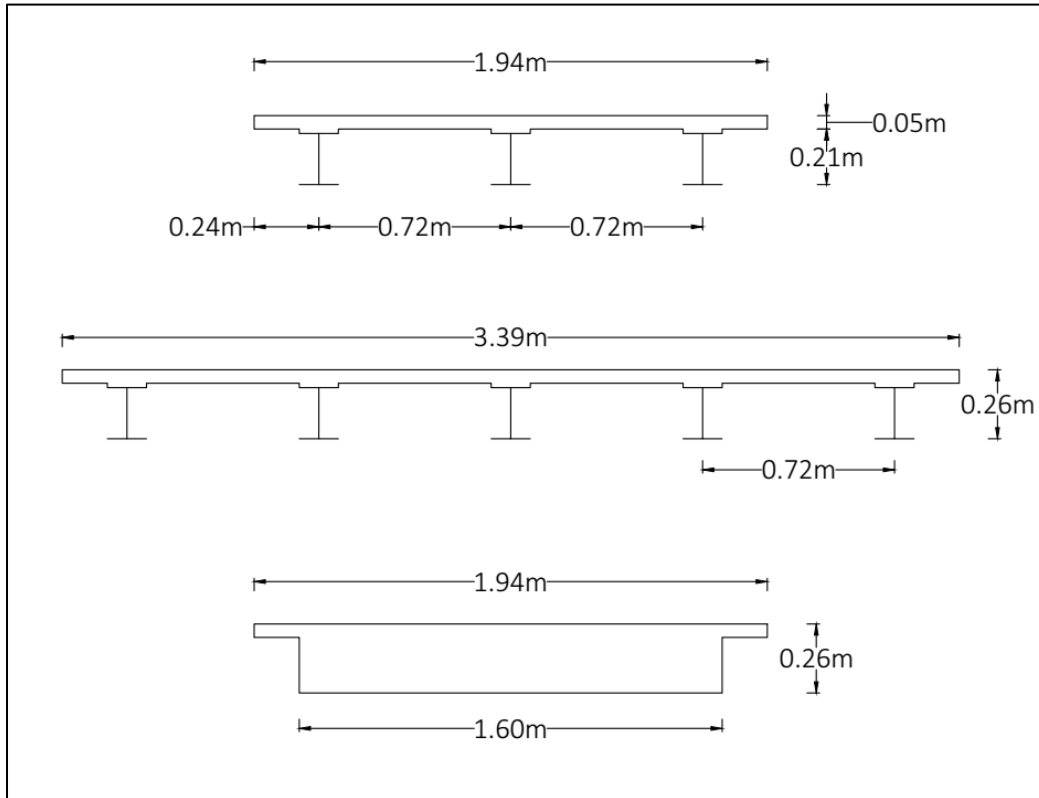
Figure 3.2: Baseline open-girder model (top), wider open-girder model (center) and box-girder model (bottom) used in the parametric investigation of the effect of skew angle

3.2 OPEN-GIRDER BRIDGES

3.2.1 Solitary waves

This section will present some selected results for unbroken solitary waves. Figure 3.3 shows the time histories of the forces and moments in all three directions for the seven skew angles. While these time-histories are helpful for understanding the physics and complexity of the transient hydrodynamic loads applied on skewed bridges, the following figure (Figure 3.4) shows the change of the maximum loads as a function of the skew angle. This could prove more beneficial for design purposes. Inspection of these two figures leads to the following findings:
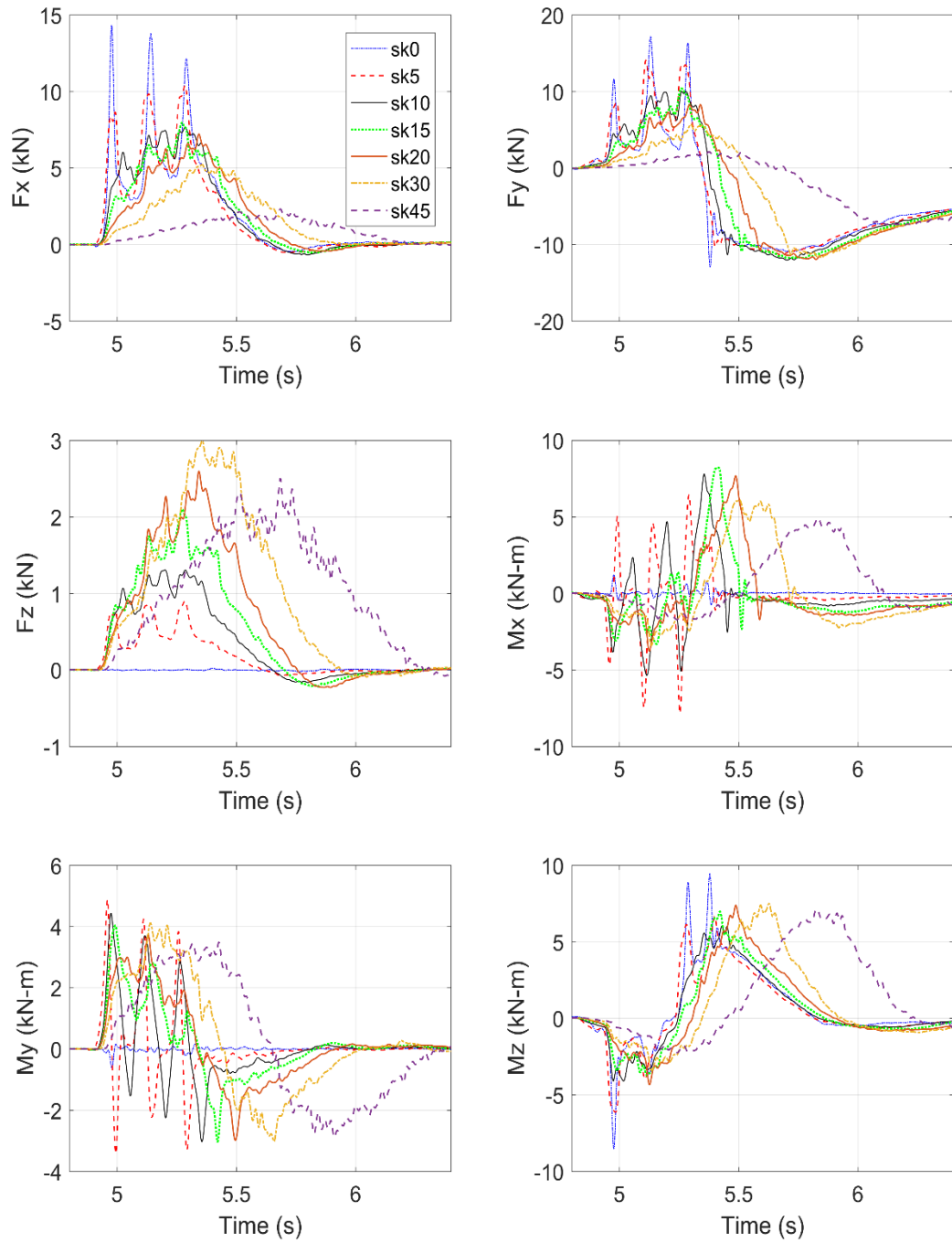
Figure 3.3: Load histories for different skewed bridges impacted by an unbroken solitary wave with H=0.75m
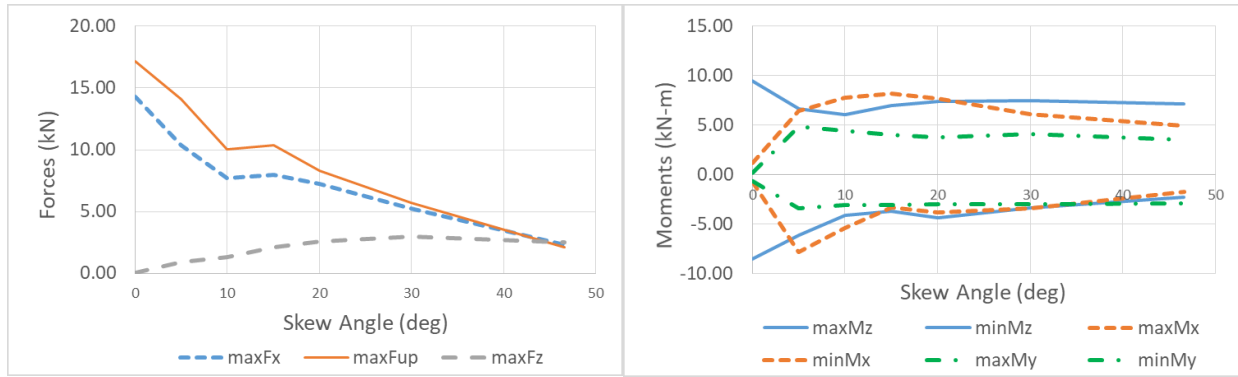
Figure 3.4: Maximum forces and moments applied on a skewed bridge by an unbroken solitary wave with H=0.70m, as a function of the skew angle

- **Fx and Fy**: As observed in the analytical results of Little Nestucca River Bridge, skewed bridges in contrast to straight ones, are subjected to longer duration uplift (Fy) and lateral (Fx) forces with less or without any impulsive peaks. The parametric investigation reveals that these forces decrease almost linearly with the increase of the skew angle and at 46.6o are reduced down to 20% of the value of a straight bridge. This is partially due to the reduction of the impulsive peaks generated by the slamming of the bore on a girder (Fx) or a chamber (Fup), which for skew angles larger than 20o are negligible. However, the further reduction is also caused by the reduction of the long-duration pulse, as demonstrated by the differences between the results of 30o and 46.6o skew angle.

- **Mz:** The overturning moment histories are also influenced by the skew angle, with the absolute value of the magnitude of the negative Mz (minMz) being significantly reduced with the existence of a skew angle. In fact, while for straight and skewed bridges with angles smaller or equal to 10o the negative moment is maximized at the beginning of the inundation when the bore slams the offshore girder and overhang (Istrati et al., 2018)). This negative moment generates significant uplift in the offshore bearings. For larger angles the maximum occurs later in the inundation process meaning that the underlying physics change and the overhang has a less significant effect. Interestingly, while the negative maximum moment (minMz) drops down to 26% at a 46.6o skew angle (relative to the respective value of the straight bridge), the positive maximum moment, witnesses only a small reduction and drops to 76%. Please note that the positive maximum moment occurs after the partial inundation of the top slab of the superstructure, this in turn indicates that the biggest effect of the skew angle is on the slamming phase where the short-duration impulsive pressures are applied on the bridge. Last but not least, it must be noted that in contrast to the reduction of Fx and Fy, which were seen to follow a nearly linear trend with the increase of the skew angle, the Mz follows a more nonlinear trend with the largest relative reduction occurring up to a skew angle of 10 degrees.

- **Fz**: In addition to the force (Fx) in the direction of the tsunami propagation, skewed bridges witness also forces normal to this direction. In particular, this force (Fz) increases with the skew angle and becomes about 57% and 108% of maxFx for skew

angles equal to 30o and 46.6o, respectively. Interestingly though, the latter case does not witness the largest Fz and this could probably be attributed to the wavelength of the solitary wave, which might not be long enough in order to apply simultaneously large pressures on the whole length of the superstructure. The Fz force should be considered in the tsunami design of skewed bridges, because it generates out-of plane horizontal loads in the bearings and connections that could potentially lead to the unseating of the superstructure.

- **Mx and My**: Another difference with straight bridges is the application of large roll (Mx) and yaw (My) moments on skewed bridges. The time-histories of Mx and My present similarities and are characterized by three distinct short-duration pulses (with positive and negative values) corresponding to the number of girders (affects My) and chambers (affects Mx). The time-histories of Mx and My exhibit a negative and positive pulse respectively starting at the instant that the wave slams the offshore acute corner followed by an opposite moment generated as the wave propagates through the bridge. As the wave propagates pressures are applied on the remaining length of the girders (or chambers) until it reaches the obtuse corner of the same girder. This process keeps repeating as the wave flows across the bridge. The relationship between these moments and the skew angle is rather complex, since their magnitudes seem to increase with the increase of the skew angle (observed at 5 o and 10 o), however, for larger angles these moments remain constant or can even decrease. These moments can have a critical effect on the performance of bridges due to their large magnitude and the fact that:

  o the yaw moment My generates out-of plane horizontal loads (in the z direction) that could result in the unseating of the deck and generates an unequal distribution of the total Fx force to each bent-cap or abutment, and

  o the roll moment (Mx) results in the unequal distribution of the uplift force to the two supports of a skewed deck, overloading the structural components of one support.

Interestingly, the above observations and findings seem to indicate that:

a) straight bridges witness the largest Fx, Fup and Mz magnitudes,

b) the skewed bridge with the largest skew angle (46.6) witnesses the largest Fz force with simultaneously large Mx and My,

c) the most severe overall demand might be applied on skewed bridges with small skew angles (e.g. 5o).

The overall demand (item c) is attributed to the fact that such bridges still witness significant impulsive peaks in the loads, which means that the Fx, Fup and Mz do not reduce significantly (e.g. about 20% reduction relative to the straight bridge), while they simultaneously witness some of the largest Mx and My. Additional investigation is required in order to identify the most critical skew angle.

3.2.2 Long-duration bores

Figure 3.5 shows the time histories of the forces and moments in all three directions for the seven skewed bridge models subjected to a long-duration bore with a height of 0.70m and velocity of 2m/s (at the inlet). Moreover, Figure 3.6 presents the change of the maximum loads as a function of the skew angle for two different bores. For the second bore (shown in the bottom graphs of Figure 3.6) the height and velocity at the inlet were 0.70m and 1.75m/s respectively and the bridge specimens were elevated by 0.10m in order to see if there will be any significant effects on the observed behavior. Clearly these two figures demonstrate that:

- The effect of the skew angle on the bore-induced bridge loads is similar to the one observed for unbroken solitary waves. One of the major differences is that in the case of the long-duration bores the loads reach a steady-state solution with a practically constant magnitude of forces, which is similar for all the skew angles. This can be justified by the fact that all the models with the different skew angles have the same in-plane area, and steady-state forces are a function of this area. Interestingly, the maximum loads on all the bridges are applied during the transient inundation phase of the superstructure, either when the bore slams the offshore face of the deck or as the bore propagates across the bridge impacting the interior girders and chambers. It is interesting to note that these maximum loads did not occur during the steady state phase, which occurs after the inundation of the top slab of the bridge.

- The two different bores and the bridge elevation affects the magnitudes of the loads. Examine the first case of Figure 3.6 (top graphs), for example, it shows that the bridge at a lower elevation witnesses a significant larger Fx. Moreover, for the first bore (top graphs) the minMz drops to 52% (of the respective value applied on a straight bride) at a 5o skew angle, while for the 2nd bore (bottom figures) it drops to 81%. Similarly, for the first bore the maxFx (horizontal) and maxFup (uplift) drop to 73% and 82% respectively while for the other bore they drop to 58% for both maxFx and maxFup, demonstrating clearly that the exact effect of the skew angle is dependent on the bore characteristics. However, overall the general trends in the loads as a function of the skew angle, present significant similarities, including large reductions of Fx and Fy (uplift), increases of Fz and nonlinear relationships for all the moments. All of these common trends in the loads (with skew angle) indicate the similarity in the underlying physics governing the induced effects. This is encouraging because it implies that a simplified methodology could be developed for a range of bores and bridge elevations.
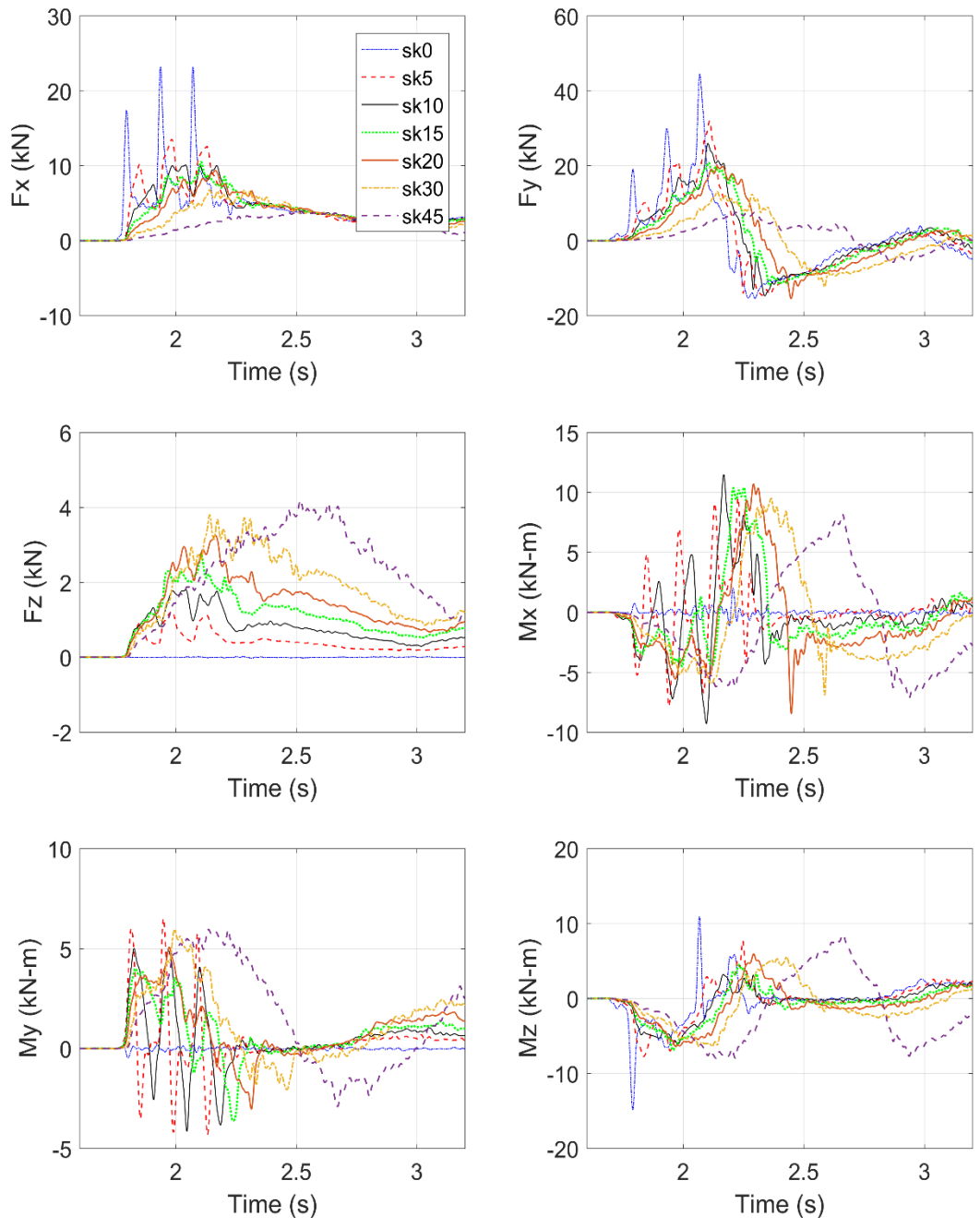
Figure 3.5: Load histories for different skewed bridges impacted by a bore

49
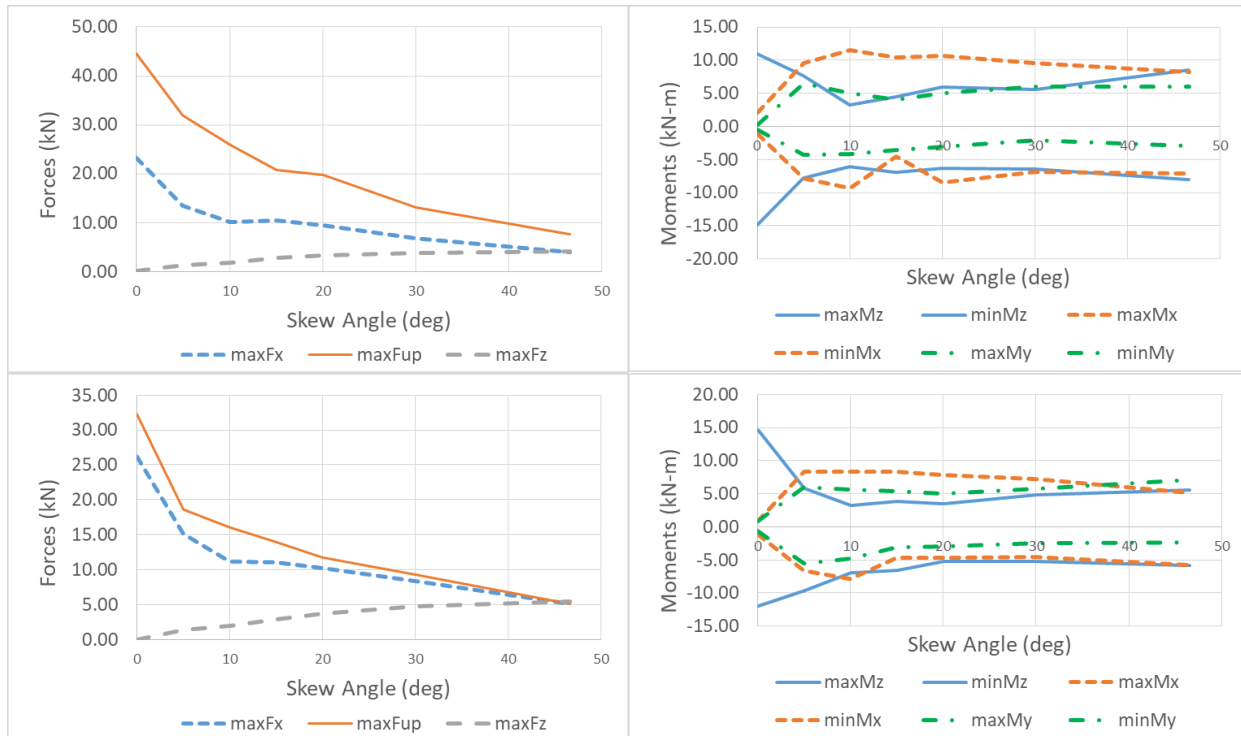
Figure 3.6: Maximum forces and moments applied on a skewed bridge for two different bores, as a function of the skew angle

In order to shed light on the reasons behind the observed behavior, the distribution of the bore-induced pressures on the skewed bridges during the tsunami inundation was investigated, and Figure 3.7 shows selected snapshots of these pressures for a 20° skew angle. The snapshots demonstrate clearly the generation of large localized pressures during the inundation of the bridge. These large pressures change location with time, starting with the acute corner of the offshore girder (closest part of the bridge to the ocean) and then gradually moving towards the obtuse corner of the same girder. These large pressures seem to occur at the instant that the bore impacts the particular location. The shifting of the location of the impulsive pressures from one end to the other end is the reason for the significant fluctuations in the Mx and My moments. Moreover, the complexity of this phenomenon increases by the fact that when the bore reaches the obtuse (left) corner of the offshore girder, at the same time (or a few centiseconds later) the bore reaches the acute (right) corner of the following interior girder. The applied pressures on the former location tends to generate an Mx and My in a specific direction, while the pressures on the latter location tend to apply moments in the opposite direction. This means that predicting the exact transient time-histories of Mx and My is rather challenging and could potentially be a function of (i) the skew angle, (ii) the distance between the girders, and (iii) the speed of the bore, all of which will determine how close in time the impulsive pressures on the obtuse corner of one girder (or chamber) will be to the ones of the acute corner of the following girder (or chamber).

Figure 3.8 presents the time-histories of the loads normalized with their maximum absolute value for the case of a long-duration bore and four selected skew angles. The left and right graphs present the loads that affect the demand in the horizontal direction (Fx, Fz and My) and vertical

50

direction (Fy, Mz, Mx) respectively. These graphs demonstrate that the maximum forces and moments do not necessarily occur simultaneously. This seems to be true for all the skew angles, and the increase of the angle seems to be affecting the time difference between the instants at which different loads are maximized. For example, while for a skew angle of 5° the Fx, Fy and My are maximized at instants very close to each other, for a 20° angle the My is maximized much earlier than Fx and Fy. This is a major finding both for advancing the fundamental knowledge of tsunami-induced effects on bridges, but also for design purposes because it indicates that it is not accurate to apply simultaneously all the maximum loads on a skewed bridge. Instead further investigation is required in order to identify the appropriate combination of forces and moments that will yield realistic demand in structural components.
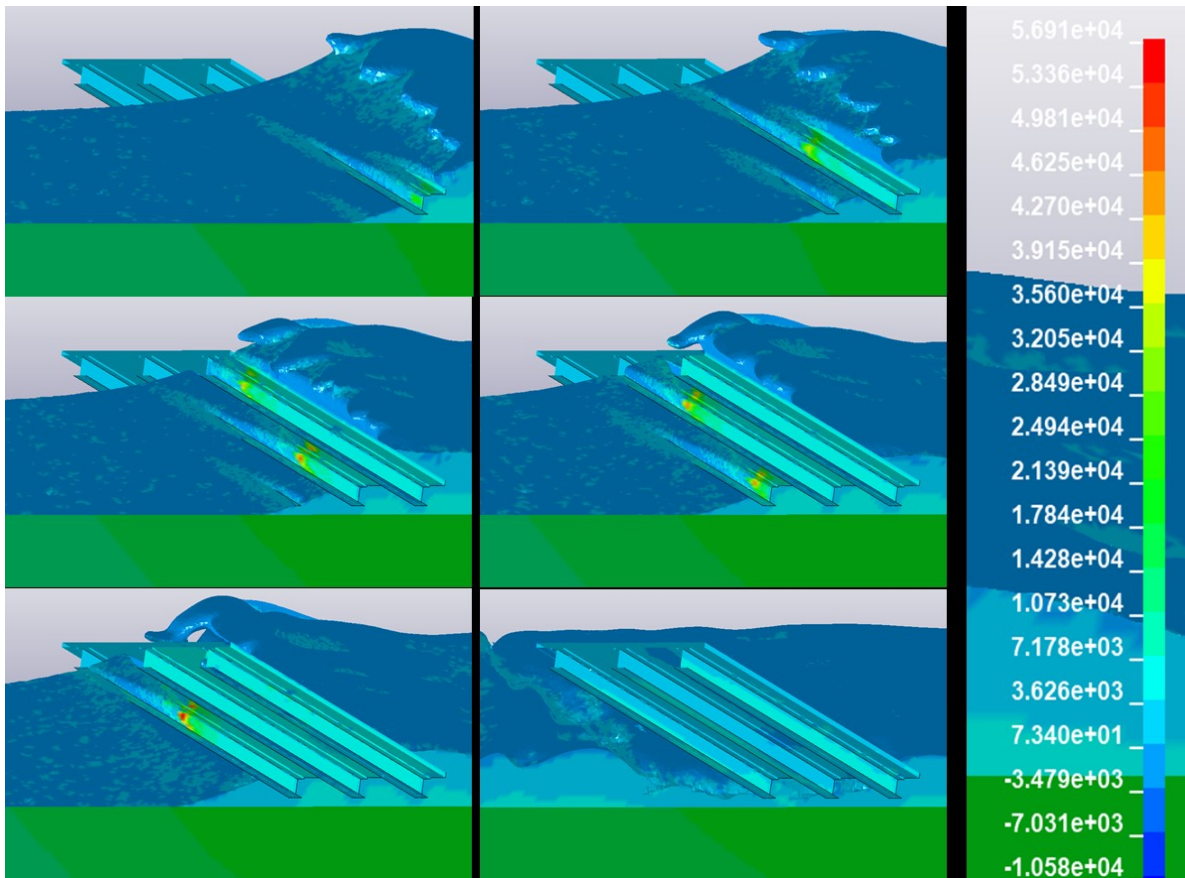
Figure 3.7: Snapshots of bore-induced pressures on a skewed bridge with a 20° skew angle
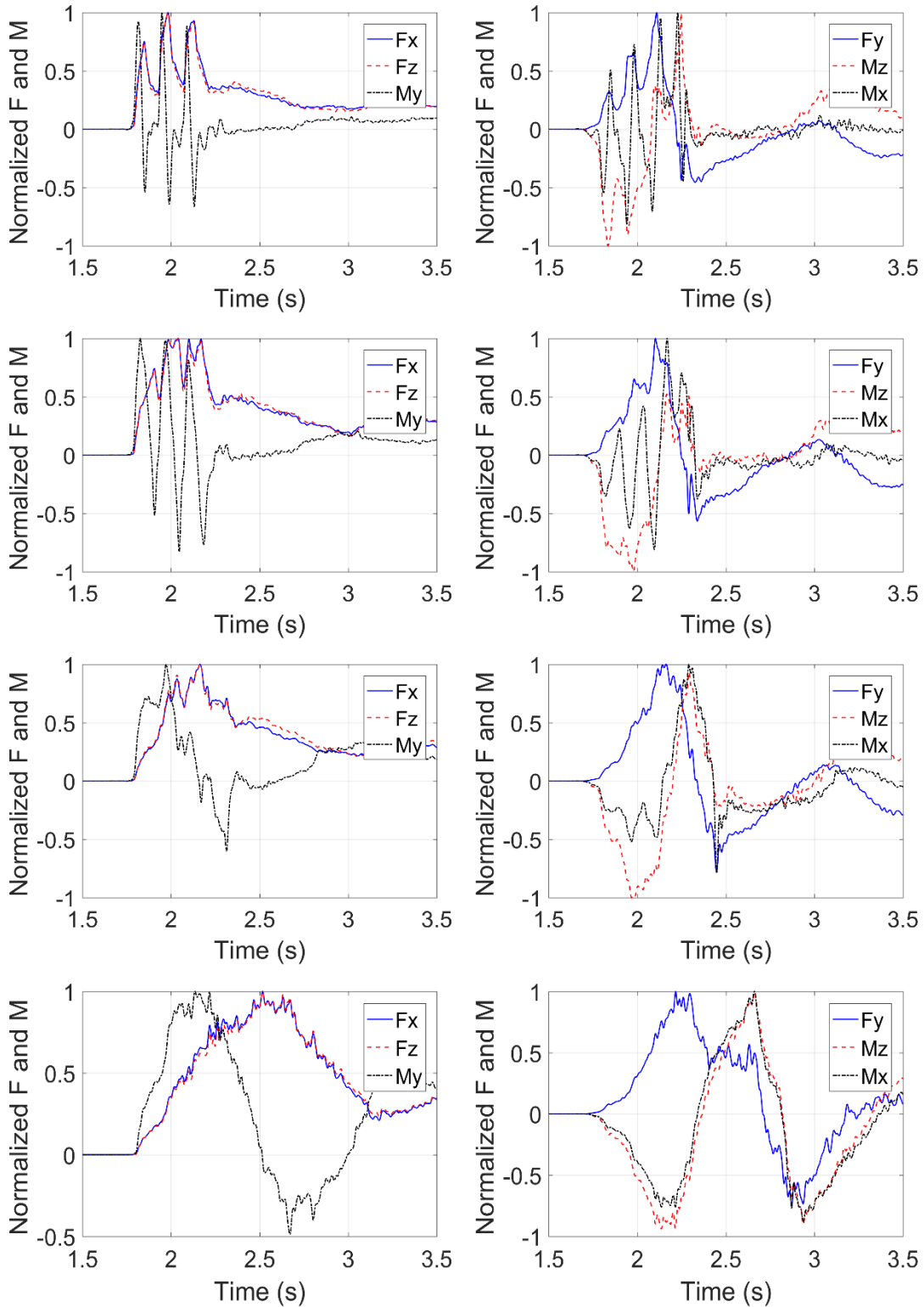
Figure 3.8: Normalized bore-induced load histories on an open-girder skewed bridge with skew angle θ=5º (top), θ=10º (2ⁿᵈ line), θ=20º (3ʳᵈ line) and θ=46.6º (bottom)

3.3 EFFECT OF BRIDGE WIDTH

Figures 3.9 and 3.10 show a comparison of the time histories of the forces and moments in all three directions for two skewed bridge models subjected to the same long-duration bore as in the previous sections. The smallest skew-angle (5º) and the largest one (46.6º) were intentionally selected in order to demonstrate a range of different trends and behaviors. Moreover, Figure 3.11 presents the change of the maximum loads as a function of the skew angle for both bridge widths. These graphs illustrate noticeable differences in the time-histories of the loads, with the wider bridge exhibiting two additional peaks for the small skew angle, which are generated by the application of the impulsive pressures on the two additional girders and chambers (which do not exist in the narrower bridge). Nonetheless, the width has a relatively small effect on the magnitudes of the majority of the loads, including Fx, Fz, Mx and My, for all the skewed angles.

The major difference is observed in the overturning (pitch) moment Mz, with the wider bridge witnessing significantly larger values. This is reasonable since the moment is calculated about the mid-width of the bridge (below the deck) and thus the wider bridge has a longer moment arm. Moreover, the wider bridge tends to exhibit larger uplift forces than the narrow bridge, and this increase is more obvious for the bridges with large skew angles (above 20º). This can be attributed to the fact that for small skew angles the maximum uplift force (and horizontal force) is dominated by the impulsive force peaks, which can generally get maximized when the tsunami impacts one of the first girders and chambers, at which point the additional two girders on the onshore side of the wider bridge have no effect. On the other hand, for larger skew angles the maximum uplift is achieved a little later when the wave already applies some pressures on the new girders. Overall though, the general trends of the maximum loads as function of the skew angle are quite similar, indicating the possibility for the development of a design method, which will be applicable to different bridge widths.
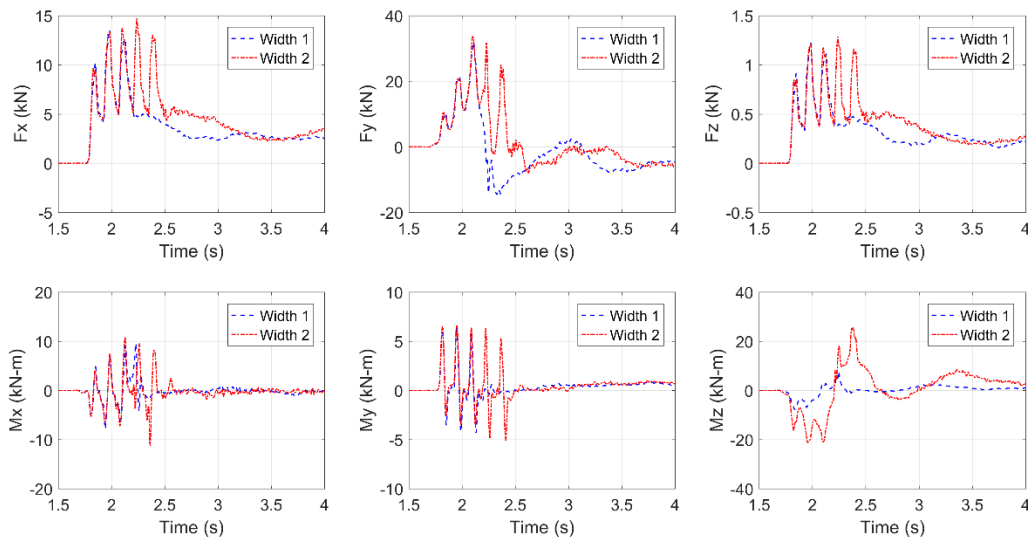
Figure 3.9: Bore-induced loads on two skewed bridges with different widths and a 5º skew angle

53
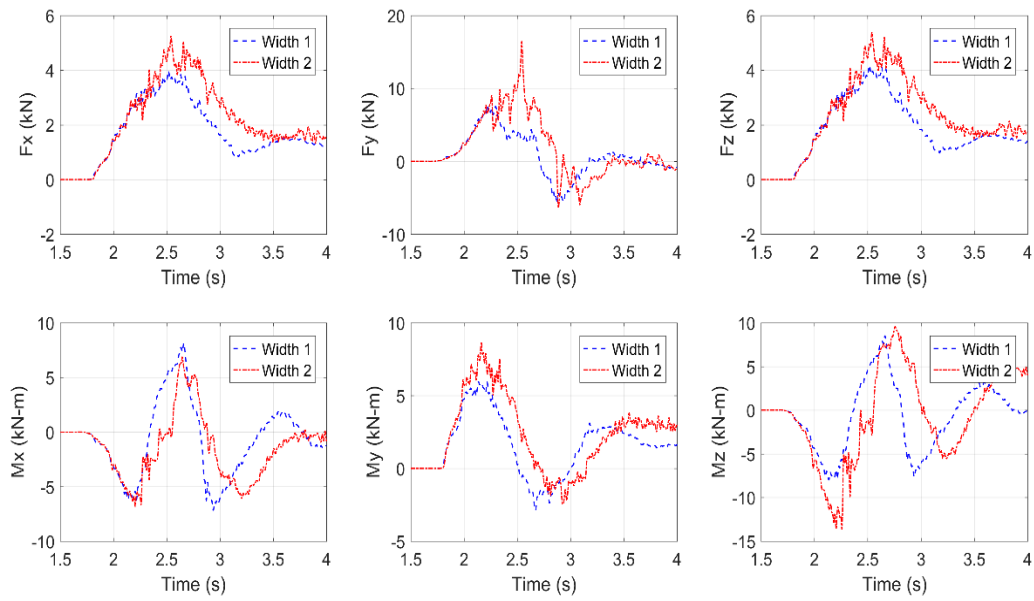
Figure 3.10: Bore-induced load histories on two skewed bridges with different widths and a 46.61⁰ skew angle
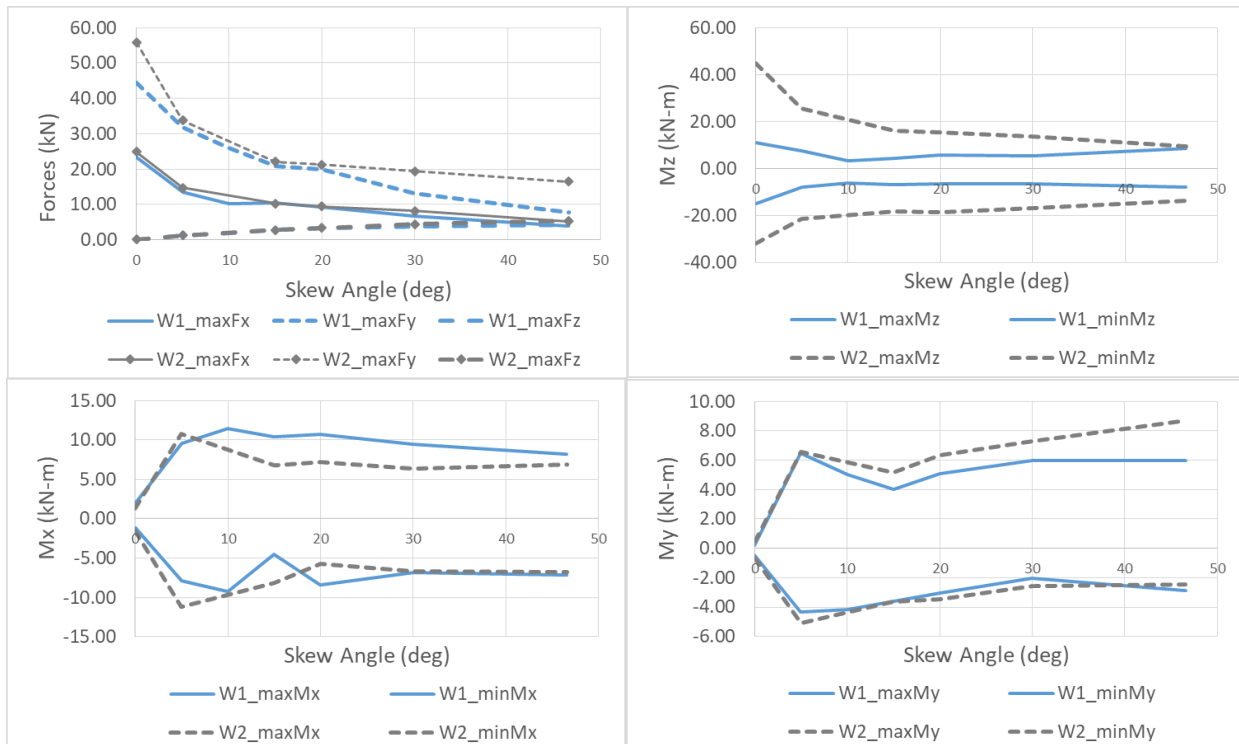
Figure 3.11: Maximum forces (top-left), and moments Mz (top-right), Mx (bottom-left) and My (bottom-right) for two bridges with different widths as a function of the skew angle

3.4   OPEN-GIRDER VS BOX-GIRDER BRIDGES

Figure 3.12 shows the time histories of the forces and moments in all three directions for seven differently skewed box-girder bridge models (θ from 0 to 45 degrees), which have all been subjected to a long-duration bore.
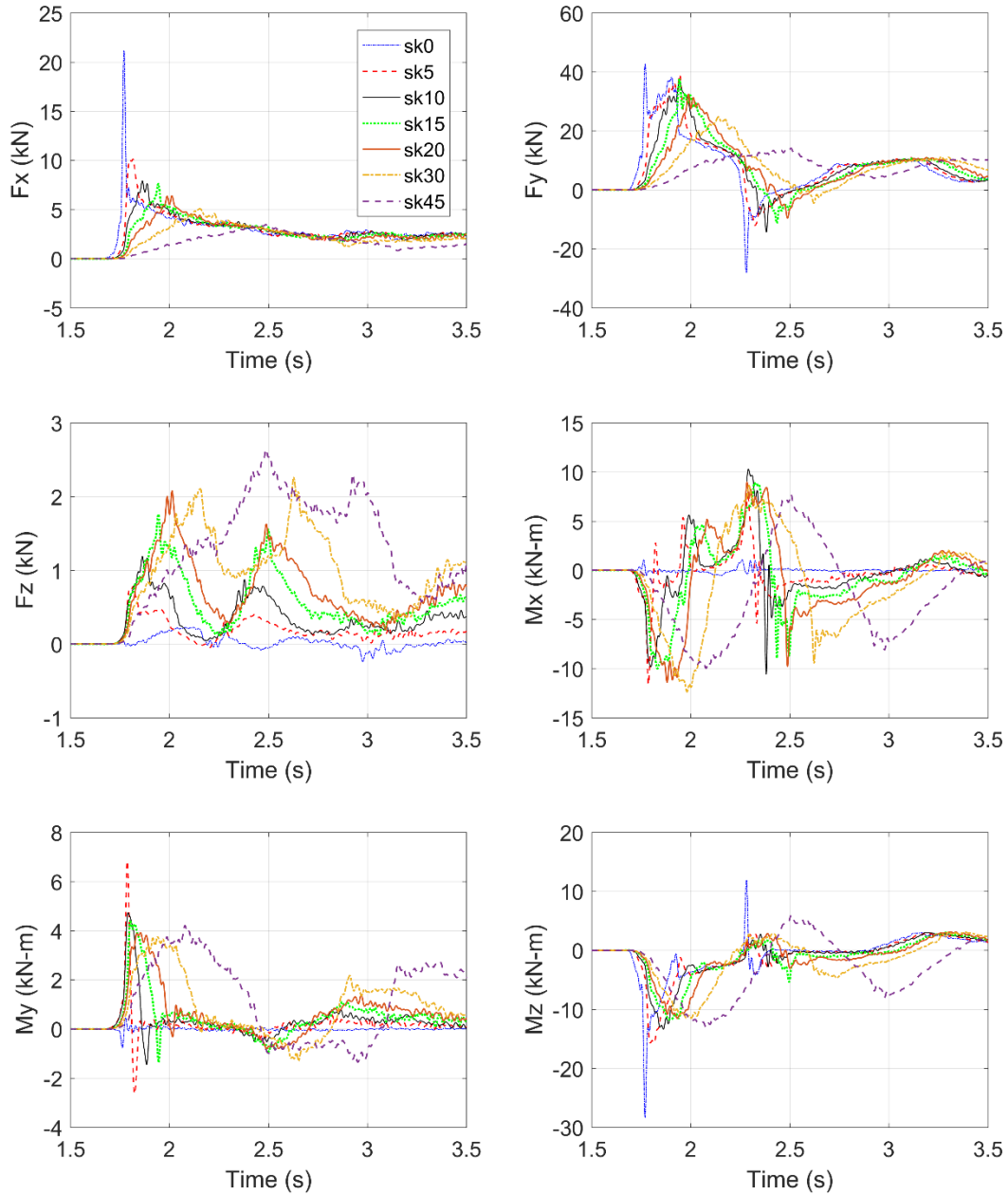
Figure 3.12: Bore-induced load histories on a box-girder bridge with different skew angles

Figure 3.13 presents the time-histories of the loads normalized with their maximum absolute value for the same bore, bridge type (box-girder) and three selected skew angles (θ=5º, 20º and θ=46.6º).
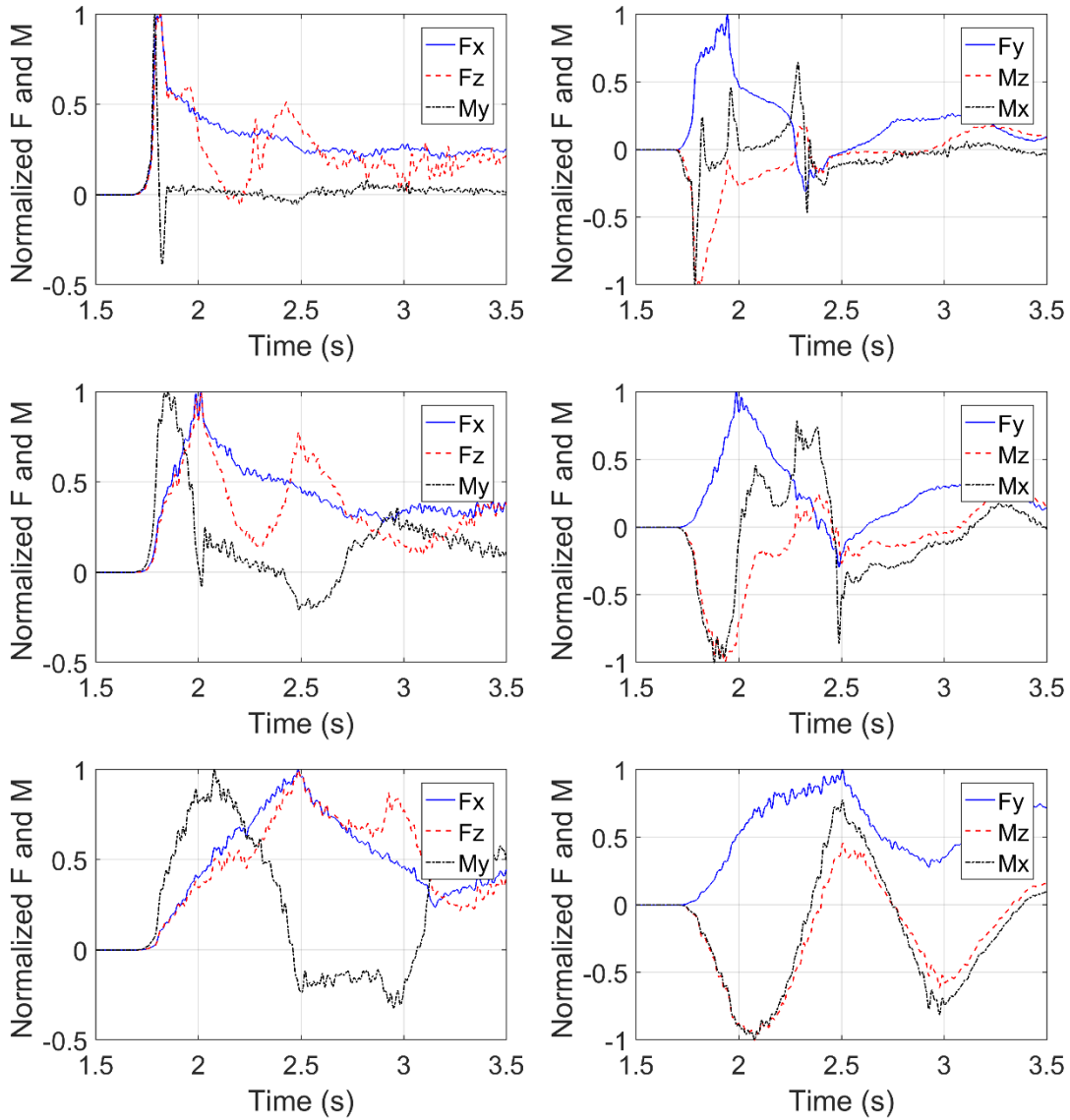
Figure 3.13: Normalized bore-induced load histories on a box-girder skewed bridge with θ=5º (top), θ=20º (center) and θ=46.6º (bottom)

Figures 3.12 and 3.13 demonstrate the following:

- The effect of the skew angle on the tsunami-induced loads on a box-girder bridge presents noticeable similarities with the case of open-girder bridges. This includes the significant reduction of Fx and Mz with the increase of the skew angle. It also includes the generation of Fz and its increase with the skew angle.

- Some of the major differences are observed in the moments Mz, Mx and My. While the increase of the skew angle causes a major reduction of the uplift force (similar to the one of Fx), this is not the case for box-girder bridges, which do not exhibit significant reductions for skew angles smaller or equal to 20o. Moreover, in contrast to open-girder bridges, box-girder bridges under this loading do not exhibit many

56

fluctuations in Mx and My since the tsunami does not impact the internal webs of the superstructure cells (as it did for the open-girder bridges). For both types of the bridges, though, the Fz, Mx and My tend to maximize during the inundation phase of the superstructure and before the water has covered the whole top slab of the deck and a steady-state condition is reached.

- Interestingly, in the case of box-girder bridges with a small skew angle (less or equal to 5o) the loads Fx, Fz and My are maximized at the same instant, when the tsunami slams on the offshore face of the superstructure. On the other hand, for larger skew angles the maximum values are do not occur simultaneously, with My being maximized before Fx and Fz, and the latter ones being equal to about 50% of their maximum values at the instant of maxMy. This means that the skew angle has a dual effect on the bore-induced horizontal demand on the structural components of the bridge. This is because the skew angle (i) reduces the maxFh, and (ii) offsets the instants at which My, Fx, and Fz occur reducing further the overall demand on the bridge members.

Figure 3.14 shows the maximum forces and moments for all the investigated skew angles and the two bridge types. Clearly, despite the fundamental differences of the load histories applied on an open-girder and a box-girder skewed bridge, the two bridge types exhibit similar decreasing tends for Fx, Fy, and Mz, and similar increases of Fz, Mx, and My, with the increase of the skew angle. However, three major differences are observed, including the maxFy, minMz and minMx, with the box-girder bridge having to withstand significantly larger values for the majority of the skew angles. In fact, as highlighted by the ratios of Figure 3-15, the skewed box-girder bridge has to sustain up to 89% larger uplift forces, 121% larger negative roll moments (minMx), and 118% larger negative pitch moments (minMz) than the respective open-girder bridge. It is noteworthy that the larger uplift demand on box-girder bridges relative to open-girder ones was experimentally observed in (Istrati, 2017) for straight bridges, however, this new numerical investigation reveals that the above is also true for skewed bridges. This means that designers should identify the exact skew angle and bridge type (box-girder or open-girder), in order determine the appropriate loads and load combinations.
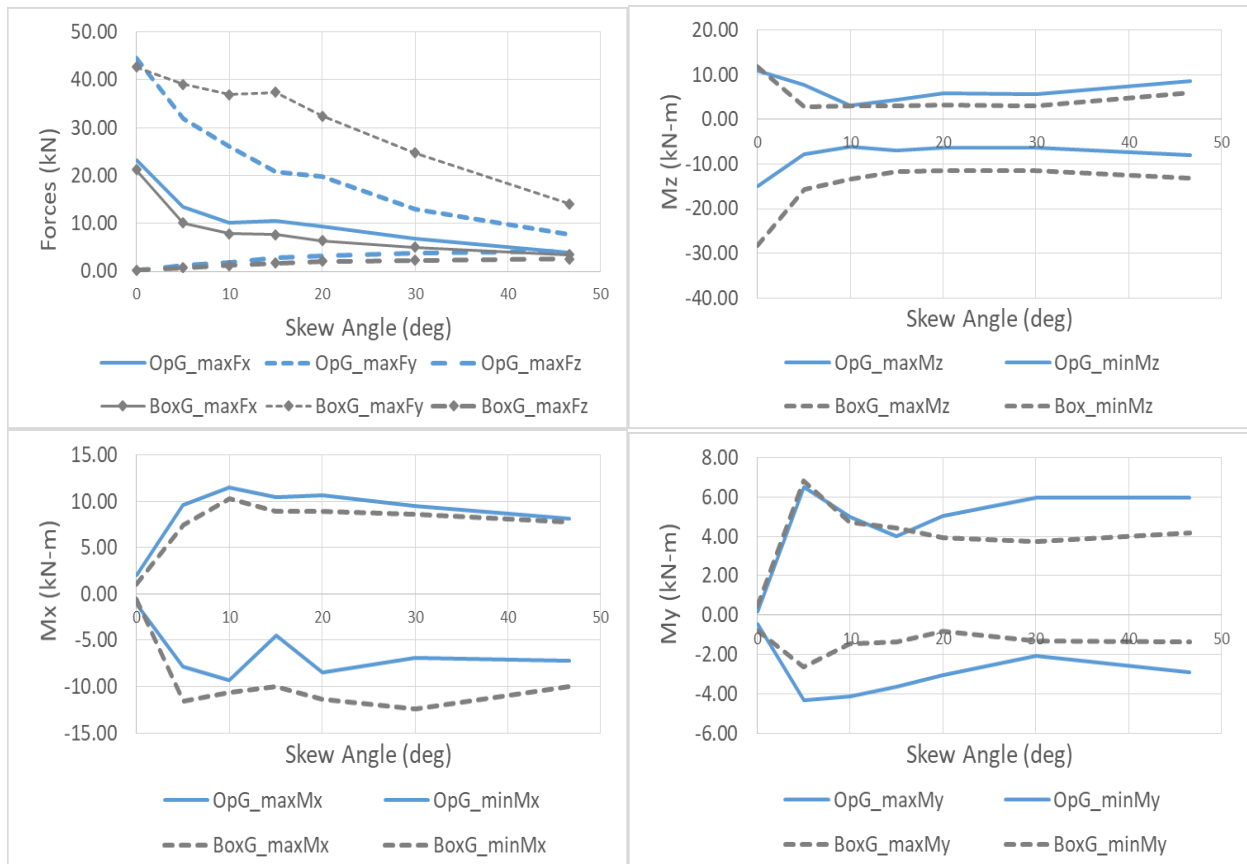
Figure 3.14: Maximum forces (top-left), and moments Mz (top-right), Mx (bottom-left) and My (bottom-right) for an open-girder and box-girder bridge as a function of the skew angle
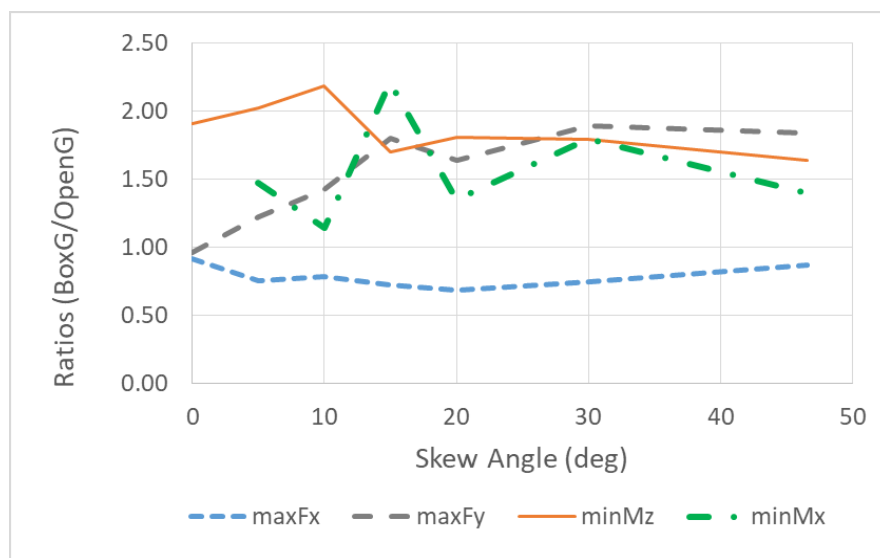
Figure 3.15: Ratios of maximum loads applied on the box-girder bridge relative to the open-girder one for a range of skew angles

3.5   SIMPLIFIED DESIGN METHODOLOGY

Given the similarities of the trends observed in the tsunami-induced loads on skewed bridges for different bores and bridge types, this section will investigate further the general trends and the possibility for developing a simplified design methodology. To that end, skew factors, which are ratios of the maximum loads applied on a skewed specimen relative to the respective load of a straight bridge, have been calculated and are presented in Figure 3.16. As observed in reconnaissance surveys following recent tsunamis (Kawashima, 2012), a large percentage of bridges failed due to the uplift (or combined uplift and rotation) of the deck. This in turn means that while the vertical load histories exhibit both uplift and downward peaks, the most severe situation is caused by the maximum uplift (maxFy), and not the downward one. Similarly, while the overturning/pitch moment (Mz) presents both negative and positive values, the most severe effects are expected to be applied by the maximum negative moment (minMz), which generates additional uplift in the offshore bearings and connections. For this reason Figure 3.16 presents the skew factors for maxFx, maxFy and minMz. Interestingly, for all of the investigated waves and bridge types investigated numerically herein, as well as the experimental data from the companion report (Istrati and Buckle, 2020], the three parameters of interest present similarly decreasing trends, with the minMz governed by more nonlinear trends (abrupt reduction for a small skew angle, and a small further reduction with the increase of the skew angle). Despite this difference it looks like a linear equation –termed "Design" – can provide an upper bound for all three parameters. However, for maxFx and maxFy this design equation has a value of 0.55 at θ=46.6º, while for the minMz it is 0.70. Also note that, the numerical results of the wave with H=0.65m exceeds the suggested design curves, however, this is considered acceptable because the specific wave is a simplified unbroken solitary wave, which does not necessarily introduce identical effects with a longer duration tsunami-like bore.

In addition to the three loads (Fx, Fy, Mz) that straight bridges have to withstand, this study showed that skewed bridges have to sustain a force normal to the direction of the tsunami propagation (Fz), as well as, roll (Mx) and yaw (My) moments. These maximum loads are plotted in Figure 3.17. Note that this figure shows only the bores, since it was observed that unbroken solitary waves with a finite wavelength present some differences in the applied moments on skewed bridges. Interestingly, although the previous section revealed a nonlinear increase of maxFz with the increase of the skew angle, when it is normalized by the respective maxFx applied on the same specimen, then the trend becomes near linear. In fact, the same linear equation seems to give a good prediction of maxFz for all the bores and bridge models, which is encouraging because it means that if maxFx is known then maxFz can be easily calculated via a generic linear equation. Figure 3.17 shows such a simplified design equation for maxFz, which is slightly conservative for skew angles smaller than 40deg and slightly unconservative for larger skew angles.

Moreover, another critical parameter for the design of skewed bridges is the My, which tends to increase the horizontal force in the components of each bent-cap and abutment. The time histories of this moment are complex and involve several peaks with fluctuations between positive and negative values, while the absolute values are dependent on the bore properties. However, when the maxMy is normalized by (maxFx*Ls) then significant similarities emerge in the overall trends, as shown in Figure 3.17. In fact, a bilinear non-dimensional equation with a value equal to 0.35 at 46.6º skew angle seems to bound the demand for all the cases. The good

correlation of all the cases with the maxFx and the skewed length Ls is reasonable because the gradual application of Fx along the length of each girder is the reason for the generation of My. Similarly, the normalization of the Mx with (maxFy*Ls) reveals some similarities in the trends, with the same bilinear equation bounding reasonably well both the maxMx and the minMx (maximum value in the negative direction). However, this non-dimensional equation is not identical to the one of the maxMy, and it gives smaller values which reach 0.22 at 46.6° skew angle.

The above figures demonstrate that if the maxFx and maxFy are known for a skewed bridge then the remaining parameters (maxFz, maxMy, maxMx, minMx) can be estimated using relatively simple (linear or bilinear) non-dimensional equations, which will be a function of the skew.
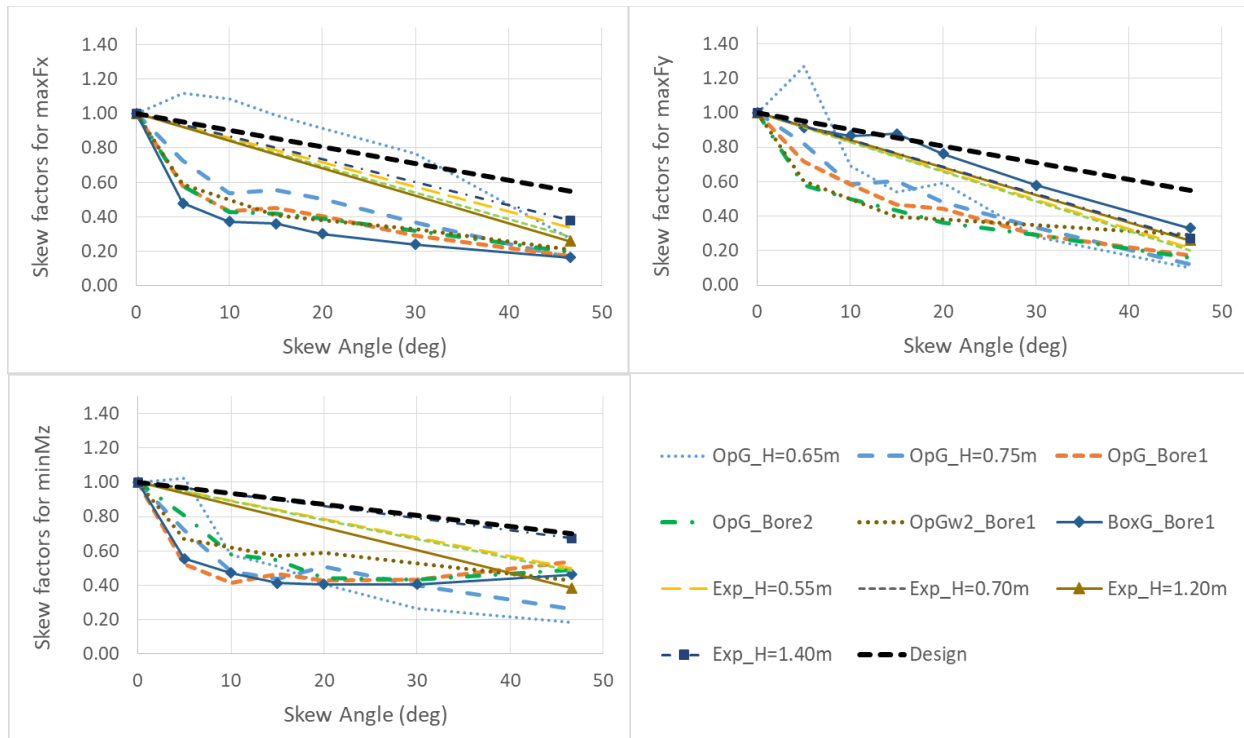
Figure 3.16: Skew factors for maxFx, maxFy and minMz, with suggested design curves as a function of the skew angle
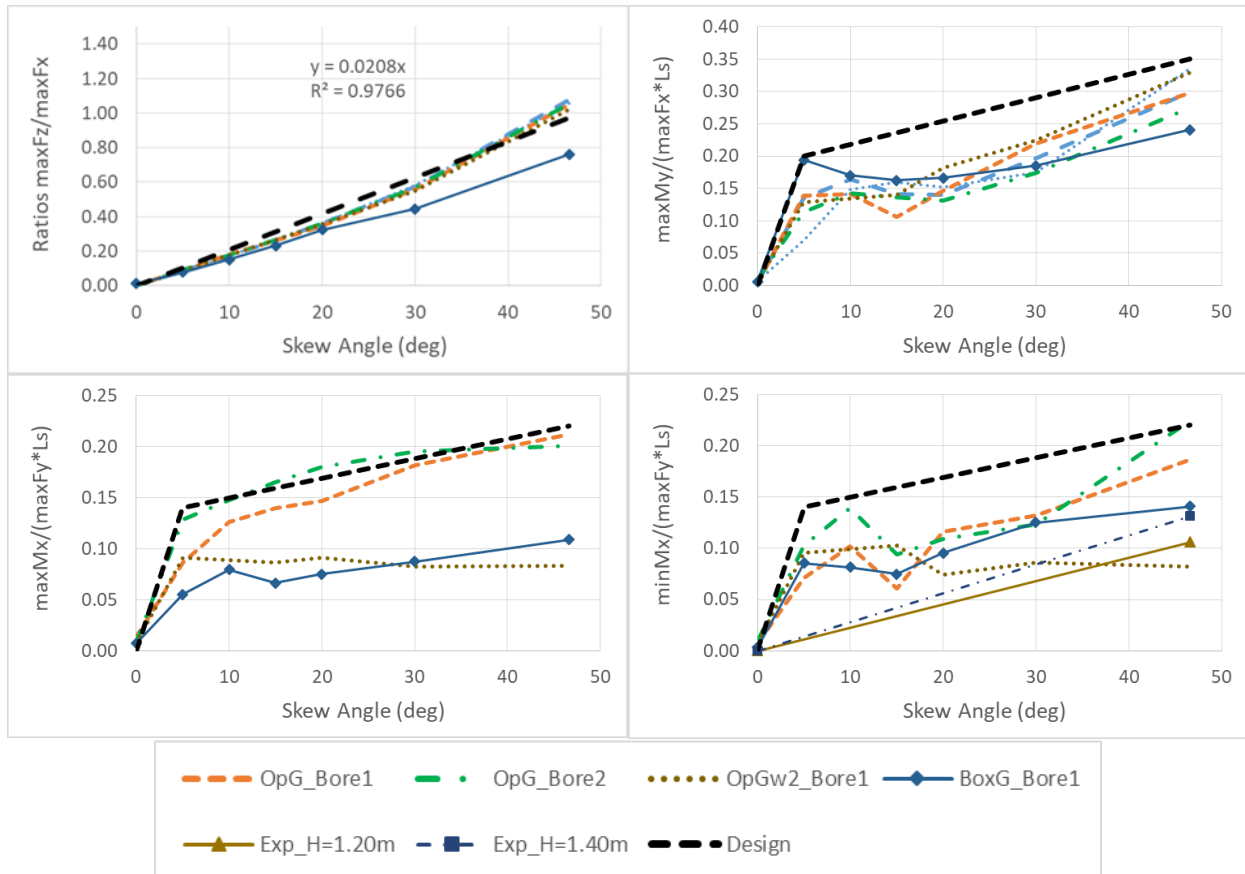
Figure 3.17: Non-dimensional maxFz, maxMy, maxMy and minMx with suggested design curves as a function of the skew angle

Having now the maximum loads applied in each direction, the next step is to determine whether all those maximum values occur at the same instant or if additional reduction coefficients have to be used for the development of realistic load combinations. To this end, the six loads (Fx, Fy, Fz, Mx, My, Mz) are normalized with their maximum absolute value (Mx was normalized with the maximum absolute value, while Mz is maximized with the absolute value of minMz) and the results are plotted in Figure 3.18 and 3.19 for several instants as a function of the skew angle. The experimental investigation conducted by the authors in a prior study (Istrati and Buckle, 2020) had revealed that the horizontal demand in the bent caps was maximized either at the instant of maxFx or maxMy or minMy, while the uplift demand in the bent caps and the individual connections could maximize at maxFy, minMz, minMx or maxMx. Therefore, these instants were selected as the critical ones in Figure 3.18, and the relative magnitudes of the loads at these instants were identified for each skew angle. Interestingly, although the maximum loads of the previous figure exhibited some consistency in the trends with the change of the skew angle, this does not seem to happen for the loads at the selected instants (based on the prior study). For example, at the instant of maxFy, where the deck is subjected to uplift, the Mx and Mz, which affect the uplift demand in the connections, can be either positive for some skew angles or negative for other angles.

61

The exact trends and load coefficients are dependent on the tsunami wave characteristics, bridge width, elevation and bridge type, verifying the complexity of (i) the three-dimensional interaction of the tsunami with a skewed bridge and (ii) the associated transient (temporally and spatially) loads. The non-consistent trends of the load coefficients with the skew angle makes it impossible to predict analytically their exact value, while the high dependence on the four aforementioned parameters means that specialized load combinations would be required for each bridge and wave case. To consider specialized load conditions in this way is impractical for design purposes. To facilitate the selection of the load combinations the authors have post-processed all the numerical results presented herein and have identified some combinations that could be critical for the bridge design. For this selection the range of possible coefficients were determined for each load and each instant, by identifying the minimum and maximum value witnessed by any skew angle. This means that these load combinations are not a function of the skew angle but should cover the range of skewed angles investigated herein.

Table 3.1, shows the load combinations that could potentially be critical for the horizontal tsunami-induced demand in bridge components, so the focus is on the proper combination of Fx, Fz and My. This is important because the horizontal force in structural components (e.g. bearings or shear keys), will depend not only on the total tsunami horizontal load Fx, but also on Fz and My. As noticed, these three loads may not be at max values at the same instant, which is the reason why we see coefficients smaller than one (or a negative value to represent the other direction). In addition to the coefficients of Fx, Fz and My, the table also shows the range of the coefficients of Fy, Mz and Mx (and the instant at which all of these occur), which could prove useful for the design of other structural components that have to withstand both horizontal and vertical loads. For the latter parameters, it is not possible to provide only one coefficient, because the coefficient changes inconsistently with the skew angle.

Similarly, Table 3.2 shows potentially critical load combinations for structural components that have to withstand the tsunami-induced vertical forces. Therefore, attention is paid to the proper combination of Fy, My and Mz, all of which contribute to the uplift that a bearing or a connection below the deck has to withstand. Moreover, the table also presents the range of Fx, Fz and My, which could be useful for the design of structural components that are located further from the deck (i.e. the bottom of the columns, the foundations etc). For such components, the uplift demand will be dependent also on the horizontal tsunami loads on the deck, since they will generate additional overturning moment (Mz) at the bottom of the bridge. Note that these load combinations are applicable to both open-girder bridges and box-girder ones; however, for the latter case the coefficients could be optimized further in the future, if additional numerical (or experimental) data were to be generated. Optimization would likely reduce some loads and could result in cost savings for design.
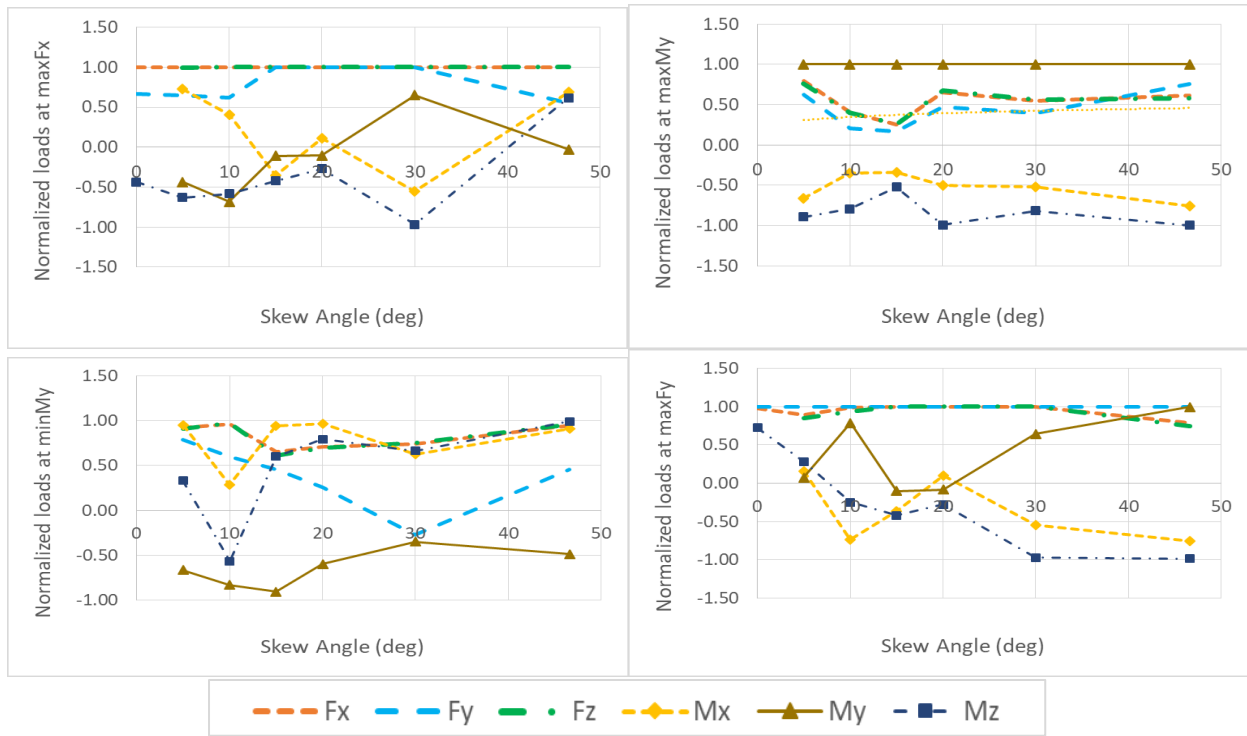
Figure 3.18: Bore-induced normalized loads on an open-girder bridge, at different critical instants (maxFx, maxMy, minMy, MaxFy) as a function of the skew angle
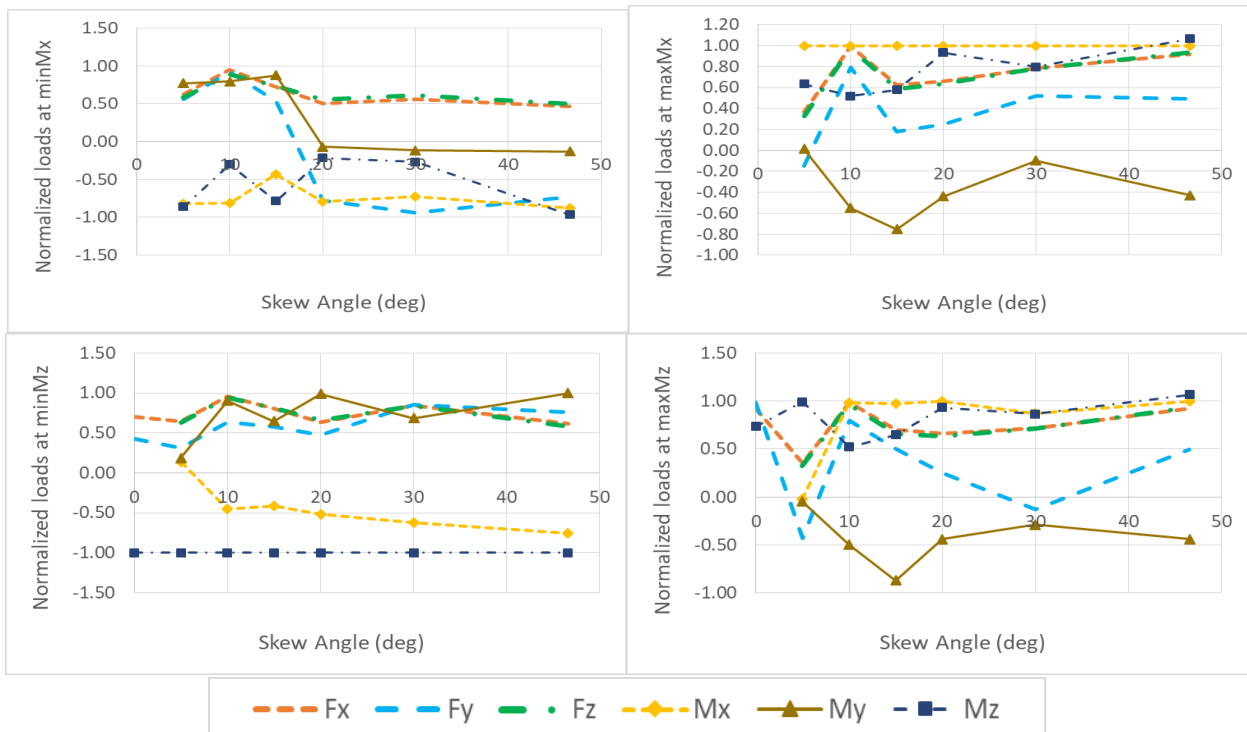
Figure 3.19: Bore-induced normalized loads on an open-girder bridge, at different critical instants (minMx, maxMx, minMz, maxMz) as a function of the skew angle

Table 3.1: Load Combinations – Part 1

Load Comb.	Coefficients						Comments
	Fx	**Fz**	**My**	**Fy**	**Mz**	**Mx**	
1	1.00	1.00	0.65	[0.45,1.00]	[-1.00,1.20]	[-0.91, 0.94]	At maxFx
2	0.85	0.81	1.00	[0.57,0.92]	[-1.00,0.48]	[-1.00,-0.34]	At maxMy
3	1.00	0.61	-0.93	[-0.82, 1.00]	[-0.96, 1.00]	[-0.85, 0.97]	At minMy
4	1.00	1.00	-0.93				

Table 3.2: Load Combinations – Part 2

Load Comb.	Coefficients						Comments
	Fy	**Mx**	**Mz**	**Fx**	**Fz**	**My**	
5	1.00	-0.76	-1.00	[0.52,1.00]	[0.59,1.00]	[-0.28,1.00]	At maxFy
6	1.00	0.77	-1.00				
7	0.92	-1.00	-1.00	[0.31, 0.97]	[0.33, 0.96]	[-0.13, 1.00]	At minMx
8	1.00	0.85	-1.00	[0.54, 1.00]	[0.50, 1.00]	[-0.79, 1.00]	At minMz
9	1.00	1.00	-0.74	[0.33, 1.00]	[0.15, 1.00]	[-0.88, 0.34]	At maxMx

In summary, the suggested design method is outlined in Table 3.3.

Table 3.3: Description of Simplified Design Methodology for Skewed Bridges

Step	Description	Equation	
1	Calculate Fx_0 and Fy_0 for a straight bridge using the equations for the maximum impulsive load		
2	Calculate the pitch moment Mz_0 using Method B for straight bridge described in [Istrati et al (2018)], which essentially applies the Fx_0 and Fy_0 at different bridge locations		
3	Calculate the skew factors $C_{1\theta}$ and $C_{2\theta}$, and the loads of skewed bridge Fx_θ, Fy_θ and Mz_θ, where θ=skew angle in degrees.	$C_{1\theta} = 1 - 0.010*\theta$ $C_{2\theta} = 1 - 0.0064*\theta$ $Fx_\theta = C_{1\theta}*Fx_0$ $Fy_\theta = C_{1\theta}*Fy_0$ $Mz_\theta = C_{2\theta}*Mz_0$	(eq. 3-1) (eq. 3-2) (eq. 3-3) (eq. 3-4) (eq. 3-5)
4	Calculate the skew factor $C_{3\theta}$ and the force Fz_θ	$C_{3\theta} = 0.0208*\theta$ $Fz_\theta = C_{3\theta}*Fx_\theta$	(eq. 3-6) (eq. 3-7)
5	Calculate the skew factor $C_{4\theta}$ and the yaw moment My_θ	$C_{4\theta} = 0.040*\theta$, for $\theta \leq 5°$ $C_{4\theta} = 0.20+0.0036*(\theta-5)$, for $5° < \theta \leq 46.6°$ $My_\theta = C_{4\theta}*Fx_\theta*Ls$	(eq. 3-8) (eq. 3-9) (eq. 3-10)
6	Calculate the skew factor $C_{5\theta}$ and the roll moment Mx_θ	$C_{5\theta} = 0.028*\theta$, for $\theta \leq 5°$ $C_{5\theta} = 0.14+0.002*(\theta-5)$, for $5° < \theta \leq 46.6°$ $My_\theta = C_{5\theta}*Fy_\theta*Ls$	(eq. 3-11) (eq. 3-12) (eq. 3-13)
7	Build a three-dimensional model of the skewed bridge model and run several different load combinations of Fx_θ, Fy_θ, Fz_θ, Mz_θ, My_θ and Mx_θ, as shown in Tables 3.1 and 3.2. Determine the max demand for each structural component (e.g. bearing, shear key, column, foundation etc), and design the respective components of the two bents/abutments of the skewed superstructure for the same tsunami load. Note: The equations are in SI units (θ in degrees, Forces in N, Moments in N-m)		

3.5.1 Limitations of simplified design methodology

This method is applicable to cases where the straight bridge witnesses impulsive loads (not for steady state conditions). For steady-state conditions, the Fx does not change with the skew angle, while for transient loads with longer-duration pulses (e.g. causes by a small velocity) the skew factors presented herein are not applicable, since they would over-predict the reduction with the skew angle.

The baseline open-girder models had cross-frames, which allows the air to escape. Additional investigation will be require in order to investigate if this method is directly applicable to open-girder bridge diaphragms. The diaphragms could potentially affect the fluid flow in the chambers and the associated since they will trap a certain amount of air and will interact directly with the tsunami, meaning the overall contacted area of the bridge will be larger.

The method is applicable to open-girder bridges with cross-frames and box-girder ones; however, it is not optimized for the latter case, since the absolute values of maxMy. maxMx and minMx tend to be smaller than what the methods predicts for skew angles larger than 5°, while the load coefficients in some load combinations could be smaller.

- The critical load cases have been identified based on the dynamic response of two large-scale experimental specimens – a straight bridge and a skewed one with 46.6deg- shown in Istrati and Buckle (2020), and the analytical results of the applied load histories on the seven skew angles discussed in this chapter. However, future studies should conduct fluid-structure interaction analyses or simplified dynamic analyses with equivalent applied tsunami pressures or loads in order to investigate if there exist other load combinations that could potentially govern the bridge design.

- At the end of the design phase (using the above simplified methodology) after the maximum demand in each structural component has been determined from the structural analyses, it is advised to design the components of the two ends/supports of a skewed bridge for the same load. This is because at this point there are too many uncertainties involved (e.g. in the load combinations) in order to ensure that the simplified method will result in the accurate distribution of the tsunami loads in all the bridge members. Moreover, designing the structural components of the two bent-caps of a skewed bridge for the same loads is expected to ease the design and avoid possible confusion during the construction process. While in reality, one bent-cap of a skewed bridge could attract larger forces than the other one, in order to accurately simulate the distribution, sophisticated FSI or sequential CFD and CSD would be required.

- Some components of the simplified method could be refined further if additional angles were investigated especially angles smaller than 10o

- The method is applicable for skew angles less than 46.6 deg.

4.0   EFFECT OF WAVE INCIDENT ANGLE

4.1   DESCRIPTION OF MODEL WITH 60° INCIDENT ANGLE

Given the significant role of 3D effects observed in the case of the tsunami impact on skewed bridges, it was of interest to investigate if similar effects could be generated in the case of straight bridges impacted by a wave incident angle different than 90º. To provide an insight into this topic the validated three dimensional model of an open-girder bridge with three I-girders presented in Chapter 1 was converted into a straight bridge impacted by a tsunami at a 60º angle. The selected tsunami was represented by one of the bores used in the previous chapter, which had a height of 0.70m and a velocity of 7.6m/s. To ensure that the hydrodynamic conditions were similar as in the straight and skewed models, the bore was kept exactly the same and the straight bridge was rotated as shown in Figure 4.1. This means that the computational domain had the same length and height (26m x 3m), however, the width of the flume was increased to 4.5m in order for the deck to match the length of the a skewed deck with a 30º skew angle (L_{deck}=3.995m).

One of the main differences of this model with the three-dimensional models presented in previous chapters was the modeling of the abutments at the two ends of the deck, because it was expected that when a wave hits a bridge at an angle different than 90º, some interaction of the hydrodynamic flow with the wing-walls could potentially take place. To make the models more realistic, a 10cm gap between the back-wall and the deck was simulated, assuming that the expansion joints had been damaged by the preceding earthquake shaking. Given the good agreement of the three-dimensional numerical model with the experimental data, when the bridge mesh-size was about 2-2.5cm in the x and y direction and 5cm in the z direction, the same mesh-size was used for the new model presented herein. In this model the mesh-size of the sides of the computation domain was 10cm, while the mesh-size in the remaining model was automatically generated by the solver using an unstructured mesh with size ranging between 2.5cm and 10cm. The total number of tetrahedral elements in the 3D model was 16.9million.
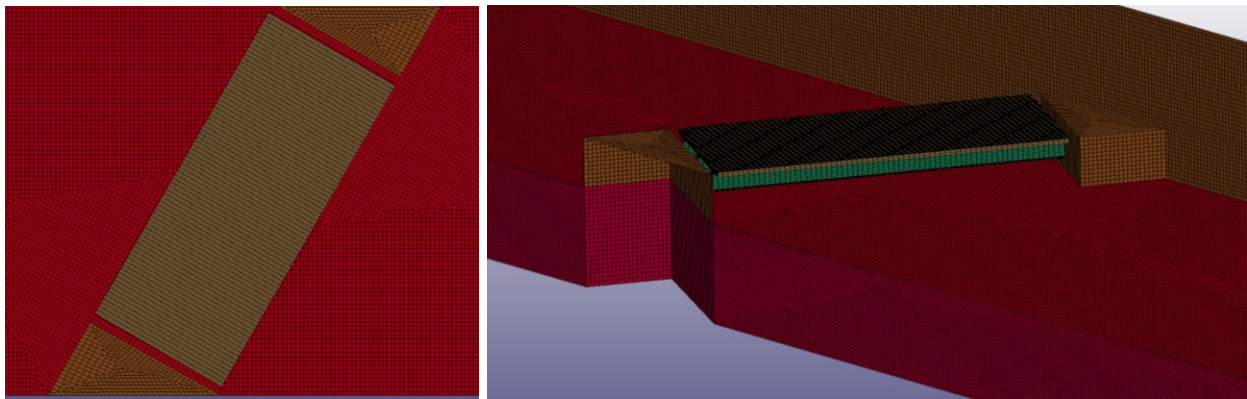
Figure 4.1: Three-dimensional numerical model of deck with abutments, including a plan view (left) and a 3D view (right)

4.2   FORCE AND MOMENT HISTORIES

Figure 4.2 shows the recorded time-histories of the loads on the aforementioned straight bridge, while Figure 4.3 presents the same time-histories but normalized with their maximum absolute value. In the latter figure, the left and right graphs present the loads that affect the demand in the horizontal direction (Fx, Fz and My) and vertical direction (Fy, Mz, Mx) respectively. These figures reveal that as was the case with the skewed bridges, straight bridges impacted by a tsunami at a 60° angle witness forces not only in the vertical direction (Fy) and in the direction of the flow (Fx), but also normal to that (Fz). Moreover, in addition to the pitch moment (Mz), yaw (My) and roll (Mx) are also applied on the bridge deck. In fact the results show that:

- **Fz:** The time-histories of this force exhibits trends similar to Fx, with some impulsive peaks on top of a long duration pulse in the direction of +z occurring at the beginning of the inundation. These peaks are followed by a significant steady-state component in the same direction.

- **My:** The yaw moment exhibits a positive pulse starting at the instant that the wave slams the offshore acute corner followed by an opposite moment generated as the wave propagates though the bridge and pressures are applied along the whole length of the girders. Once the bridge is permanently inundated then a steady-state positive moment (smaller than the transient moment) is generated. The yaw moment is expected to have a significant role for the horizontal demand (x and z directions) in structural components (e.g. abutment, shear key, columns etc), due to its large magnitude relative to the total tsunami induced horizontal load and the fact that it will affect the distribution of the applied loading to the two supports of each span.

- **Mx:** The roll moment is characterized by two small negative peaks, and a major longer duration pulse in between them. The reason for the generation of this moment is the gradual application of the vertical tsunami pressures starting from the offshore corner impacted first by the wave. This moment has a similar effect with the yaw moment by affecting the distribution of the forces in the structural components at the two ends of the span but this time in the vertical direction. This moment can potentially increase the cumulative uplift demand in the connections of the deck at one end of the bridge by up to 65% relative to the case where only Fy was applied on the bridge.

- The maximum forces and moments do not necessarily occur simultaneously. For example, the My is not maximized at the same instant with the Fx and Fz (but when they are about 50% of the max value), implying that the My might not necessarily affect the tsunami design of the bridge if that one is governed by another instant where the forces are maximized. This subsequently reveals the need for further investigation that will identify the critical combination of forces and moments for the design of the bridge.

- The Mx can have a governing effect on the maximum tsunami-induced uplift in structural components, since it is simultaneously maximized with the total uplift force

Fy and the pitch moment Mz. Therefore, such a critical combination should be further investigated and considered in the tsunami design of straight bridges.
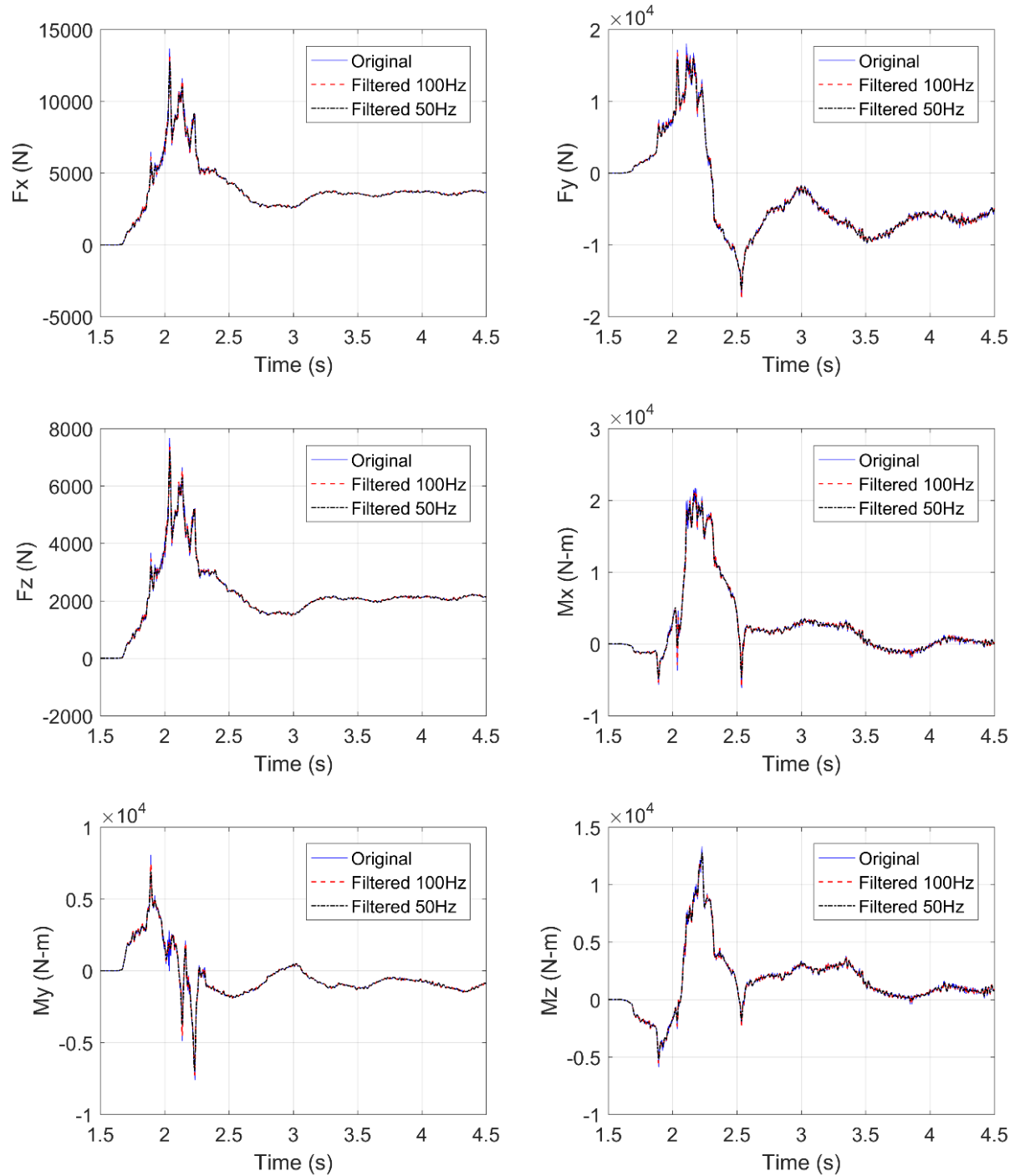
Figure 4.2: Applied loads on a straight bridge impacted by a tsunami-like bore with a 60° incident angle
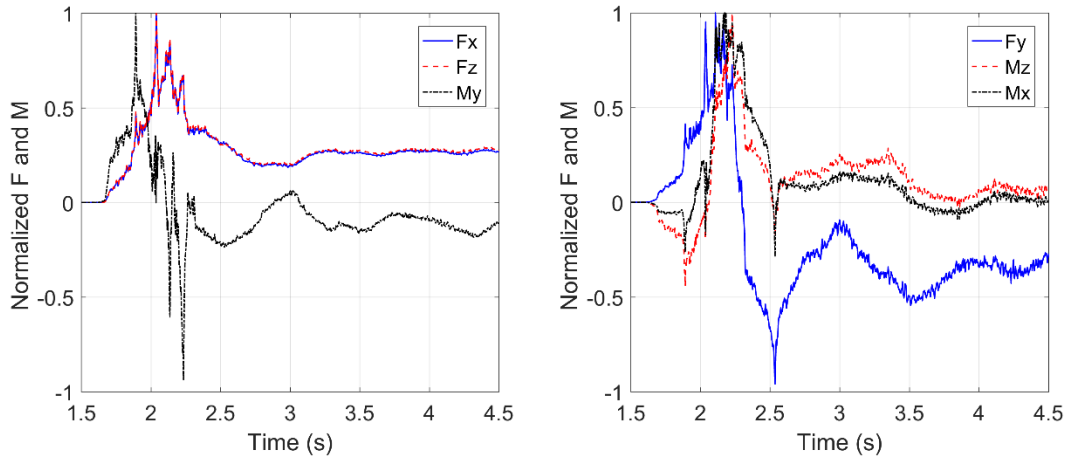
Figure 4.3: Normalized loads on a straight bridge impacted by a tsunami-like bore with a 60º incident angle

4.3 EFFECT OF INCIDENT ANGLE: 60° VS 90°

This section presents a preliminary comparison of a straight bridge impacted by a 90º wave incident angle with a 60º case. To save some time, the results of the existing straight bridge model of Chapter 3 was used as a baseline (90º). This means that the two models have the same in-plane area, however, the span length of the model in the latter incident angle is longer by about 15%, while its width is smaller by the same amount. This in turn means that the comparison shown in Figure 4.4 is not exactly accurate, however, it gives a preliminary insight into the effect of the incident angle. Future studies should be conducted with a more accurate representation of the specimens and several incident angles. For the time being, it is useful to note that:

- The normal tsunami impact on the bridge results in the larger lateral (Fx) and uplift forces, with the 60deg incident angle witnessing smaller loads due to the reduced impulsive peaks. These peaks are reduced probably due to the gradual application of the wave pressures on the straight bridge and the associated 3D effects. These effects, however, seem to be eliminated as the bridge becomes totally inundated with the two incident angles leading to the same steady state loading.

- The pitch moment Mz is also larger for the 90o incident angle, however, this is not true for all the peaks observed in the time-histories. In fact, while the normal impact applies a larger negative impulsive peak, generated when the tsunami hits the offshore girder and overhang (introducing uplift in the offshore connections), it is not true for the moment in the other direction. In the positive direction the 60o applies a larger magnitude with a significantly longer duration probably increased due to the interaction with the second abutment.

70
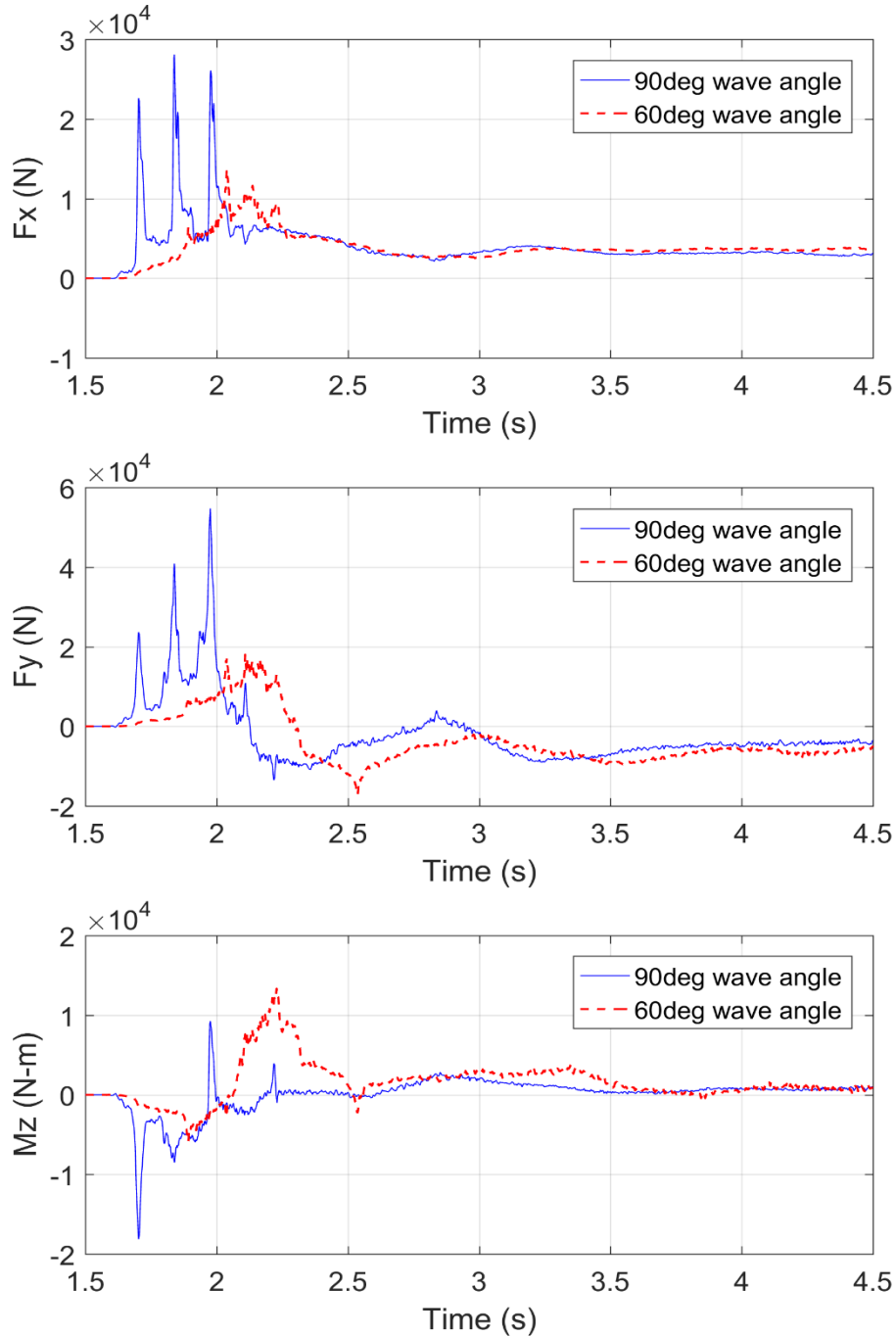
Figure 4.4: Fx, Fy and Mz histories for the straight bridge impacted by a tsunami bore at a 90º and 60º wave incident angle

4.4 WAVE INCIDENT ANGLE VS SKEW ANGLE

The last section of this chapter focuses on the comparison of a 30º skewed bridge with a straight bridge impacted by a tsunami at a 60º angle, both of which are shown in Figure 4.5. The motivation for this comparison is the fact that in both cases the relative angle between the deck and the wave is 30º. Given this similarity, it is of interest to see if the design methodology

71

developed for skewed bridges can be extended to straight bridges with incident angles different than 90°. It must be noted that despite this similarity, the two cases have a major difference. While in the case of the skewed bridge the abutments are aligned with the direction of the tsunami wave propagation (assuming it follows the river channel), in the case of the straight bridge with a 60° incident angle the abutments are also skewed relative to the direction of the tsunami wave propagation.
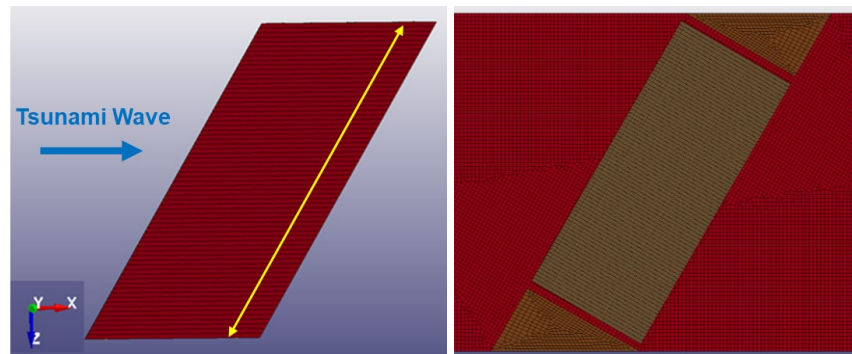
Figure 4.5: Plan view of the skewed bridge with a 30°skew angle (left) and the straight bridge with a 60° incident angle (right)

Figure 4.6 presents the loading histories applied on the two cases and reveals that:

- Overall the force and moment histories exhibit similar trends, indicating the generation of 3D effects both in the case of a skewed bridge and when the wave is skewed relative to a straight bridge. These 3D effects in turn generate significant forces in the z direction (Fz), as well as, roll and yaw moments, which do not exist when a tsunami impacts a straight bridge at a normal angle.

- Despite the similarities in the horizontal forces, the straight bridge with the incident angle witnesses larger and more impulsive peaks (up to twice as high). A possible reason for this is the channeling effect generated by the interaction of the first abutment with the incident wave when the tsunami reaches the bridge, which could modify the flow and increase the velocity at which it impacts the remaining length of the girders and slab.

- The channeling effect could also be the reason for the larger positive peaks of Mx, My and Mz. However, as shown in Figure 4.6 and 4.7, while the maximum peak of My seems to be occurring slightly before the tsunami reaches the second abutment, the Mx and Mz are maximized after the tsunami impacts this abutment. Consequently, this indicates that the local obstruction of the hydrodynamic flow caused by the second abutment could also contribute to the increased forces and moments, as well as, to the different steady-state conditions. The effects of the abutments on the fluid velocities can be observed in the snapshots of Fig. 4.7, with the main velocity increase occurring next to the offshore face of the first abutment and behind the second abutment.

The above results demonstrate that the design methodology developed for skew bridges is not necessarily applicable to straight bridges with wave incident angles different than 90 degrees, since it could significantly under-predict the horizontal forces and some of the moments applied on the bridge.
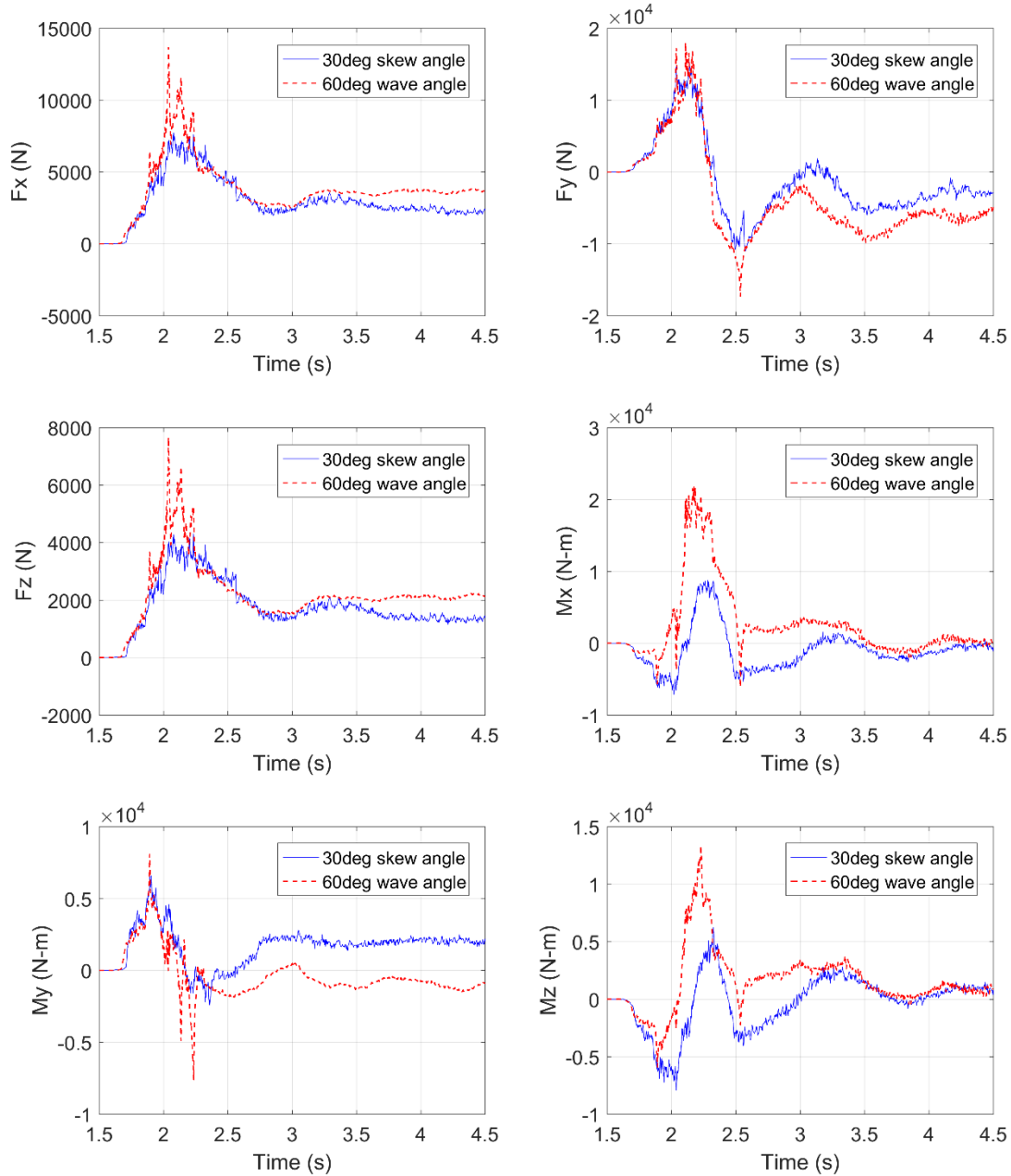
Figure 4.6: Tsunami-induced loads a skewed bridge with a 30° skew angle and a straight bridge with a 60° incident angle
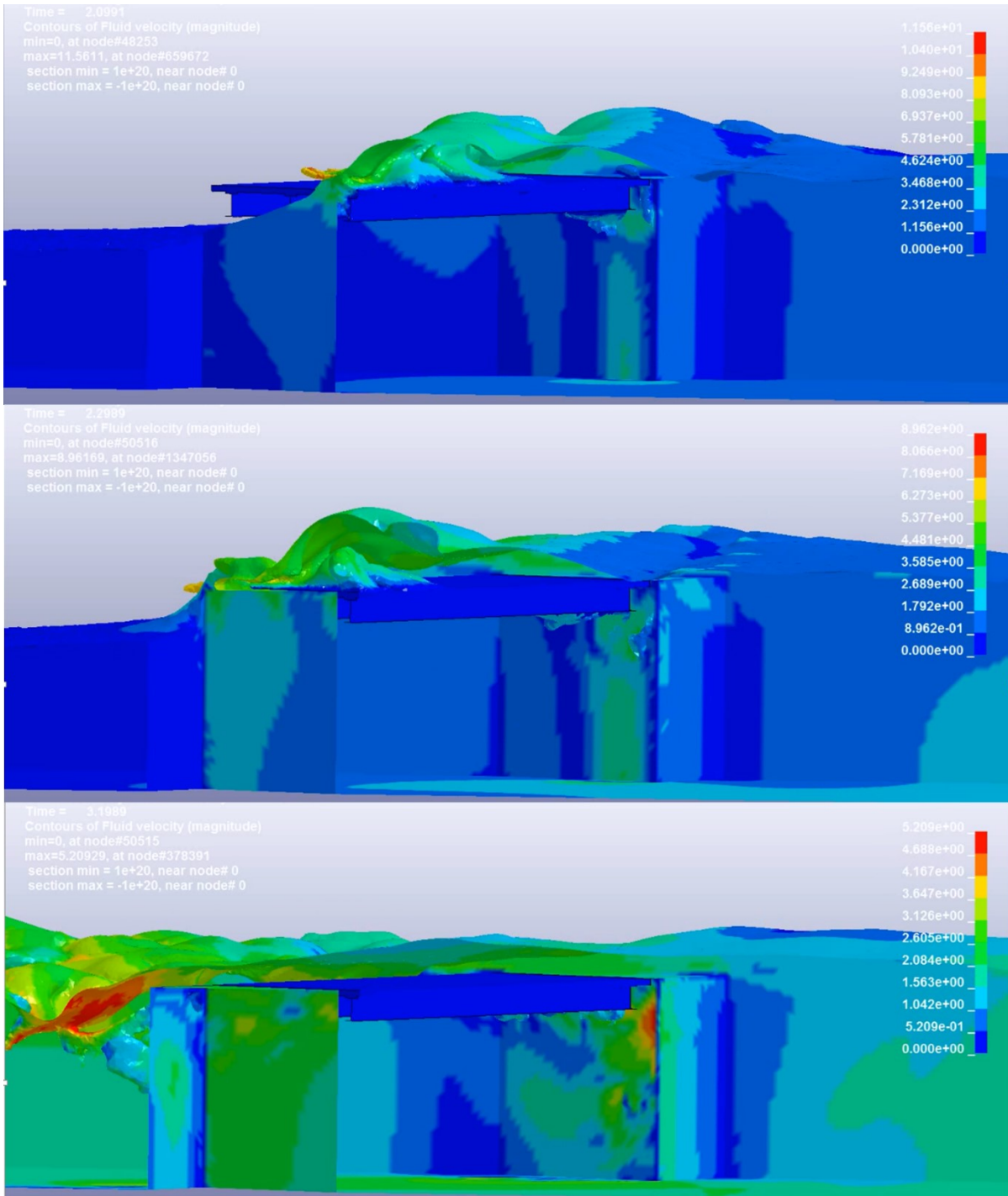
Figure 4.7: Snapshots of the fluid velocity field around a straight bridge impacted by a tsunami bore with a 60° incident angle

5.0   PERFORMANCE CRITERIA

5.1   INTRODUCTION

Performance-based seismic design for bridges is currently a major initiative for AASHTO. The recently completed NCHRP 12-106 project for the development of *Guidelines for Performance-Based Seismic Design* relates to the ground shaking hazard. It is very likely that AASHTO will wish to see the methodology extended to include the tsunami hazard. The first step in doing so is to define the levels of performance desired, and provide guidance to Owners on when each level of performance might be appropriate. This chapter describes how this might be done based on the findings of the 12-106 project, modified for the tsunami hazard. To begin, three performance levels are described:

Life Safety is the lowest level, in which the potential for bridge collapse is minimized during a tsunami but perhaps requiring replacement afterwards.

Operational is an intermediate level of performance in which the bridge is damaged but usable by emergency vehicles and reparable with or without restrictions on traffic flow. This performance level presents the greatest challenge in terms of converting the performance objective into required design parameters.

Fully Operational is the highest level of performance proposed herein, in which full use of the bridge is expected immediately following a tsunami. However, an inspection may be necessary to determine the condition of a bridge, its approaches post-event, and its adequacy for emergency and other kinds of traffic.

To implement this process the following steps need to be defined:

1. Tsunami hazard levels

2. Bridge operational categories, and

3. Performance criteria for each performance level.

Each step is described in following sections.

5.2   TSUNAMI LEVELS

Performance criteria for two levels of tsunami hazard are proposed in subsequent sections. The two levels include a Design Basis Tsunami (DBT) and a Maximum Considered Tsunami (MCT). These tsunamis are defined in Table 5.1.

Note the 75-year exposure period in Table 5.1 is consistent with the assumed life of a bridge adopted by AASHTO in various specifications for the seismic design of bridges due to ground shaking.

Table 5.1: Tsunami Levels

	Probability of Exceedance	Approx. Return Period
Design Basis Tsunami (DBT)	7 % probability of exceedance in 75 years	1,000 years
Maximum Considered Tsunami (MCT)	3 % probability of exceedance in 75 years	2,500 years

5.3 BRIDGE OPERATIONAL CATEGORIES

Performance criteria should be based on the owner's classification of the operational importance of a bridge. The three operational categories adopted herein are based on those given in the recently completed NCHRP 12-106 report: *AASHTO Guidelines for Performance-Based Seismic Design.* These three categories are 'critical', 'recovery' and 'ordinary', as described in Table 5.2.

Table 5.2: Bridge Operational Categories

Category	Description
Critical	Open to all traffic after inspection and clearance of debris following the DBT. Usable by emergency vehicles and for security/defense purposes after MCT.
Recovery	As a minimum, open to emergency vehicles and for security/defense purposes after inspection and clearance of debris following DBT. May be closed after the MCT, but no span is expected to collapse during this event.
Ordinary	May be closed following DBT and MCT, but no span is expected to collapse during these events.

5.4 PERFORMANCE CRITERIA BASED ON OPERATIONAL CATEGORY

It is convenient to quantify performance criteria using performance levels as is done in the previously mentioned NCHRP 12-106 Report, and the FHWA Seismic Retrofitting Manual. It will be seen in Table 53 that three Performance Levels are proposed and assigned according to Bridge Operational Category (Table 5.2) and Tsunami Level (Table 5.1). Expected performance at each Performance Level is given in Table 5.4.

Table 5.3: Assignment of Performance Levels Based on Operational Category

Tsunami Level	Bridge Operational Category		
	Critical	**Recovery**	**Ordinary**
DBT (1,000 yr)	Fully Operational, PL3	Operational, PL2	Life-safety, PL1
MCT (2,500 yr)	Operational, PL2	Life-safety, PL1	Life-safety, PL1

Table 5.4: Performance Levels and Associated Performance

Performance Levels		
PL1: Life-safety	**PL2: Operational**	**PL3: Fully Operational**
Significant damage is sustained during the DBT and MCT and service is significantly disrupted, but the potential for collapse is minimized. Closure is expected and the bridge may need to be replaced especially following the MCT.	Damage sustained is minimal and access for emergency vehicles is available after inspection and clearance of debris. Bridge should be reparable with or without restrictions on traffic flow.	No damage (or very minor damage that does not require immediate attention) is sustained and full service is available for all vehicles almost immediately after the DBT.
Significant damage includes permanent offsets and cracking. Plastic hinging in the columns is likely to be extensive. Offshore deck slab overhang is likely to have failed. In moderate-to-loose soil conditions severe foundation scour is expected that may lead to permanent vertical misalignment of substructure elements. Approach scour is likely to be extensive limiting access to the bridge. No connection failures between the superstructure and substructure (bearings, restrainers, shear keys) are expected during DBT and no girder unseating. Connection failures are to be expected during MCT, but not girder unseating. Undesirable failure modes such as shear failure in reinforced concrete are avoided.	*Minimal damage* includes minor inelastic response and narrow flexural cracking in concrete substructures due to minor plastic hinging. Offshore deck slab overhang is likely to have failed. Minor foundation and approach scour are expected but bridge serviceability and access are available under controlled conditions for emergency vehicles and security/defense purposes. No connection failures between the superstructure and substructure (bearings, restrainers, shear keys) are expected during the DBT and MCT, and consequently no girder unseating. Undesirable failure modes such as shear failure in reinforced concrete are avoided.	*Very minor* damage consists of minor cracking of concrete, possible incipient crushing or flaking of concrete cover. Minor rebar yield ($\mu<2$). Offshore deck slab overhang is likely to have survived. No significant foundation scour is expected but minor approach scour may occur. This should be quickly reparable and access restored for all vehicles almost immediately. No connection failures between the superstructure and substructure (bearings, restrainers, shear keys) are expected during the DBT and MCT, and consequently no girder unseating. Undesirable failure modes such as shear failure in reinforced concrete are avoided.

6.0   SUMMARY AND FUTURE WORK

6.1   SUMMARY, OBSERVATIONS AND CONCLUSIONS

This report has presented a numerical investigation of tsunami loads on coastal bridges, advancing the state-of-knowledge in the field and providing useful information for the tsunami design of bridges. A FEM-based incompressible hydrodynamic solver within LS-DYNA was utilized in order to conduct a range of computational fluid dynamic (CFD) simulations of different types of bridges. Both the two- and three-dimensional (3D) formulations of the CFD solver were used, and their accuracy was tested against small-scale experiments available in the literature and large-scale-experiments of straight and skew bridges conducted by the authors (Istrati, 2017; Istrati and Buckle, 2020). The numerical investigation focused on the simulation of a 1:5 scale bridge specimen and three existing bridges located in Oregon, including straight bridges with two different superstructure types (open-girder and box-girder). Utilizing the validated 3D computational model of an open-girder skewed bridge with a 46.6º skew angle tested in the prior hydrodynamic experiments, a parametric investigation was conducted in order to quantify the effect of skew angle. Seven different bridge models with skew angles equal to 0º, 5º, 10º, 15º, 20º, 30º and 46.6º respectively were investigated under the impact of solitary waves (unbroken and broken) and more-realistic tsunami-like bores.

The new numerical data together with prior experimental results were used in the development of a simplified methodology for the tsunami design of skewed bridges. Despite the complex transient 3D effects and loading histories associated with the tsunami inundation of skewed bridges, the newly developed method can be conveniently used by designers, since it requires as an input only the maximum Fx, Fv and Mz applied on a straight bridge with the same cross-section. This methodology can be used for the design of both open-girder bridges with cross-frames and box-girder ones. In addition to the simplified design method, the current study gives an insight into the capabilities and limitations of CFD simulations and demonstrates that:

- FEM-based CFD solvers with a level-set method and a Large Eddy Simulation turbulence mathematical model can achieve very good predictions of the free-surface and wave-induced loads on coastal structures, including slab-type, open-girder and box-girder bridges.

- Two-dimensional CFD models can provide an accurate estimate of the hydrodynamic loads on straight bridges impacted by a tsunami wave at a normal angle. However, more sophisticated three-dimensional models are necessary for the quantification of the tsunami-induced loads on skewed bridges or straight bridges impacted by oblique waves, which are common situations in the field.

- Truncated computational domains with equivalent waves at the inlet (e.g. solitary waves) can achieve a surprisingly good prediction of the maximum forces and moments applied on bridges, at a minimum computational cost. Due to their

combined efficiency and accuracy, such models are ideal for parametric investigations.

- The accurate prediction of the bore-induced pressures on specific locations of the offshore face of coastal structures requires an adequately small mesh-size, since impulsive pressures can be quite sensitive to the discretization. On the other hand, applied forces and moments, which are calculated from the integration of pressures, were seen to be less sensitive to the mesh-size. In fact, in the case of wave impact on a large skewed bridge specimen, numerical models with a medium mesh-size gave reasonable results while they reduced the required computational time in half relative to models with a fine mesh.

The current numerical simulations of tsunami impact on existing bridges together with the parametric investigation of skewed bridges led to interesting findings that advance the fundamental understanding of tsunami-induced loads on bridges. Some of the major findings are the following:

- While for small wave heights the maximum uplift force on a straight box-girder bridge occurs after the occurrence of the maximum horizontal force and overturning moment (OTM), for large waves this is not necessarily the case. In fact, for the Winchuck box-girder bridge the selected large unbroken solitary waves and tsunami-like bores applied horizontal and uplift forces, as well as an OTM, which were all maximized at the same instant. This in turn means that larger waves can have a much worse effect on critical infrastructure not only due to the larger magnitudes but also due to the simultaneous application of all the maximum loads. On the other hand, for the second box-girder bridge simulated herein the long-duration bore applied vertical force histories with two distinguishable uplift peaks, an impulsive one occurring when the wave slams the offshore face and overhang (slamming phase), and a longer-duration peak occurring during the propagation of the bore through the bridge when it applied uplift pressures on the soffit. Generally speaking, the maxFx and maximum OTM applied by tsunami-like bores tend to maximize at the same time during the slamming phase, however, the maxFup can occur either during the slamming phase or later and this depends on the actual box-girder geometry and bore characteristics (shape, height, velocity).

- Regarding open-girder bridges, they tend to witness applied vertical forces with several uplift peaks, two of which can have a governing effect. The first one occurs during the slamming phase (similarly to the box-girder) and the second one as the wave inundates some chambers (e.g. chamber 1). Although at the first instant the uplift pressures are applied only on the offshore overhang, which has an area much smaller than the area on which the pressures are applied at the second instant, the former can still govern the uplift demand for some bridges due to fact that after the initial slamming of the wave on the offshore girder fluid particles are redirected and move upwards with large vertical velocities slamming violently in to the overhang. After this initial impact, the hydrodynamic flow changes and the wave hits the first chamber with a smaller vertical velocity. This reveals the major role that the overhang plays when a bridge is subjected to extreme hydrodynamic loading and implies that

80

removing or modifying the overhang could potentially reduce the uplift demand both in box-girder and open-girder bridges.

- In contrast to straight bridges, skewed bridges seem to be subject to smaller transient lateral (Fx) and uplift (Fy) forces, and overturning moments (Mz), which have a longer duration. In fact, as the skew angles increases the magnitude of the impulsive peaks of Fx, Fy and Mz decrease and the duration of the hydrodynamic load applied during the inundation phase increases. Notably, though this longer duration transient pulse (e.g. 1.0-2.5s depending on bridge size and skew angle) is still larger than the following steady-state load, demonstrating that the bridge inundation phase is the critical one for the design of the superstructure.

- While the existence of a skew angle has a positive effect on Fx, Fy and Mz by reducing their magnitudes, the non-symmetric geometry of a skewed bridge (relative to the direction of the wave propagation) leads to a gradual application of the loads along the bridge length that generates forces and moments in the other directions. In fact, a skewed bridge is also subjected to a force normal to the direction of the tsunami propagation (Fz), as well as, roll (Mx) and yaw (My) moments. The Fz and My can have a detrimental effect on the bridge performance because they generate out-of plane horizontal loads that could result in the unseating of the deck. Moreover, the yaw moment (My) has a significant effect on the Fx force that each bent-cap or abutment has to withstand, by increasing it up to 46%. Similarly, the roll moment (Mx) results in the unequal distribution of the uplift force to the two ends of a skewed deck, overloading the structural components at one end (bent-cap, abutment, foundations) by about 37%.

- For open-girder skewed bridges the Fz force follow trends similar to Fx, while Mx and My have similar trends to each other, exhibiting fluctuations from positive to negative as the tsunami impacts first one end of the deck (the acute corner of the offshore girder) and then the other (the obtuse corner of the offshore girder). The fluctuations of the latter moments are reduced with the skew angle and eventually eliminated for skew angles equal to or larger than 20o. On the other hand, box-girder bridges do not exhibit so many fluctuations in Mx and My since the tsunami does not impact the internal webs of the superstructure cells. For both types of the bridges, though, the Fz, Mx and My tend to maximize during the inundation phase of the superstructure and before the water has covered the whole top slab of the deck and a steady-state condition is reached.

- While the width of a skewed bridge affects the time-histories of the applied tsunami loads, it tends to have a relatively small effect on the majority of the loads. The main exception is the overturning (pitch) moment Mz (since the moment arm changes), and the maximum uplift force Fup, both of which tend to increase in the case of a wider bridge. Nonetheless, when it comes to the change of the magnitude of the loads as a function of the skew angle the two bridges with different widths exhibit similar trends.

- Despite the fundamental differences of the load histories applied to an open-girder and a box-girder skewed bridge, the two bridge types have similar sets of skew factors for Fx, Fy, and Mz, and similar changes to the maximum loads Fz, Mx, and My, as a function of the skew angle. This indicates that the simplified design methodology developed herein could be used for both bridge types.

Last but not least, the comparison of bore impact on a straight bridge at a normal angle relative to the bridge span, with a case where the incident angle was 60°, revealed the generation of significant 3D effects in the latter case. These 3D effects resulted in the reduction of the impulsive peaks and the overall magnitudes of the forces Fx and Fy and overturning moment Mz, while they had practically no effect on the steady-state loads leading to identical hydraulic conditions after the deck was totally inundated. Moreover, these 3D effects generated in turn a force normal to the direction of the tsunami propagation (Fz), as well as, roll (Mx) and yaw (My) moments, as in the case of skewed bridges. However, a follow-up comparison of (a) a wave impacting a straight bridge at 60^0 angle with (b) a skewed bridge with a 30° skew angle, both of which lead to the same obliqueness of the wave relative to the bridge, demonstrated that the two cases are not identical. In fact, it was revealed that:

- While the tsunami-induced loads exhibit overall similar trends for the two cases, the oblique wave attack on a straight bridge witnesses more impulsive peaks and larger magnitudes in Fx (up to twice as high), Fy, Fz and My. A possible reason for this is the channeling effect generated by the interaction of the first abutment with the incident wave when the tsunami reaches the bridge, which could modify the flow and increase the velocity at which it impacts the remaining length of the girders and slab.

- The oblique tsunami attack also witnesses larger positive peaks of Mx and Mz, which can be attributed to the local obstruction of the hydrodynamic flow caused by the second abutment and the channeling effect.

Overall it is concluded that the interaction of the oblique tsunami flow with the two abutments of a straight bridge leads to larger transient loads and different steady-state conditions, relative to a skewed bridge with a similar angle between the wave and the bridge superstructure. This demonstrates that the design methodology developed for skewed bridges is not necessarily applicable to straight bridges with wave incident angles other than 90°, since it could significantly under-predict the horizontal forces and some of the moments applied to the bridge.

6.2   FUTURE WORK

The present numerical study, together with the companion experimental investigation, have advanced the understanding of the tsunami inundation mechanism of coastal bridges and associated loads. They have also enabled the development of simplified methodologies for use in the tsunami design of open-girder and box-girder bridges with straight or skewed configurations. Nonetheless, there are still several topics that require further investigation, as described below:

1. The design methodology for skewed bridges presented herein was developed based on a limited number of wave types and heights, water depths and bridge geometries. Future studies could refine the simplified methodology by investigating a larger range

82

of wave characteristics and bridge dimensions, and optimize both the empirical equations that predict the maximum loads, as well as, the load cases that combine the maximum loads in order to predict the most critical case for the design.

2. A more extensive study involving several wave incident angles should be conducted in order to decipher and quantify the effect of this parameter. The similarities observed between the oblique tsunami attack on a straight bridge and the loads on a skewed bridge, indicate that the results from a future parametric investigation on the incident angle could be used for modifying and expanding the tsunami design methodology for skewed bridges developed herein.

3. The focus of this study was on the applied loads on bridge superstructures because (a) the most common failure mode in past tsunamis has been the failure of the bearings and connections between super and sub-structures, and (b) there was very limited information available regarding tsunami loading on bridge decks for which developing simplified design equations is a challenge due to complex geometry and associated sensitivities in the numerical simulations. Future studies should investigate complete bridge systems where all the structural components are simulated, including not just the superstructure, but also bent caps and columns (bents). In addition, the oblique impact of a tsunami bore on a pier wall could be quite significant and significantly affect the hydrodynamic flow, which would then influence not only the transient but also the steady-state loading on the superstructure.

4. The 3D CFD analyses focused on a single span bridge in order to reduce the computational effort. Future studies should look at multi-span bridges and the influence of abutments. This is true both for straight as well as skewed bridges.

5. Additional studies are also required in order to understand the nonlinear wave-air interaction below the deck of open-girder bridges, especially in the presence of 3D effects generated by an oblique attack on a straight bridge or the tsunami impact on a skewed bridge with diaphragms. Although, several studies have investigated the importance of air-entrapment and wave-air interaction for straight bridges impacted by periodic or solitary waves (McPherson, 2008; Cuomo et al. 2009) and bores (Istrati and Buckle, 2019), there exists extremely limited information for skewed bridges or cases of oblique impact on straight bridges.

6. As noted above, this study focused on a CFD investigation of coastal bridges, but in a companion experimental study conducted by the authors (Istrati, 2017; Istrati and Buckle, 2020)] it is shown that structural dynamics and fluid-structure interaction effects can play a major role in the demand sustained by connections and structural components. This means that the findings of this study might not be applicable to bridges with significant flexibility, such as a seismically-isolated bridge, and future studies should examine the role of flexibility on the design methodology developed herein.

7. The generation of impulsive loads was observed both in the current numerical results and past experiments, for some of the tsunami bores. However, the experimental data

revealed also a significant aleatory variability in the impulsive tsunami load, which can be attributed to the chaotic wave breaking process of plunging waves. This chaotic process translates into a large variability in both the amplitude and the duration of the impulsive load. Therefore, future studies should examine the probability distribution of the impulsive load and develop probabilistic equations for the amplitude and duration of this load.

8. Tsunami-born debris impact and damming loads have not been investigated herein. Such loads can be quite large when a shipping container, ship or vehicle is carried on shore by a bore and driven into a bridge at speed. The authors are currently working on this topic in a project funded by the Pacific Earthquake Engineering Research Center. However all of the unknowns about debris loading are unlikely to be resolved in this project and this topic will be deserving of the future studies.

9. This study focused on the quantification of the tsunami-induced effects during the initial tsunami overland flow and impact on bridges. However, a future investigation focusing on the drawdown phase (reverse flow) of the tsunami could also be of interest. While it is expected that in the drawdown phase the outflow velocity will be a fraction of the inflow velocity (e.g. in the range of 30%) and the hydrodynamic loading under clear-water conditions would be small, it is entirely possible that the water will not be clear but entrain a large amount of debris and the loading could be significant. Therefore debris damming and impact during the drawdown phase could affect the design of some bridge components, such as the onshore girders and connections.

10. Although the principal failure mode observed in bridges in past tsunamis has been the failure of structural elements (e.g. connections and bearings between the super- and substructure), another mode has been scour at piers and abutments leading to undermining of foundations and, in some cases, span collapse. Future studies should focus on quantifying the potential for tsunami-induced scour and its likely effect on structural performance.

11. Mitigation strategies which aim at reducing tsunami loads on a bridge should also be examined in the future. Prior experimental work by the authors investigated the use of air-vents in the deck slab as a mitigation strategy for bridges subjected to solitary waves and bores. This work revealed that although such measures can significantly reduce the total tsunami-induced uplift, it does not necessarily have an equally beneficial effect on all structural components. Moreover, the effect of air-venting is not a linear function of the number of vents (i.e. perforated area). This means that future studies should focus on the optimization of the location and number of air-vents, as well as the investigation of alternative mitigation strategies, such as the modification of the bridge cross-section.

12. Additional topics deserving future investigation include:

   a) Response of curved bridges to tsunami loads. For such bridges it is expected that curvature will affect both the applied loads and the distribution of these loads to

structural components, with potentially interesting transient 3D effects that have not been quantified to date.

b) Response of straight bridges with significant slope between one abutment and the other. Such bridges could sustain different overturning moments (Mz), and both roll (Mx) and yaw (My) moments that do not exist when the two abutments are at the same elevation.

c) Response of an onshore bridge where there are two parallel bridges carrying traffic in opposite directions on a coastal highway. It is expected the onshore bridge will be protected by the offshore bridge during inundation with reduced impulsive loads. But this situation will be reversed during drawdown (reversed flow) and the possibility of significant outward debris flow.

13. Tsunami performance of a bridge damaged by preceding ground shaking deserves future study. Particularly, it would be of interest to understand the interaction of the failure modes caused by earthquakes and tsunamis, the accumulation of progressive damage and the prediction of the overall structural vulnerability.

14. Future studies should extend the work presented herein on single bridges to the tsunami risk assessment of coastal highways in order to advance the resilience of entire transportation networks and coastal communities.

7.0 REFERENCES

Azadbakht, M., & Yim, S. C. (2014). Simulation and estimation of tsunami loads on bridge superstructures. *Journal of Waterway, Port, Coastal, and Ocean Engineering*, *141*(2), 04014031. https://doi.org/10.1061/(asce)ww.1943-5460.0000262

Bradner, C., Schumacher, T., Cox, D., & Higgins, C. (2010). Experimental setup for a Large-Scale bridge superstructure model subjected to waves. *Journal of Waterway, Port, Coastal, and Ocean Engineering*, *137*(1), 3–11. https://doi.org/10.1061/(asce)ww.1943-5460.0000059

Cuomo, G., Shimosako, K.-, & Takahashi, S. (2009b). Wave-in-deck loads on coastal bridges and the role of air. *Coastal Engineering*, *56*(8), 793–809. https://doi.org/10.1016/j.coastaleng.2009.01.005

Douglass, S., Chen, J., Olsen, J., Edge, B., & Brown, D. (2006). *Wave forces on bridge decks*. US Department of Transportation Federal Highway Administration. Retrieved from https://www.yumpu.com/en/document/view/7198095/wave-forces-on-bridge-decks

Grezio, A., Babeyko, A., Baptista, M. A., Behrens, J., Costa, A., Davies, G., … Thio, H. K. (2017). Probabilistic tsunami hazard analysis: Multiple sources and global applications. *Reviews of Geophysics*, *55*(4), 1158–1198. https://doi.org/10.1002/2017rg000579

Hoshikuma, J., Zhang, G., Nakao, H., & Sumimura, T. (2013). Tsunami-induced effects on girder bridges. In *International Symposium for Bridge Earthquake Engineering in Honor of Retirement of Professor Kazuhiko Kawashima*. Tokyo, Japan.

Issa, R., & Violeau, D. (2006). *SPH European research interest community SIG test-case 2 3D dambreaking* (Release 1.1). France: Laboratoire National d'Hydraulique et Environnement. Retrieved from https://app.spheric-sph.org/sites/spheric/files/SPHERIC_Test2_v1p1.pdf

Istrati, D. (2017). *Large-scale experiments of tsunami inundation of bridges including fluid-structure-interaction* (Doctoral dissertation, University of Nevada, 2017). Reno, NV: ProQuest.

Istrati, D. and Buckle, I.G., (2019). Role of trapped air on the tsunami-induced transient loads and response of coastal bridges, *Geosciences Journal, Special Issue: River, Urban and Coastal Risk*, MDPI, 9 (191), doi: 10.3390/geosciences9040191

Istrati, D., Buckle, I.G., Lomonaco, P., and Yim, S., (2018). Deciphering the tsunami wave impact and associated connection forces in open-girder coastal bridges, *Journal of Marine Science and Engineering,* MDPI, 6 (148). doi: 10.3390/jmse6040148

Istrati, D., & Buckle, I. (2020). *Tsunami loads on straight and skewed bridges – Part 1:Experimental investigation and design recommendations* (Rep. No. FHWA-OR-RD-21-12). Salem, OR: Oregon Department of Transportation.

Kawashima, K. (2012). Damage of bridges due to the 2011 Great East Japan earthquake. *Journal of Japan Association for Earthquake Engineering*, *12*(4), 319–338. https://doi.org/10.5610/jaee.12.4_319

Kleefsman, K. M. T., Fekken, G., Veldman, A. E. P., Iwanowski, B., & Buchner, B. (2005). A Volume-of-Fluid based simulation method for wave impact problems. *Journal of Computational Physics*, *206*(1), 363–393. https://doi.org/10.1016/j.jcp.2004.12.007

Livermore Software Technology Corporation, (2014). *ICFD Theory Manual for Incompressible Fluid Solver in LS-DYNA*, Livermore CA, Retrieved from https://ftp.lstc.com/ anonymous/outgoing/inaki/docs/pdf_icfd/ICFD_theory.pdf .

McPherson, R. L. (2008). *Hurricane induced wave and surge forces on bridge decks* (Master's thesis, Texas A&M University, 2008). College Station, TX: Texas A & M University.

Motley, M. R., Wong, H. K., Qin, X., Winter, A. O., & Eberhard, M. O. (2015). Tsunami-Induced forces on skewed bridges. *Journal of Waterway, Port, Coastal, and Ocean Engineering*, *142*(3), 04015025. https://doi.org/10.1061/(asce)ww.1943-5460.0000328

Osher, S., & Fedkiw, R. (2003). *Level set methods and dynamic implicit surfaces (applied mathematical sciences (153))* (Vol. 153). New York, NY: Springer.

Seiffert, B., Hayatdavoodi, M., & Ertekin, R. C. (2014). Experiments and computations of solitary-wave forces on a coastal-bridge deck. Part I: Flat Plate. *Coastal Engineering*, *88*, 194–209. https://doi.org/10.1016/j.coastaleng.2014.01.005

Xiang, T., Istrati, D., Yim, S. C., Buckle, I. G., & Lomonaco, P. (2020). Tsunami loads on a representative coastal bridge deck: Experimental study and validation of design equations. *Journal of Waterway, Port, Coastal, and Ocean Engineering*, *146*(5), 04020022. https://doi.org/10.1061/(asce)ww.1943-5460.0000560

Yang, W., Wang, R., Arduino, P., Miller, G., & Mackenzie-Helnwein, P. (2014). Damage of bridges due to the 2011 Great East Japan earthquake. In *US-Japan Cooperative Program in Natural Resources, Panel for Wind and Seismic Effects, Tsunami Modeling Workshop*. Corvallis, OR: Oregon State University.

Zhu, M., Elkhetali, I., & Scott, M. H. (2018). Validation of OpenSees for tsunami loading on bridge superstructures. *Journal of Bridge Engineering*, *23*(4), 04018015. https://doi.org/10.1061/(asce)be.1943-5592.0001221